

ROTATIONAL BANDS AND PARTICLE-HOLE EXCITATIONS AT VERY HIGH SPIN

TORD BENGSSON and INGEMAR RAGNARSSON

Dept. of Mathematical Physics, Lund Institute of Technology, Box 118, S-22100 Lund, Sweden

Received 9 April 1984

(Revised 24 August 1984)

Abstract: A method of calculating high-spin states of nuclei within the cranked Nilsson-Strutinsky framework is presented and discussed in some detail. With this method, various high-spin features of nuclei are studied, such as shape coexistence, shape changes, band crossings and band terminations. Nuclei with different mass numbers such as ^{106}Pd , ^{118}Te , ^{158}Yb and ^{187}Au are used to exemplify the formalism. Comparisons are made with observed discrete high-spin states in $^{160}, ^{165}, ^{168}\text{Yb}$, ^{168}Hf , ^{171}Ta and ^{130}Ce .

1. Introduction

Theoretical studies on nuclei at very high spin were initiated by the liquid-drop-model calculations by Cohen, Plasil and Swiatecki ¹⁾ and by the more qualitative considerations by Bohr and Mottelson ²⁾. These works were of course inspired by the building of new accelerators which made experimental studies of very-high-spin states possible. Soon afterwards the cranked Nilsson-Strutinsky method was developed ^{3,4)} and applied to a large number of nuclei all over the nuclear periodic table ⁵⁻⁹⁾. These calculations have given a very important insight as to what phenomena can be expected in rapidly-rotating nuclei. They are, however, not able to directly predict experimental quantities such as γ -ray transition energies. These limitations arise from difficulties in the standard cranking-model formalism where only so-called optimal states ⁵⁾ are considered. In the special case when the high spin is built from pure particle-hole excitations (rotation around a symmetry axis), a method to circumvent the difficulties was introduced at an early stage ^{5,10,11)}. A formalism applicable also to collective rotation was subsequently developed but it was first applied only to very light nuclei ^{12,13)}. In this paper, we present further developments of this model which make the application also to heavier nuclei straightforward. Some applications of these developments have been reported in refs. ¹⁴⁻¹⁷⁾, but the formalism has only been briefly described. In sect. 2 of this paper, we will therefore give a more complete description of our calculating technique.

In the present calculations, the pairing correlations are neglected. Therefore, any detailed comparison between theory and experiment is not meaningful for very low spins. It is still not well understood for which spins the pairing energies are more

or less unimportant. Therefore, we rather take the attitude that a comparison between our results and experiments in different spin and mass regions will illuminate this very important question. Indeed, it is our experience that also for the very lowest spins, it is only in special cases that the yrast deformations are essentially affected by pairing [cf. ref. ¹⁸].

Sects. 4–8 are devoted to applications of the method described in sect. 2. As an introduction to these sections we discuss some quantities that can be extracted from continuum-type experiments in sect. 3. Then, in sect. 4, we consider the nucleus ¹⁸⁷Au in some detail and use it as an example to illustrate the present formalism. The concept of terminating bands is an interesting nuclear phenomenon that can be studied within our formalism. As ¹⁸⁷Au is not a very good example of a nucleus with such bands, sect. 5 is devoted to a general discussion of terminating bands. A few experiments in the continuum region are discussed in connection with calculational results in sects. 6 and 7. The nuclei considered are ¹⁰⁶Pd, ¹¹⁸Te, ¹²²Xe, ¹²⁸Ba and, in addition, some neutron-deficient rare-earth nuclei in the $A = 160$ – 170 region. From this study we can get an idea of how well we describe the general properties of nuclei at high spin such as, for example, the moment of inertia.

Discrete high-spin spectra are now available up to above spin 40 in some nuclei, which makes it interesting to compare them to high-spin states calculated in the present formalism. This is done in sect. 8. From these studies, and those of the preceding sections, some general features of the rotating non-paired system emerges, which are discussed in sect. 9. Finally the main conclusions of the present study are listed in sect. 10.

2. Calculational technique

In the solution to the usual cranking hamiltonian,

$$\hbar\omega = \hbar - \omega j_x, \quad (1)$$

where ω is the cranking frequency and \hbar the static hamiltonian, the problem of so-called virtual crossings arises. Virtual crossings occur when two single-particle orbitals with the same quantum numbers approach each other in energy, due to a change in a parameter of the hamiltonian, such as ω . As the orbitals have the same quantum numbers, they cannot cross but instead they exchange wave functions in a small region of ω . This is a disadvantage in the physical picture which emerges from the cranking model [cf. ref. ¹⁹]. In a real nucleus, two configurations should interact at constant value of the total spin I , not necessarily corresponding to the same cranking frequency.

In the cranking model, the total spin $I_{s.p.}$ and the total single-article energy $E_{s.p.}$ are calculated from the single-particle energies in the rotating system, e_i^ω , and the

expectation values of the j_x operator,

$$\begin{aligned} I &= I_{\text{s.p.}} = \sum_{\text{occ}} \langle j_x \rangle_i, \\ E_{\text{s.p.}} &= \sum_{\text{occ}} \langle h \rangle_i = \sum_{\text{occ}} e_i^\omega + \omega I_{\text{s.p.}}, \end{aligned} \quad (2)$$

where the sums are taken over the occupied orbitals. When these quantities are calculated at a frequency close to a virtual crossing at the Fermi surface, serious problems arise. As an example, we show in fig. 1 single-particle energies as a function of ω and the resulting $E_{\text{s.p.}}$ versus $I_{\text{s.p.}}$. The virtual crossing gives rise to a sudden increase in $I_{\text{s.p.}}$ at approximately constant ω for the lowest band. Thus, instead of the quadratic behaviour expected from a normal rotor, it results in a nearly linear behaviour of $E_{\text{s.p.}}(I_{\text{s.p.}})$. In the first excited band, there is a sudden decrease in $I_{\text{s.p.}}$ at the interaction frequency. If the decrease is large enough, this can result in a

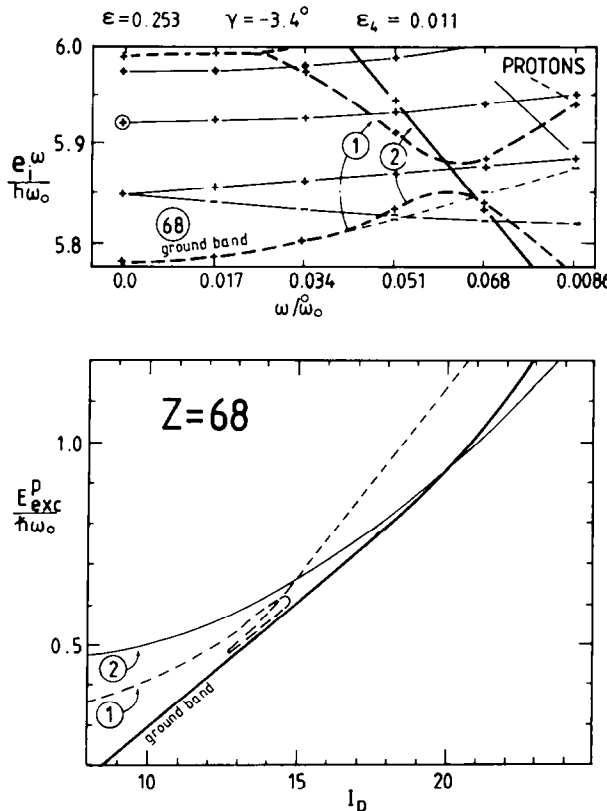


Fig. 1. Illustration of the difference between virtual and real crossings. *Top:* behaviour of single-particle energies e_i^ω as functions of the cranking frequency ω . Note the lowest configuration for 68 particles and the two orbitals which cross the last occupied orbital at $\omega/\omega_0 \approx 0.06$. *Bottom:* resulting $E_{\text{s.p.}}$ versus $I_{\text{s.p.}}$ from single-particle orbitals in the upper part. The lowest configuration (ground band) interacts with the first excited band (1), but not with the second (2).

loop-like character of $E_{s.p.}(I_{s.p.})$ for the excited band. As a counter-example we take a second excited band, having different parity. The two active orbitals are now allowed to cross (fig. 1), which means that the excited band follows a regular quadratic behaviour and cross the lowest band at a certain spin. Instead of the linear behaviour around the crossing spin we had before, we now get a band crossing which shows up as a distinct irregularity in the yrast line.

In standard cranking calculations⁵⁻⁹), neither virtual nor real crossings between orbitals are given any special attention. Instead, only one state is considered for each frequency. This so-called optimal state is the one where the lowest orbitals (all orbitals below the Fermi surface) are occupied. Consequently, a virtual crossing at the Fermi surface is treated as in fig. 1 while a real crossing gives rise to a discontinuous increase of the spin and the energy [cf. figs. 10, 11 of ref.⁵]. The intermediate spin values are then simply obtained from interpolation leading to more or less the same final result as for a virtual crossing (fig. 1). Such calculations can therefore only predict the gross nuclear behaviour. Especially, when the two axes perpendicular to the rotation axis are not very different (small collectivity), the large number of real and virtual crossings (see e.g. fig. 10 below) leads to a very schematic yrast line.

The problem of the real crossings is in principle straightforward to handle in the way shown in fig. 1. The virtual crossings on the other hand are more difficult. However, if a virtual crossing is replaced by a real crossing, it becomes possible to treat both crossings of fig. 1 in the same way [cf. fig. 1 of ref.¹²]. The problem is then reduced to that of deciding which virtual crossings should be removed and how this should be done. The method employed here will be discussed in subsect. 2.2.

The removal of virtual crossings contains necessarily a certain amount of arbitrariness, especially for heavier nuclei where the level density is high. Thus, in order to reduce the number of virtual crossings that has to be removed, we treat an "additional" quantum number as preserved, namely the total number of oscillator quanta in the rotating system, N_{rot} . To minimise the approximations involved, we work in a rotating basis, so that the effects of rotation are included already in the basis. As we furthermore include hexadecapole (ε_4) deformations, the diagonalisation procedure becomes rather involved and we devote subsect. 2.1 to a short description of it.

With the virtual crossings removed it is more meaningful to keep track of the quantum numbers of the yrast states. It is then natural to introduce "four different yrast lines" defined by the total parity and total signature¹²). However, further divisions could be made, for example by defining parity and signature independently for protons and neutrons. As one important benefit from introducing an additional preserved quantum number, we get the possibility to study a large number of well-defined excited configurations in the entire deformation plane. In subsect. 2.3 we discuss this facility of the model.

2.1. SINGLE-PARTICLE ORBITALS

In these calculations we are mainly interested in the very-high-spin states of nuclei, for which the deformation changes play an important role. The pairing correlations, on the other hand, should have decreased substantially. Furthermore, an almost unavailable amount of computation effort is needed to include large deformation changes *and* pairing in the same calculation. For these reasons, we do not include pairing in the calculations and leave to the comparison with experiment the question of whether it is permissible or not.

2.1.1. Hamiltonian. We work with the cranked Nilsson hamiltonian, which can be divided in the following way:

$$h^\omega = h_{\text{h.o.}}(\epsilon, \gamma) + 2\hbar\omega_0\rho^2\epsilon_4 V_4(\gamma) + V' - \omega j_x. \quad (3)$$

Here $h_{\text{h.o.}}(\epsilon, \gamma)$ is the deformed harmonic-oscillator hamiltonian:

$$h_{\text{h.o.}}(\epsilon, \gamma) = p^2/2m + \frac{1}{2}m\{\omega_x^2x^2 + \omega_y^2y^2 + \omega_z^2z^2\}. \quad (4)$$

The oscillator frequencies ω_x , ω_y and ω_z are expressed in the quadrupole deformation parameters (ϵ, γ) in the usual way²⁰.

The radius in the stretched coordinate system^{21,20} is denoted by ρ and the hexadecapole deformation potential $V_4(\gamma)$ is made dependent on γ in such a way that it does not break the axial symmetry when $\gamma = -120, -60, 0 or }60^\circ$. This is achieved by choosing the a_{4i} parameters in

$$V_4 = a_{40}Y_4^0 + a_{42}(Y_4^2 + Y_4^{-2}) + a_{44}(Y_4^4 + Y_4^{-4}) \quad (5)$$

so that they have the transformation properties of a hexadecapole tensor²²). Here we have employed the functions

$$\begin{aligned} a_{40} &= \frac{1}{6}(5\cos^2\gamma + 1), \\ a_{42} &= -\frac{1}{12}\sqrt{30}\sin 2\gamma, \\ a_{44} &= \frac{1}{12}\sqrt{70}\sin^2\gamma. \end{aligned} \quad (6)$$

Other forms are also possible, namely those which redefine the sign of ϵ_4 for different axes of symmetry, see ref.²³). Some early but less consistent calculations along these lines were carried out in ref.²⁴) where the a_{4i} coefficients were rather arbitrarily chosen to give reasonable shapes in the $0 \leq \gamma \leq 60^\circ$ sector.

The term V' of the Nilsson potential is of the form

$$V' = -\kappa(N)\hbar\omega_0\{2l_t \cdot s + \mu(N)(l_t^2 - \langle l_t^2 \rangle_N)\} \quad (7)$$

The index t in the orbital angular momentum operator l_t denotes that it is defined in stretched coordinates^{21,20}). The parameters κ and μ are made dependent on the main oscillator quantum number N as in table 1, thus facilitating the study of a wide range of nuclei with the same set of single-particle parameters. The parameters are chosen to essentially reproduce the fit of ref.²⁵) for the valence orbitals in

TABLE I
The modified oscillator parameters, κ and μ , which have been used in this work

N_{rot}	Protons		Neutrons	
	κ	μ	κ	μ
0	0.120	0.00	0.120	0.00
1	0.120	0.00	0.120	0.00
2	0.105	0.00	0.105	0.00
3	0.090	0.30	0.090	0.25
4	0.065	0.57	0.070	0.39
5	0.060	0.65	0.062	0.43
6	0.054	0.69	0.062	0.34
7	0.054	0.69	0.062	0.26
8	0.054	0.69	0.062	0.26

rare-earth and actinide nuclei. In the lighter regions, we have paid special attention to the Z or $N = 8, 20$ and 28 single-particle gaps. A further requirement is that the κ - and μ -values should vary with N in a smooth way. It has been tested that ground-state deformations and nuclear masses are obtained with a similar accuracy as for any other parameter set of the Nilsson potential [cf. ref.²⁶⁾]. For future reference, we show in figs. 2 and 3, the single-particle energies as a function of deformation with this set of parameters. The operators that commute with the hamiltonian h^ω are the parity operator π and the operator for performing a rotation of 180° around the cranking axis, $\exp(-i\pi j_x)$. The eigenvalues for the latter operator are $\exp(-i\pi\alpha)$, where the signature exponent quantum number α [ref.²⁷⁾] takes the values $\alpha = +\frac{1}{2}$ or $\alpha = -\frac{1}{2}$.

2.1.2. The rotating basis. It is possible to find a coordinate transformation so that the cranked harmonic oscillator separates into three uncoupled oscillators [see e.g. refs.^{28,29)}]:

$$\begin{aligned} h_{\text{h.o.}}^\omega &= h_{\text{h.o.}} - \omega_j = \sum_k \hbar \omega_k (c_k^+ c_k + \frac{1}{2}) - \omega_j \\ &\rightarrow \sum_i \hbar \Omega_i (a_i^+ a_i + \frac{1}{2}) - \hbar \omega \Sigma. \end{aligned} \quad (8)$$

Here Σ is the intrinsic spin projection on the cranking axis. The new oscillator frequencies Ω_i depend on deformation and cranking frequency:

$$\begin{aligned} \Omega_1 &= \Omega_x = \omega_x, \\ \Omega_i &= \Omega_i(\omega_y, \omega_z, \omega), \quad i = 2, 3. \end{aligned} \quad (9)$$

This gives the eigenvalues of the cranked harmonic oscillator,

$$E_{n_x n_2 n_3 \Sigma} = \hbar \omega_x (n_x + \frac{1}{2}) + \hbar \Omega_2 (n_2 + \frac{1}{2}) + \hbar \Omega_3 (n_3 + \frac{1}{2}) - \hbar \omega \Sigma, \quad (10)$$

and eigenfunctions $|n_x n_2 n_3 \Sigma\rangle$.

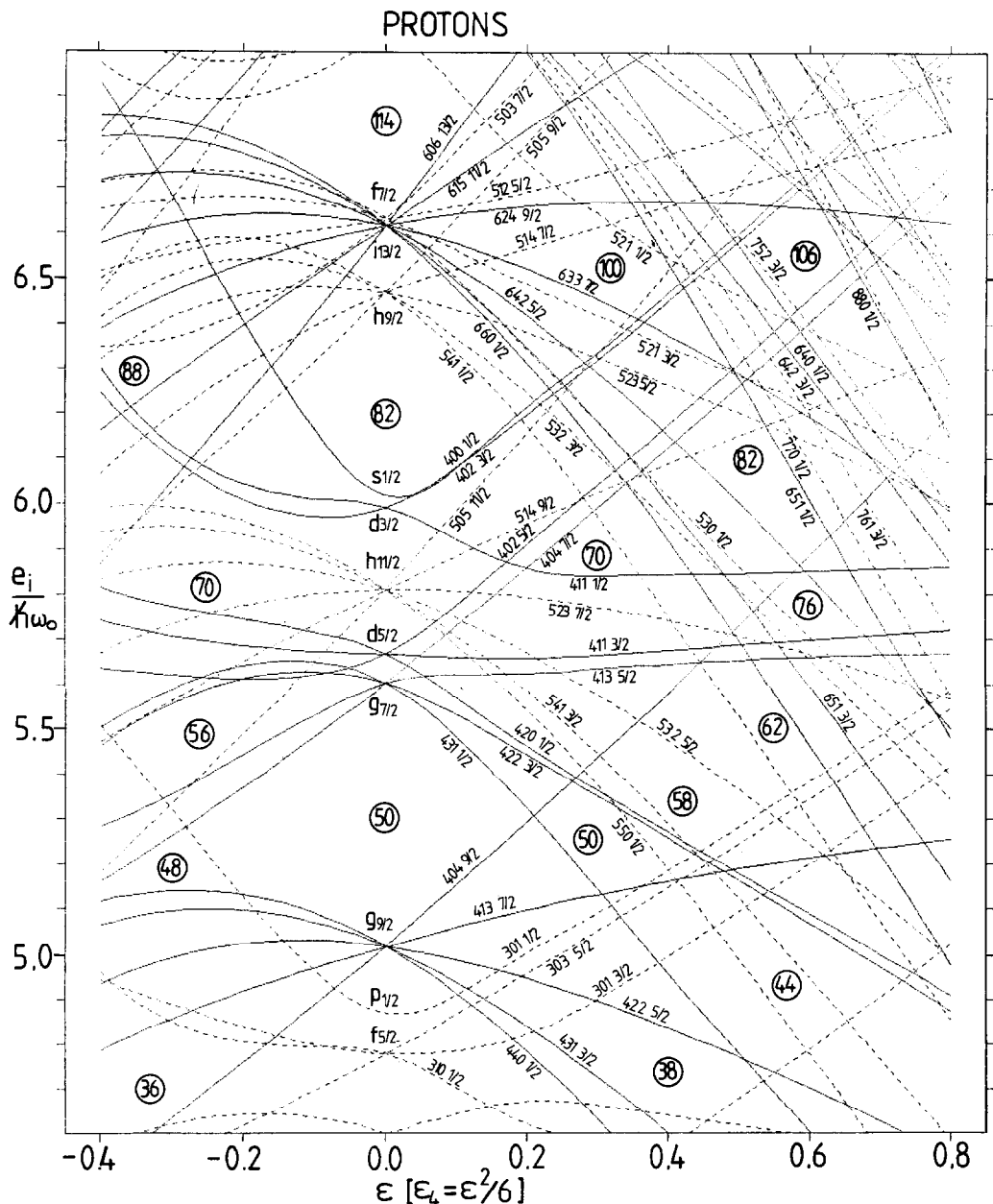


Fig. 2. Single-proton energies as functions of the quadrupole deformation parameter ϵ . The hexadecapole deformation is taken along an approximate liquid-drop valley, $\epsilon_4 = \frac{1}{6}\epsilon^2$. The single-particle parameters κ and μ are those given in table 1. Full and broken lines corresponds to positive-parity orbitals and negative-parity, respectively.

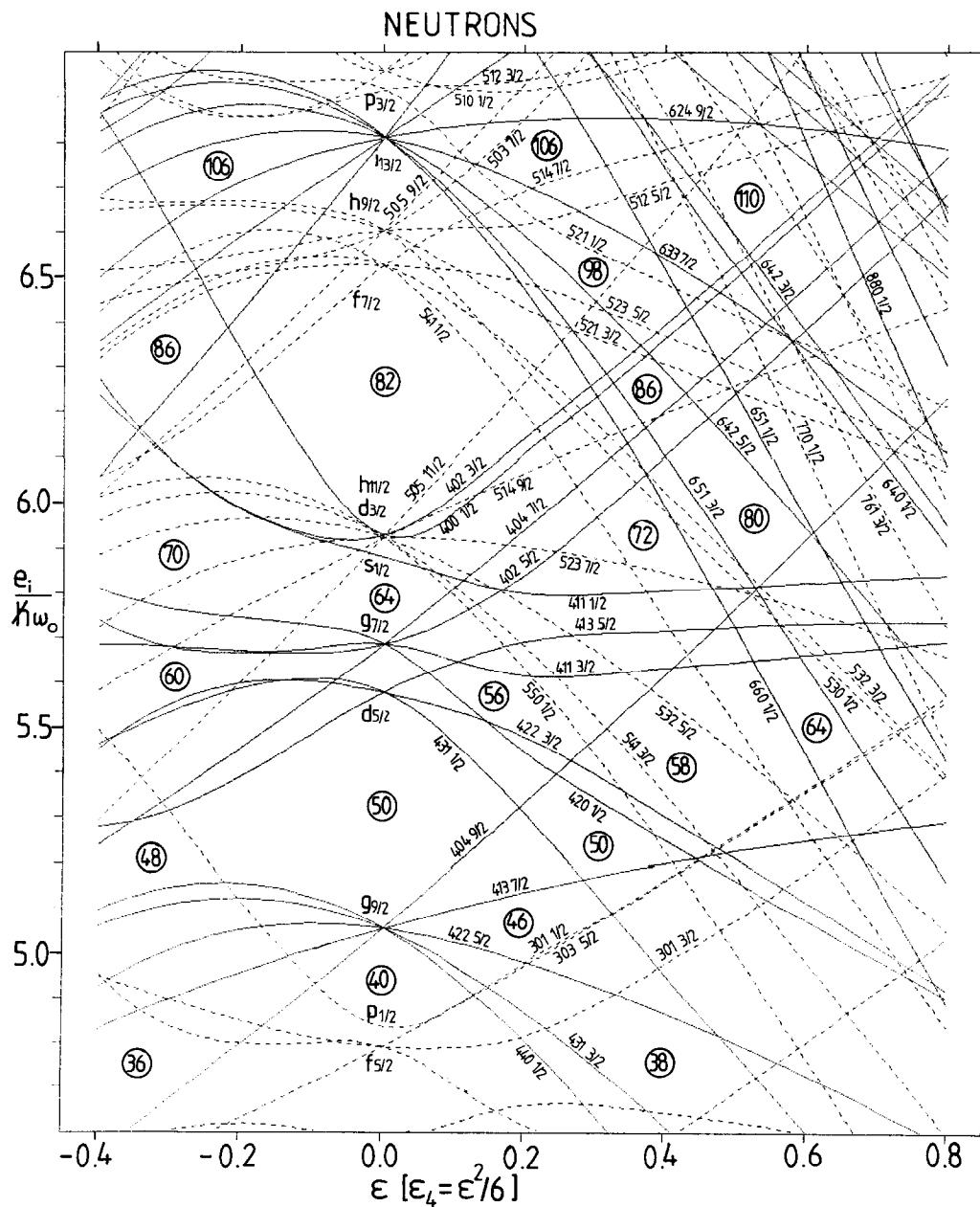


Fig. 3. Same as fig. 2, but for neutrons.

This rotating basis can be utilised for finding eigenfunctions of eq. (3). Since the couplings of j_x are fully accounted for in the rotating basis, the only terms in (3) which couple between basis states of different $N_{\text{rot}} = n_1 + n_2 + n_3$ are the hexadecapole deformation potential V_4 and the $l_i \cdot s$ and l_i^2 terms. The off-shell matrix elements of the latter terms are small for reasonable rotational frequencies. Neglecting the off-shell matrix elements of the V_4 term causes errors of minor importance at moderate deformations, as will be exemplified in subsect. 2.4. It thus seems reasonable to neglect all those matrix elements which are off-shell in the rotating basis, keeping N_{rot} as a preserved quantum number. As stated above, this will reduce the number of virtual crossings that have to be removed after the diagonalisation. Furthermore, excited configurations with a prescribed number of particles in different N_{rot} shells can be studied.

As the matrix elements of the V_4 potential proved to be hard to find in the rotating basis, we choose to perform the diagonalisation in two steps. First, we calculate a transformation matrix between the rotating $|n_1 n_2 n_3 \Sigma\rangle$ basis and the non-rotating $|Nlj\Omega\rangle$ basis. Then the matrix elements of (3) are calculated from their values in the non-rotating basis:

$$\begin{aligned} \langle \bar{n} | V_4 | \bar{n}' \rangle &= \sum_{\bar{N}, \bar{N}'} \langle \bar{n} | \bar{N} \rangle \langle \bar{N} | V_4 | \bar{N}' \rangle \langle \bar{N}' | \bar{n}' \rangle \\ |\bar{n}\rangle &\equiv |n_1 n_2 n_3 \Sigma\rangle \\ |\bar{N}\rangle &\equiv |Nlj\Omega\rangle. \end{aligned} \quad (11)$$

Here we only include matrix elements between basis states with the same N_{rot} . Furthermore, the sum is only taken over nonrotating states which have $N = N' = N_{\text{rot}}$. The resulting matrix is then diagonalized to give the single-particle orbitals in the rotating system. As the transformation matrix $\langle \bar{n} | \bar{N} \rangle$ only depends on quadrupole deformation and cranking frequency, the same matrix can be used for any value of ϵ_4 .

2.1.3. Generation of the transformation matrix. The transformation matrix can naturally be calculated using a diagonalisation procedure, where it is given by the resulting eigenvectors. We have chosen another approach, though, mainly to simplify the assignment of quantum numbers to the eigenvectors, which is especially difficult if some eigenvalues are degenerate. To avoid this difficulty, we generate the eigenvectors using step operators.

The use of step operators in a harmonic oscillator is well known from elementary quantum mechanics. For a one-dimensional harmonic oscillator, the x -operator can be expressed in the step-up and step-down operators:

$$x = \sqrt{\hbar/2m\omega_x} (a^+ + a), \quad a^+ = \sqrt{2m\omega_x/\hbar} x - a. \quad (12)$$

This gives a recursion relation for the eigenvector $|n\rangle$:

$$\sqrt{n+1} |n+1\rangle = \sqrt{2m\omega_x/\hbar} x |n\rangle - \sqrt{n} |n-1\rangle. \quad (13)$$

From this relation it is thus possible to calculate the eigenvector $|n+1\rangle$, once the eigenvectors $|n\rangle$ and $|n-1\rangle$ are known. The step operator in eq. (12) is applicable in the direction of the cranking axis (the x -axis) of the cranked harmonic oscillator. For the other directions more complicated expressions appear. The cranking term couples the oscillators in the y - and z -directions, which are transformed as indicated in eq. (8) into oscillators in the 2- and 3-directions. Expressions for these step operators can be found in ref.^{29]}.

The use of a stepping procedure to generate the transformation matrix is thus possible if the lowest eigenfunctions are known. An iterative method is used to calculate the lowest eigenfunction of each signature, $|n_x n_2 n_3 \Sigma\rangle = |000\Sigma\rangle$. First, split the cranked harmonic oscillator hamiltonian expressed in stretched coordinates into a spherical and a residual part:

$$\begin{aligned} h_{\text{h.o.}}^{\omega} &= \frac{1}{2}\hbar\omega_0(-\Delta_{\rho} + \rho^2) + V_{\text{def}}(\varepsilon, \gamma) - \omega j_x \\ &= h_{\text{sphere}} + V_{\text{res}}. \end{aligned} \quad (14)$$

Here both $h_{\text{h.o.}}^{\omega}$ and h_{sphere} have known eigenvalues:

$$\begin{aligned} h_{\text{sphere}}|Nlj\Omega\rangle &= \hbar\omega_0(N + \frac{3}{2})|Nlj\Omega\rangle = E_N|Nlj\Omega\rangle, \\ h_{\text{h.o.}}^{\omega}|000\Sigma\rangle &= \hbar\{\frac{1}{2}(\omega_x + \Omega_2 + \Omega_3) - \omega\Sigma\}|000\Sigma\rangle \\ &= E_{0\Sigma}|000\Sigma\rangle. \end{aligned} \quad (15)$$

Thus, by expressing $|000\Sigma\rangle$ in the basis $|Nlj\Omega\rangle$ one arrives at the following expression for the expansion coefficients:

$$\begin{aligned} \langle Nlj\Omega|000\Sigma\rangle &= \frac{1}{E_{0\Sigma} - E_N} \langle Nlj\Omega|V_{\text{res}}|000\Sigma\rangle \\ &= \frac{1}{E_{0\Sigma} - E_N} \sum_{N'l'j'\Omega'} \langle Nlj\Omega|V_{\text{res}}|N'l'j'\Omega'\rangle \langle N'l'j'\Omega'|000\Sigma\rangle. \end{aligned} \quad (16)$$

This expression can be used for an iterative procedure, in which one starts with

$$|000\Sigma\rangle = |N=0 l=0 j=\frac{1}{2}\Omega=\Sigma\rangle, \quad (17)$$

which is approximately valid for all reasonable rotational frequencies. The residual potential V_{res} has couplings with $\Delta N = 2$, so in order to give any amplitude in the $N = 8$ shell one needs at least four iterations. By iterating eq. (16), the expansion of $|000\Sigma\rangle$ can be obtained at any accuracy. We have found that six iterations give sufficient accuracy for the present applications, so that within the numerical uncertainty of the computer, the expansion of $|000\Sigma\rangle$ and then also of $|n_x n_2 n_3 \Sigma\rangle$ can be considered as exact.

2.2. REMOVAL OF VIRTUAL INTERACTIONS

2.2.1. Why remove interactions? When the single-particle orbitals have been calculated for a sequence of ω -values at a fixed deformation, there still occur virtual crossings as discussed above, even though their number has been considerably reduced by the diagonalisation procedure described in subsect. 2.1. The problem of virtual crossings can be exemplified with the aid of fig. 4. In fig. 4a, single-particle energies e_i^ω for one group of orbitals, with the same quantum numbers, are plotted as a function of ω . The actual diagonalisation has only been performed at the ω -values marked. The broken lines connect the energy values in such a way that different orbitals do not cross. The behaviour of the different orbitals ϕ_i then seems very complicated. From the relation

$$\frac{de_i^\omega}{d\omega} = -\langle \phi_i | j_x | \phi_i \rangle \quad (18)$$

this implies even more drastic changes in $\langle j_x \rangle$. Such drastic changes will introduce ambiguities in the final result, which can be thought of as interpolation errors but are of a more fundamental nature. The orbitals never cross, but their wave functions can be interchanged in a very narrow interval in ω , if the interaction is small enough. This means that a specific orbital (connected by the broken line in fig. 4a) does not necessarily have a wave function which varies in a smooth way as a function of rotational frequency. It may thus be questionable whether it is not more correct to connect those points of fig. 4a that have similar wave functions. An additional factor supporting such a conclusion is that in the cranking model the interaction between the orbitals occurs at constant rotational frequency while in a more correct theory, it should occur at constant spin. As is discussed in ref.¹⁹⁾, the interaction might cause a large spread in the angular momentum leading to unphysical results. Furthermore, if the strength of the interaction, V , satisfies

$$V < i^2/4J_c, \quad (19)$$

where i is the single-particle alignment caused by the band crossing and J_c the kinematical moment of inertia of the nucleus, one can show³⁰⁾, within a simple two-level model, that the interaction results in a backbend. Indeed, if the virtual crossing is left unchanged the result is that, for a certain region of ω , $I_{s.p.}$ and $E_{s.p.}$ of the excited band will decrease as functions of ω , as shown in fig. 1. This makes it impossible to calculate excited bands with any accuracy. In summary, a lot of problems with the cranking model are avoided if we replace at least those crossings that satisfy eq. (19) with real crossings.

2.2.2. How to remove interactions. To better understand the interactions, let us study the wave functions of the orbitals shown in fig. 4a. Wave functions are not easily visualised, but in fig. 4b we try to show the overlap

$$|\langle \phi_i(\omega_n) | \phi_j(\omega_{n+1}) \rangle|^2 \quad (20)$$

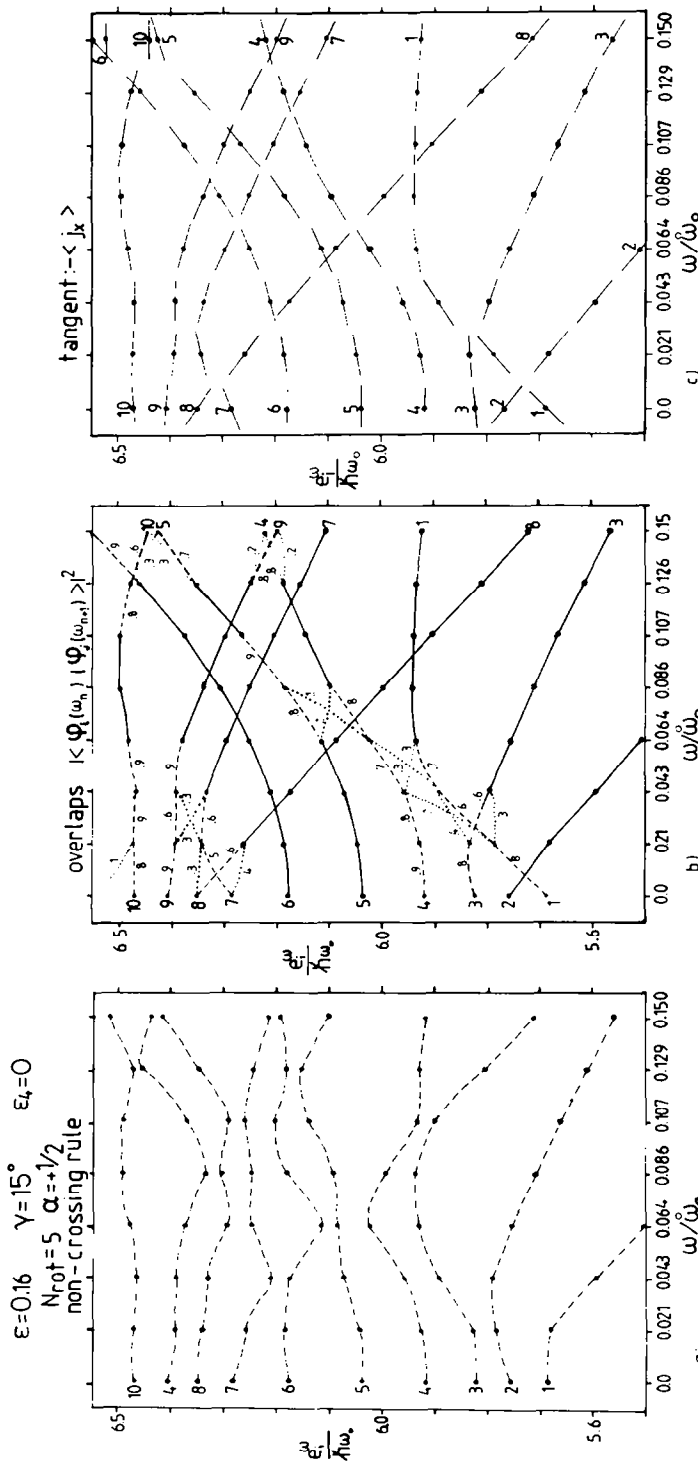


Fig. 4. Single-particle energies ϵ_i^ω as functions of rotational frequency ω , at the deformation $\epsilon = 0.16$, $\gamma = 15^\circ$ and $\epsilon_4 = 0$. All the orbitals have the same quantum numbers, $N_{\text{rot}} = 5$ and $\alpha = +\frac{1}{2}$. The diagonalisation has only been performed for the eight ω -values marked on the abscissa. In the figure to the left (a), the curves connect energies according to the non-crossing rule. Overlaps $|\langle \phi_i(\omega_n) | \phi_i(\omega_{n+1}) \rangle|^2$ between wave functions corresponding to the single-particle energies are shown in the middle (b). Points of maximal overlap are connected by broken lines or, if the overlap is larger than 0.9, by full lines. Dotted lines connecting two points indicate that the corresponding wave functions have a greater mutual overlap than 0.1. For the points connected by broken or dotted lines, the overlap is explicitly given. The numbers at the beginning and end of each line indicate how the orbitals should be drawn if points of maximal overlap were connected. To the right (c) the slope $-\langle j_x \rangle$, is shown at each calculated energy value as a tangent. The tangents give essentially the same suggestion about how the orbitals should continue as the wave functions.

between the wave functions in a simplified way. If the overlap (20) is greater than 0.9, we connect the points representing the single-particle energies with a full line. For lesser overlap, the line is broken and connects the points with the largest overlap. Dotted lines connect two single-particle energies, if their wave functions show greater overlap, as defined by (20), than 0.1. There is a drastic change between figs. 4a and 4b. In the latter figure, one clearly sees "strongly aligned orbitals" cross over a number of "less aligned orbitals", in many cases with virtually no interaction at all (no overlap). In some cases, there is a strong interaction between near-lying orbitals and it might be questionable whether they should be made to cross or not.

For those cases, where there is a virtual crossing and the wave functions are strongly interacting, ref.³¹⁾ recommends a rediagonalisation in the restricted space spanned by the interacting orbitals, without the coupling matrix elements. With this method, orbitals that are smooth functions of the cranking frequency ω can be constructed and thus the problems mentioned in subsect. 2.2.1 are avoided.

The handling of virtual crossings can be substantially simplified so that it is practically applicable for problems where one cannot afford to keep the whole set of single-particle wave functions. The only properties of the wave function we need in the applications described in this paper is the energy e_i^ω and the angular momentum projection on the cranking axis $\langle j_x \rangle_i^\omega \equiv \langle j_x \rangle_i$. From these quantities one can connect orbitals in much the same way as described above by observing that, in the cranking model, eq. (18) is exactly valid. Thus we can estimate $e_i^{\omega+\Delta\omega}$ and $\langle j_x \rangle_i^{\omega+\Delta\omega}$ at the cranking frequency $\omega + \Delta\omega = \omega_{n+1}$ from those given at $\omega = \omega_n$, by the assumption that $\langle j_x \rangle_i^\omega$ is approximately unchanged. The estimated value, $e_i^{\omega+\Delta\omega}(\rightarrow)$, can be determined from eq. (18) as

$$e_i^{\omega+\Delta\omega}(\rightarrow) = e_i^\omega - \Delta\omega \langle j_x \rangle_i^\omega. \quad (21)$$

These assumptions are visualised in fig. 4c. At each calculated energy value we have drawn a tangent whose slope corresponds to $-\langle j_x \rangle_i^\omega$ and thus should point at the energy value at the adjacent ω -value which corresponds to a similar wave function. If one then considers a specific orbital at ω_n as connected with the orbital at ω_{n+1} , where the tangents show the minimal deviation from the calculated energies, the result becomes quite similar to that of fig. 4b.

For questionable cases, we need a criterion for whether the orbitals at ω_n and ω_{n+1} should be connected or not. Thus we also estimate the energy at ω_n , $e_k^\omega(\leftarrow)$, from the values $\langle j_x \rangle_k^{\omega+\Delta\omega}$ and $e_k^{\omega+\Delta\omega}$ for the proposed continuation, orbital k at $\omega + \Delta\omega$:

$$e_k^\omega(\leftarrow) = e_k^{\omega+\Delta\omega} + \Delta\omega \langle j_x \rangle_k^{\omega+\Delta\omega}. \quad (22)$$

For the orbital k that has the smallest differences, $|e_i^{\omega+\Delta\omega}(\rightarrow) - e_k^{\omega+\Delta\omega}|$ and $|e_k^\omega(\leftarrow) - e_i^\omega|$, to orbital i , we check that it forms a reasonable continuation of orbital i . Thus, if the differences do not exceed the value $\Delta j \Delta\omega$, the orbitals i and k are connected to form a "new" orbital which will then cross one or several other orbitals. If no continuation with the difference smaller than $\Delta j \Delta\omega$ is found, the orbitals are left

unchanged at this stage but a search over the interval $2\Delta\omega$ as described below is carried through. If taken within reasonable limits, the value of Δj have no or, in specific cases, small influence on the final results. The value used, 0.6, has been determined by studying single-particle diagrams such as those of figs. 9, 10, 17, 21 and 22 below.

One special problem occurs if the diagonalisation is carried out at an ω -value where two (or more) orbitals have maximal interaction. We have thus included the possibility of searching for a continuation at ω_{n+2} , if none of the e_i^ω and $\langle j_x \rangle_i^\omega$ at ω_{n+1} lies within an uncertainty range, given by the uncertainty in $\langle j_x \rangle$, Δj . An equivalent procedure is then carried out for the ω_n and ω_{n+2} points as was described above for the ω_n and ω_{n+1} points.

This leaves an irregularity in the interacting orbitals at ω_{n+1} . To remove this interaction, we calculate the expected values of $\langle j_x \rangle_i^{\omega+4\Delta\omega}$ and $e_i^{\omega+4\Delta\omega}$ at the interaction frequency ω_{n+1} , via a third-degree polynomial interpolation, whose parameters are completely determined from the values of $\langle j_x \rangle_i^\omega$ and e_i^ω at the frequencies ω_n and ω_{n+2} . Then those expected values are adjusted so that the sums of e_i^ω and $\langle j_x \rangle_i^\omega$ over the interacting orbitals are left unchanged.

Our procedure aims at taking away the weak interactions between different orbitals and thus between different bands completely. This is of course not fully correct as there should always be some interaction left between all bands^{30,31)}. However, most of the crossings we create should indeed be quite sharp. For example, if the different bands could be characterised by different fillings of some high- j subshells, it is well known that essentially independent bands are formed at low spins and we can see no reason why this should not be the case also at higher spins. On the other hand, there are one or a few "crossings" at low frequencies in fig. 4 (within "h_{11/2} orbitals") which are more questionable. Such problems mainly occur at rather low rotational frequencies, however, and are thus less important in the present calculations which aim at describing the properties at higher spins. Even so, it is important to verify that the different properties we calculate are not strongly influenced by any questionable virtual crossings. This is one reason why the applications below are accompanied by a rather large number of single-particle diagrams.

Recently we have successfully applied this crossing procedure to Woods-Saxon single-particle orbitals [see ref.³²⁾], which means that the procedure has now reached such a stage of refinement that the diagonalisation procedure described in subsect. 2.1 is not absolutely necessary any longer, at least for medium-heavy nuclei. But, as we will see, other advantages of having an extra quantum number preserved might be as useful as the simplification of the crossing procedure.

2.3. CHOOSING OCCUPIED ORBITALS

In the nucleus, the states are characterised by their spin and parity. This means, that in addition to the total single-particle energy and spin, eq. (2), we must calculate

the total parity π_{tot} and signature α_{tot} of the nucleus:

$$\pi_{\text{tot}} = \prod_{\text{occ}} \pi_i, \quad (23)$$

$$\alpha_{\text{tot}} = \sum_{\text{occ}} \alpha_i \bmod 2.$$

The signature is needed, because for symmetry reasons the total signature α_{tot} of the nucleus determines the possible spin values^{27,33}). For an even nucleus $\alpha_{\text{tot}}=0$ gives $I=0, 2, 4, \dots$, whereas $\alpha_{\text{tot}}=+1$ gives $I=1, 3, 5, \dots$. In odd nuclei $\alpha_{\text{tot}}=-\frac{1}{2}$ gives $I=\frac{3}{2}, \frac{7}{2}, \frac{11}{2}, \dots$, whereas $\alpha_{\text{tot}}=\frac{1}{2}$ gives $I=\frac{1}{2}, \frac{5}{2}, \frac{9}{2}, \dots$

Keeping track of π_{tot} and α_{tot} means that we separate the total yrast line of the nucleus into four yrast lines, characterised by their parity and signature. We denote those bands with $(\pi_{\text{tot}}, \alpha_{\text{tot}})$, where in the following we will generally drop the index "tot" and simply write (π, α) . This separation enables us to study for example the continuation of an yrast band when it has been crossed by another band with different signature or parity. An even better separation can be made if we make use of all the preserved quantum numbers in the single-particle orbitals, N_{rot} , π and α . We can thus require that the occupied orbitals in eqs. (2) and (23) are such that they include a specific number of the most low-lying orbitals in the different symmetry groups having the same value of N_{rot} and α (π is given by N_{rot}). In the following, we will by "configuration" mean calculated nuclear states with a prescribed number of particles in the different symmetry groups of orbitals with fixed N_{rot} and α (cf. table 2 below). By a "band" we mean a sequence of nuclear high-spin states built on the same single-particle orbitals. An orbital is then defined from those points connected after the removal of virtual crossings. This means that a band can in general be recognized from the smooth behaviour of its energy as a function of spin I . With this convention, many bands are included in the same configuration and the calculations will only give the yrast part of these bands.

2.4. CALCULATION OF TOTAL ENERGIES

Having removed the virtual crossings between the single-particle orbitals, we are ready to calculate the total energy and spin for a variety of configurations in a nucleus at a given deformation. Since the single-particle orbitals are now smooth functions of ω , the total single-particle energy and spin for protons and neutrons within a band, eq. (2), can also be treated as smooth functions of ω . Among all the possible neutron and proton bands that correspond to a given configuration, those are studied that, at some value of ω , are optimal or can be reached via low-energy 1p1h or 2p2h excitations within the configuration. The energy, $E_{\text{s.p.}}(I)$, of the configuration is then given by the lowest band at the spin I .

Following the standard Nilsson-Strutinsky prescription^{34,3,5}), the total single-particle energy at this spin must be renormalised, so that the total nuclear energy is

given by

$$E_{\text{tot}}(I) = E_{\text{s.p.}}(I) - \langle E_{\text{s.p.}}(I) \rangle + E_{\text{r.l.d.}}(I), \quad (24)$$

where $\langle E_{\text{s.p.}}(I) \rangle$ is the Strutinsky-smoothed energy at the spin I , and $E_{\text{r.l.d.}}(I)$ is the rotating-liquid-drop energy

$$E_{\text{r.l.d.}}(I) = E_{\text{surf}} + E_{\text{Coul}} + \hbar^2 I^2 / 2J_{\text{rig}}. \quad (25)$$

The surface and Coulomb energies are calculated with parameters from ref.³⁵), while the rigid-body moment of inertia J_{rig} is calculated with a sharp nuclear surface and a radius parameter, $r_0 = 1.2$ fm. The calculations of $E_{\text{tot}}(I)$ are repeated for a large number of deformation points and the deformation of a nucleus in a specific configuration is determined by a minimisation of the total energy for each spin separately.

It is well known that the Nilsson potential has a somewhat strange rotational behaviour⁵⁻⁷), with the dynamical moment of inertia J_{dyn} , defined from the slope of the “Strutinsky-smoothed” quantities $\langle E_{\text{s.p.}} \rangle$ versus $\langle I \rangle^2$, approximately 30% larger than the rigid moment of inertia J_{rig} . This behaviour is caused by the I^2 term which brings down the high- I subshells relative to the low- I ones, making it energetically less expensive to create angular momentum in the Nilsson potential than in the pure oscillator. The Strutinsky renormalisation is introduced to renormalise to rigid rotation on the average but one could of course still ask if, for example, the high- I subshells of the $N+1$ principal shell might come too low in energy relative to the Fermi level in the N -shell. The $N+1$ orbitals would then become occupied at a too low rotational frequency. It seems to us that such questions can only be settled by comparing theory to the observed high-spin bands with such $N+1$ orbitals occupied even though it seems difficult to isolate this more basic question from the parameter fitting problem. This is illustrated by our discussion concerning the position of the proton $i_{13/2}$ (and $h_{9/2}$) subshells in subsects. 7.3, 8.1 and 8.2 below.

In this context, it seems important to test our approximation to neglect the off-shell hexadecapole matrix elements and also the cut-off in the (rotating) single-particle basis. For this purpose, we compared the shell-correction energy at $\omega = 0$, E_{sh} , given by

$$E_{\text{sh}} = \sum e_i - \langle \sum e_i \rangle, \quad (26)$$

of ^{166}Yb calculated within this approximation and with two more shells added including off-shell couplings, respectively. It was found that for reasonable small ε -values, say $\varepsilon \approx 0.5$, our approximation introduces only small changes in E_{sh} which are essentially negligible compared to other uncertainties. The insensitivity of the shell correction to the basis cut-off and to the couplings between shells was previously discussed in e.g. refs.^{36,37}). One should then note that with the rotating basis the errors should be more or less independent of rotational frequency. Therefore, with the possible exception of superdeformed states in heavy nuclei, the numerical convergence of the present calculations should be quite satisfying.

3. Quantities obtained in continuum-type experiments

Unresolved high-spin spectra have for a long time been the only way to study very-high-spin states in nuclei experimentally [see e.g. ref.³⁸⁾]. With improved detectors, discrete states are found at increasingly higher spins, but one also achieves a better statistical resolution in the unresolved spectra above the discrete lines. Quasi-continuum properties of nuclei will therefore in the foreseeable future continue to play an important role in the study of the very highest spins.

To facilitate the interpretation of continuum-type experiments, the results are usually interpreted in the form of a moment of inertia. Depending on what aspects of the nuclear high-spin states a particular experiment is sensitive to, one talks about different types of moment of inertia³⁹⁾. Formally, there are two general types, namely the kinematical moment of inertia $J^{(1)}$, defined as

$$J^{(1)} = I \left\{ \frac{dE}{dI} \right\}^{-1} = \frac{I}{\omega}, \quad (27)$$

and the dynamical $J^{(2)}$,

$$J^{(2)} = \left\{ \frac{d^2E}{dI^2} \right\}^{-1} = \frac{dI}{d\omega} = J^{(1)} + \omega \frac{dJ^{(1)}}{d\omega}. \quad (28)$$

A further division arises from the experimental situation. If the moment of inertia comes from transitions within a rotational band, one talks about $J_{\text{band}}^{(1)}$ and $J_{\text{band}}^{(2)}$. If the transitions are somehow averaged over a number of bands, one can define a $J_{\text{eff}}^{(2)}$ as in ref.⁴⁰⁾, where all E2 transitions in the deexciting cascade contribute, or a $J_{\text{yrast}}^{(2)}$ as in ref.³⁹⁾, where only yrast states are allowed to contribute. $J_{\text{eff}}^{(2)}$ is experimentally accessible for unresolved spectra, whereas $J_{\text{yrast}}^{(2)}$ require resolved spectra. Our calculational results concerning $J_{\text{eff}}^{(2)}$, described in ref.¹⁶⁾, are briefly reviewed in subsect. 6.2.

$E_{\gamma} - E_{\gamma}$ coincidence techniques as described in ref.^{41,42)}, are especially suited to the study of collective properties at very high spins. For a rotational nucleus a valley appears in a plot of the correlation function along the diagonal $E_{\gamma_1} = E_{\gamma_2}$. The width of the valley is related to the increase in transition energy between adjacent transitions within a rotational band, thus related to $J_{\text{band}}^{(2)}$. From fillings of the valley, one can in general deduce the occurrence of backbends, as then a number of transitions will have approximately the same energy. In sect. 7 we discuss the application of our calculational method to experiments of this kind.

4. The nucleus ^{187}Au

This nucleus is interesting because it shows shape coexistence^{43,44)} at low spin, a coexistence which according to a recent experiment⁴⁵⁾ seems also to survive to quite high spin values.

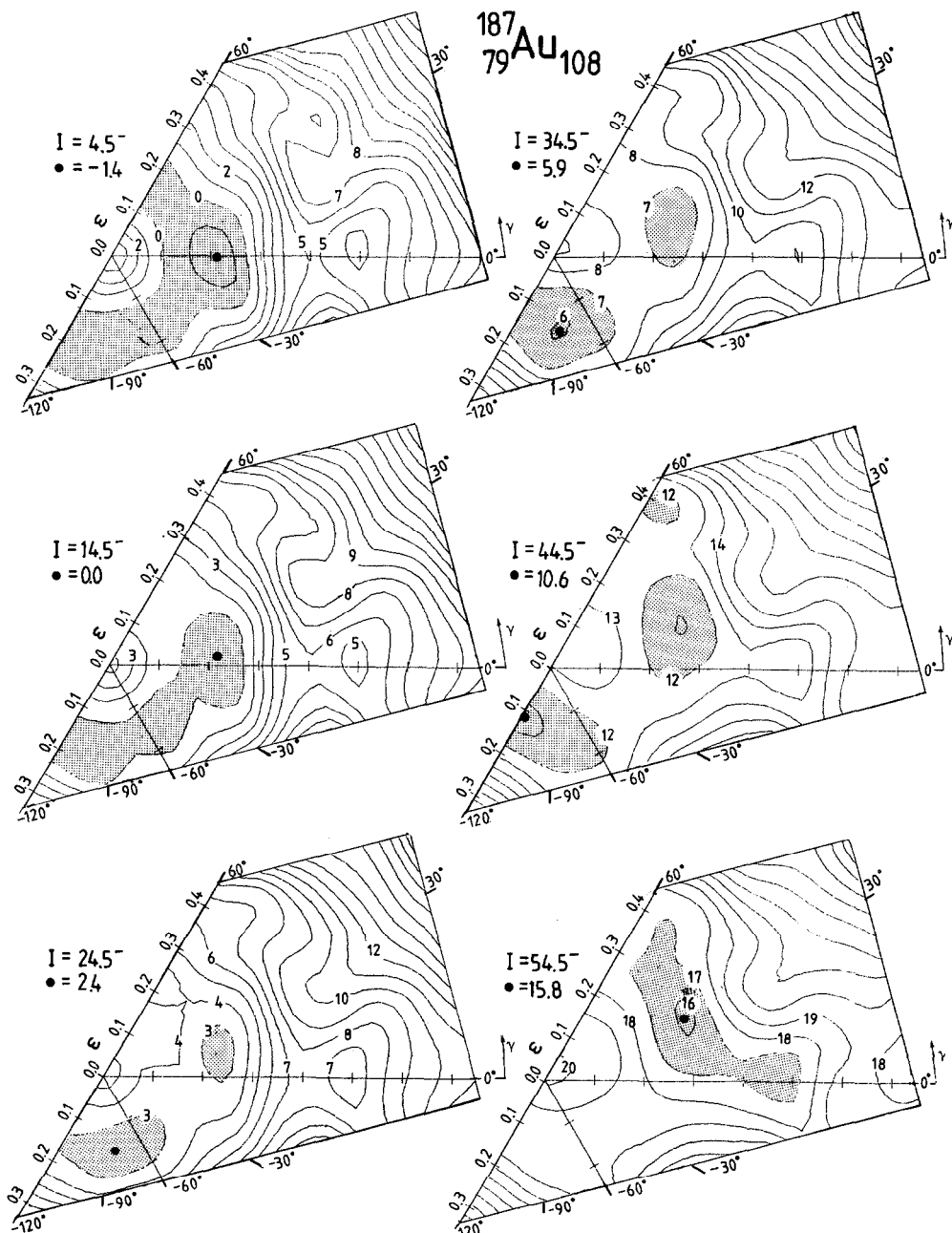


Fig. 5. Deformation energy surfaces at different spins for $\pi = -$, $\alpha = +\frac{1}{2}$ configurations in ^{187}Au . The contour line separation is 1 MeV. A dot indicates the lowest point on the surface. For $I \leq 50$, one especially notes the two coexistent minima that correspond to different coupling schemes.

At low spins, it seems as though the nuclear shape depends on the orbit of the odd particle^{43,44}). Thus, a small triaxial near-oblate deformation results with the odd proton in positive-parity ($d_{3/2}$, $s_{1/2}$) orbitals or $h_{11/2}$ orbitals while the deformation becomes larger and prolate if the odd particle is placed in the lowest $h_{9/2}$ orbital. This latter fact is easily understood from a single-particle diagram (fig. 2) where the [541½] orbital which emerges from $h_{9/2}$ is strongly down-sloping on the prolate side. Similarly, even though there is presently no experimental verification, one expects at somewhat higher excitation energies strongly-deformed prolate configurations with the odd particle in the lowest $N_{\text{rot}} = 6$ $i_{13/2}$ orbital, [660½].

Some selected potential energy surfaces of ^{187}Au are shown in fig. 5. They are calculated for parity $\pi = -$ and signature $\alpha = +\frac{1}{2}$. The two coupling schemes mentioned above manifest themselves in two different minima which survive separated up to quite high spins, $I \approx 40-50$. The minimum for prolate shape is found at $\epsilon \approx 0.20$ and $\gamma \geq 0$ for low spins and then evolves in the direction towards somewhat larger ϵ - as well as γ -values. For negative-parity and signature $\alpha = +\frac{1}{2}$, it is for low spins mainly the "h_{9/2} states" which are favoured. This is thus consistent with the prolate shape at the lowest minimum for $I'' = \frac{9}{2}^-$. The second minimum in this surface is found at a large negative γ -value which, according to particle-rotor calculations^{43,44}), more or less corresponds to the bandhead deformations for positive-parity or $h_{11/2}$ states. One should note that in standard particle-rotor calculations, no distinction is made between the three 60° sectors of the (ϵ , γ) plane. However, the present calculations suggest that those states of ^{187}Au which are generally referred to as triaxial or oblate are most naturally described as having $\gamma \leq -60^\circ$ (rotation around the smaller axis) in the cranking formalism. The negative γ -minimum becomes, in the present calculations, more pronounced at higher spins and is seen for $\gamma = -75^\circ - 120^\circ$ and $\epsilon = 0.10-0.20$ for all spins up to $I \approx 50$. These states are then either of ph character for prolate shape or triaxial, in some cases near-oblate, with a small collectivity.

The different minima of the energy surfaces can be used to construct different bands, E versus I . Some typical examples of such bands are shown in figs. 6a, b. There, in addition to the collective yrast states of $\pi = -$, $\alpha = +\frac{1}{2}$ (fig. 5), we also show the most low-lying bands which emerge from the fixed configuration calculations, where the fixed configurations are specified in table 2. The very different features of the bands having high collectivity (fig. 6a), and small collectivity (fig. 6b), respectively, are easy to recognize.

It is of course straightforward to construct potential energy surfaces also for the fixed configurations. This is illustrated in fig. 7 where, for $I'' = 32.5^+$, we give the energy surface for some different fixed configurations, together with the more standard surface which results if all $\pi = +$, $\alpha = +\frac{1}{2}$ configurations are considered simultaneously. It is interesting to see how the fixed configuration surfaces have only one very well-defined minimum with the energy increasing very smoothly in all directions away from the minimum. This suggests that, when the energy is interpolated for some deformation between the mesh points, this is done much more

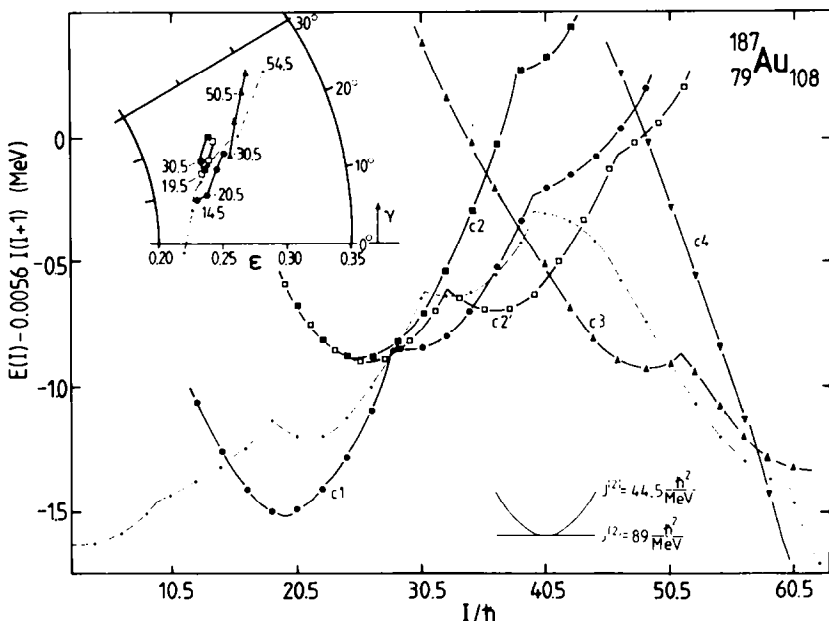


Fig. 6a. Total energy minus average liquid-drop contribution for some collective bands of ^{187}Au , as specified in table 2. The thin line indicates the lowest $(\pi, \alpha) = (-, +\frac{1}{2})$ states in the $\gamma \geq 0^\circ$ region. The curvature corresponding to two different values of the moment of inertia $J_{\text{band}}^{(2)}$ is also indicated. As an insert the change of deformation with spin is shown in steps of $10 \hbar$. In all cases, the asymmetry parameter γ increases slowly with spin.

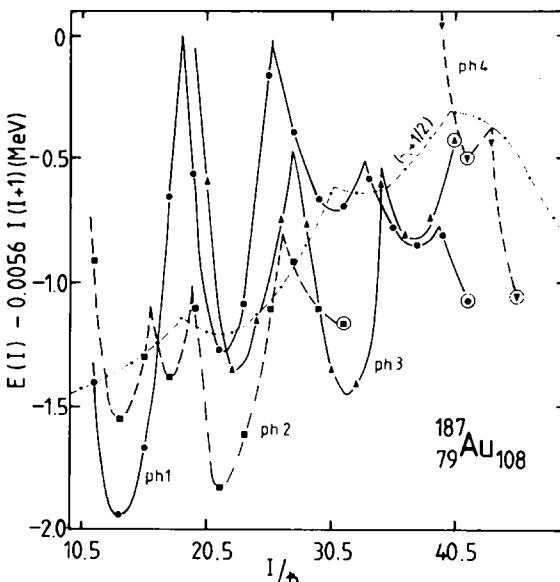


Fig. 6b. Same as fig. 6a, but here we show bands of small or no collectivity, i.e. those bands that correspond to the minima found around $\gamma = -100^\circ$ in fig. 5. Terminating states on the $\gamma = -120^\circ$ axis (prolate shape) are indicated by an open circle. As a comparison the $(-, +\frac{1}{2})$ collective states of fig. 6a are also given.

TABLE 2
Low-lying ^{187}Au configurations which are given special attention in our calculations

Proton conf.			N_{rot}	α	- $\frac{1}{2}$	+ $\frac{1}{2}$	- $\frac{1}{2}$	+ $\frac{1}{2}$	- $\frac{1}{2}$	+ $\frac{1}{2}$	- $\frac{1}{2}$	+ $\frac{1}{2}$	- $\frac{1}{2}$	+ $\frac{1}{2}$
				- $\frac{1}{2}$	+ $\frac{1}{2}$	- $\frac{1}{2}$	+ $\frac{1}{2}$	- $\frac{1}{2}$	+ $\frac{1}{2}$	- $\frac{1}{2}$	+ $\frac{1}{2}$	- $\frac{1}{2}$	+ $\frac{1}{2}$	
Neutron conf.			4	13	13	13	13	11	11	14	14	15	14	
			5	6	6	5	6	6	7	6	5	5	5	
			6	0	1	1	1	2	2	0	0	0	0	
α	N_{rot}	5	6	7	(π, α)		(+, + $\frac{1}{2}$)	(-, + $\frac{1}{2}$)	(-, + $\frac{1}{2}$)	(-, - $\frac{1}{2}$)	(+, - $\frac{1}{2}$)			
$-\frac{1}{2}$	14	5	0		(+, 0)			c1						
$+\frac{1}{2}$	14	5	0			(+, + $\frac{1}{2}$)								
$-\frac{1}{2}$	14	4	0		(-, 1)				c2'					
$+\frac{1}{2}$	15	5	0				(-, - $\frac{1}{2}$)							
$-\frac{1}{2}$	14	5	0		(-, 0)			c2						
$+\frac{1}{2}$	15	4	0				(+, + $\frac{1}{2}$)							
$-\frac{1}{2}$	14	4	1		(-, 0)			c3						
$+\frac{1}{2}$	14	5	0				(+, + $\frac{1}{2}$)							
$-\frac{1}{2}$	11	7	1		(-, 0)				c4					
$+\frac{1}{2}$	11	6	2					(+, + $\frac{1}{2}$)						
$-\frac{1}{2}$	15	4	0		(-, 0)					ph1	ph4			
$+\frac{1}{2}$	14	5	0							(+, - $\frac{1}{2}$)	(-, - $\frac{1}{2}$)			
$-\frac{1}{2}$	15	4	0		(+, 0)					ph2				
$+\frac{1}{2}$	15	4	0							(-, - $\frac{1}{2}$)				
$-\frac{1}{2}$	15	5	0		(-, 1)					ph3				
$+\frac{1}{2}$	14	4	0							(+, + $\frac{1}{2}$)				

The configurations are specified by the number of protons and neutrons in different groups of orbitals with fixed N_{rot} and α . The (π, α) quantum numbers are given separately for protons and neutrons. Underneath each configuration label c1, c2', ... we give (π, α) for the total configurations.

accurately if one configuration is fixed than if different configurations are considered simultaneously.

4.1. COLLECTIVE STATES

The band structure which is seen in the E versus I plot (fig. 6a) becomes even more apparent if the transition energies $\Delta E = E(I) - E(I-2)$ are plotted versus spin I . Thus, with only collective states ($\epsilon > 0.18$ and $0 < \gamma < 30^\circ$) considered, such plots are given in fig. 8. They are constructed for the negative-parity yrast states of $\alpha = +\frac{1}{2}$ and $\alpha = -\frac{1}{2}$, respectively. It is well known that the backbends or upbends observed in these curves are caused by band crossings along the yrast line. In fig. 8, we also show ΔE versus I for the fixed collective configurations (table 2) which were depicted in fig. 6a. In these cases a backbend corresponds to a band crossing within a fixed configuration.

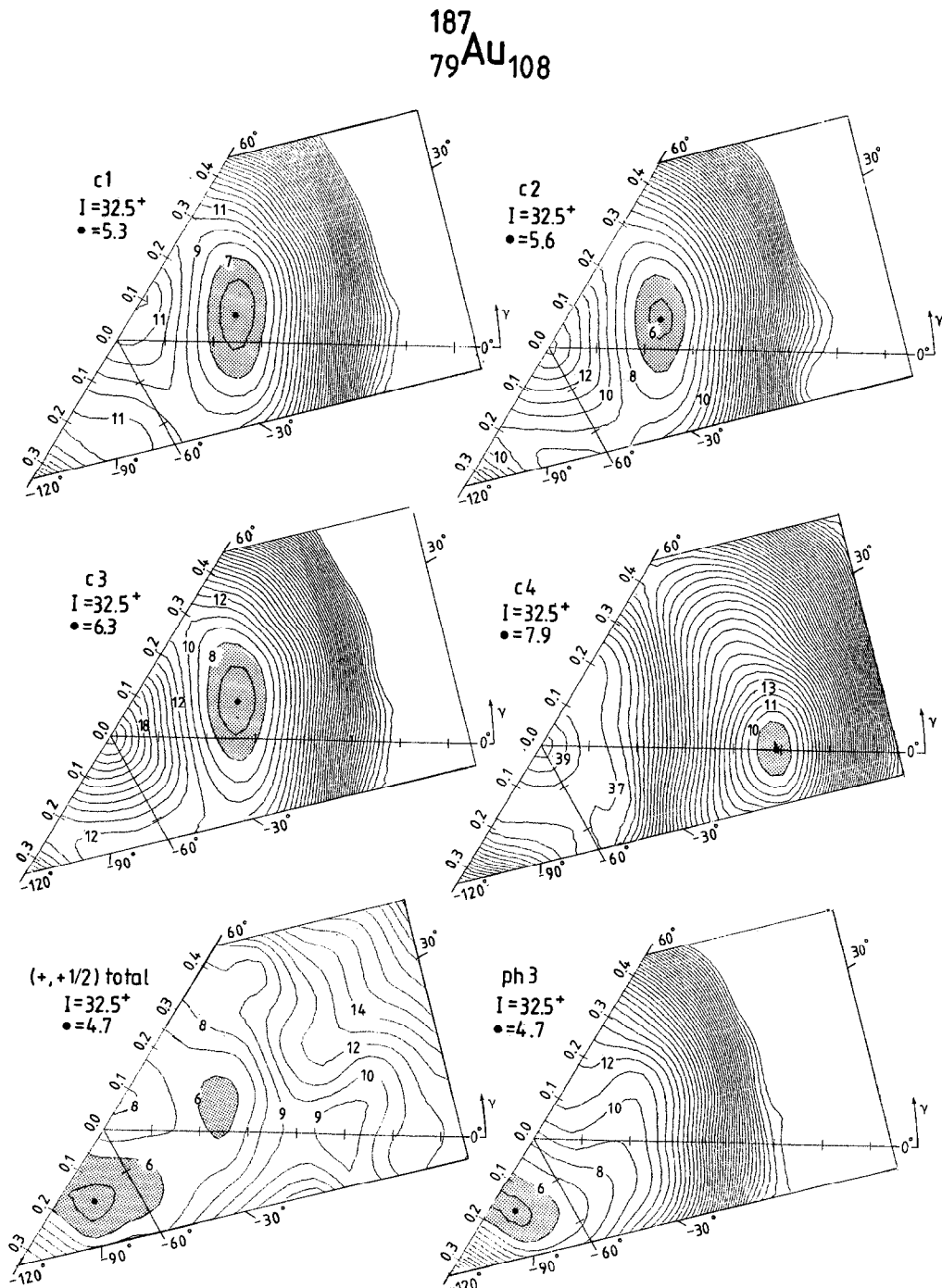


Fig. 7. Deformation energy surfaces as in fig. 5, but for some fixed configurations at spin 32.5^+ , i.e. $(\pi, \alpha) = (+, \frac{1}{2})$. The configurations are defined in table 2. Also the surface resulting from an energy minimisation within all $(+, \frac{1}{2})$ configurations is given.

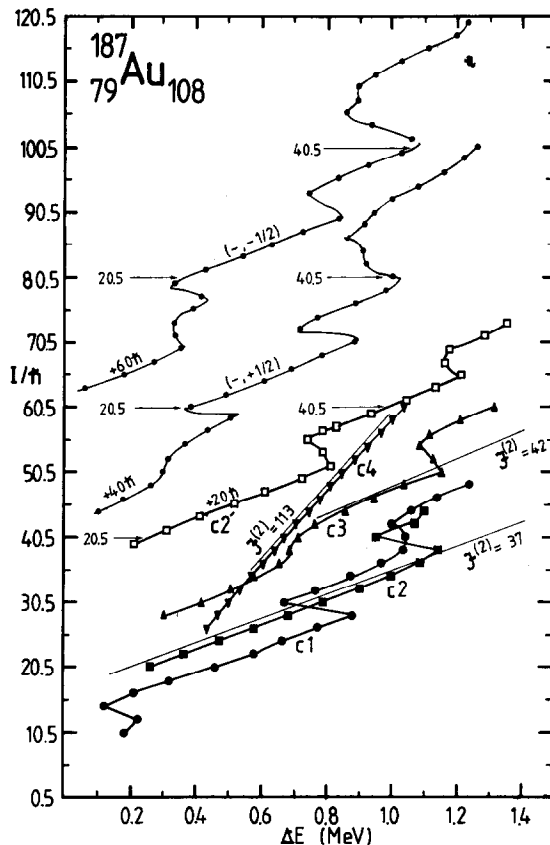


Fig. 8. Spin versus transition energy for the fixed configurations of fig. 6a and additionally for the $\pi = -$ yrast bands of ^{187}Au . The different (π, α) combinations are displaced vertically by $\Delta I = 20 \hbar$, so the scale on the ordinate is strictly valid only for the $(+, \frac{1}{2})$ configurations c1, c2, c3 and c4. The moment of inertia $J_{\text{band}}^{(2)}$ (in units of \hbar^2/MeV) for some different slopes of the lines is also indicated.

The identification of the different yrast bands, becomes straightforward with help of single-particle diagrams at appropriate deformations. Thus, in fig. 9, the energies of proton as well as neutron orbitals are given as functions of $\hbar\omega$. The deformation used, $\epsilon = 0.24$ and $\gamma = 15^\circ$, is appropriate for the collective yrast states at spins $I \sim 15-40$, see insert of fig. 6a. Some general features can be extracted from these diagrams. For the protons, a rather high spin ($I \sim 15$) is supplied from two protons in $h_{9/2}$ and one in $i_{13/2}$ already at low rotational frequencies. At somewhat higher ω -values, it is rather the configuration with two protons in $i_{13/2}$ and one in $h_{9/2}$ which becomes optimal. In a large frequency interval, these two are the only proton configurations which are of any importance. At small ω -values, the low-lying neutron configurations have 8, 9 or 10 particles in $i_{13/2}$. At $\hbar\omega > 0.35$ MeV, some strongly down-sloping orbitals cross the Fermi surface. The corresponding band crossings are seen as backbends at transition energies $\Delta E = 0.8-1.0$ MeV in fig. 8.

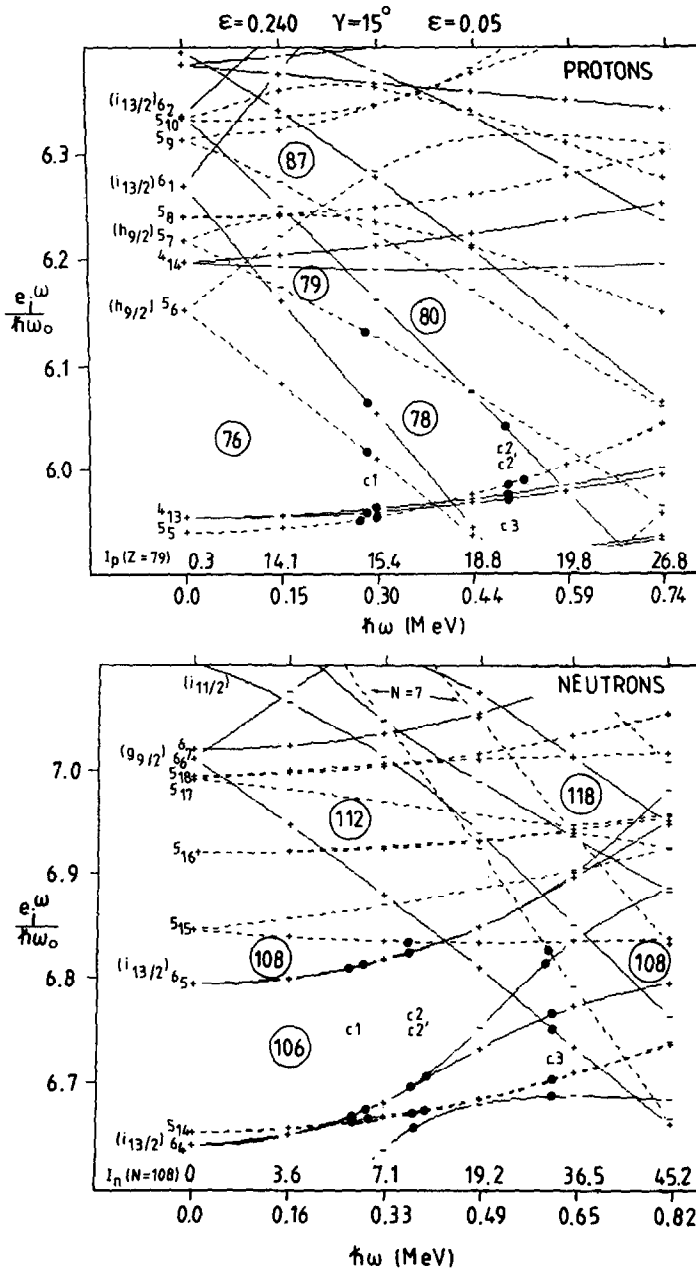


Fig. 9. Single-particle energies e_i^ω as a function of cranking frequency ω , for the deformation $\epsilon = 0.24$, $\gamma = 15^\circ$ and $\epsilon_4 = 0.05$. The scale on the abscissa is corrected by a Strutinsky renormalisation factor⁵⁾ so (provided the deformation is the proper one) there should be a one-to-one correspondence between a crossing frequency in the present diagram and the backbending frequency in a diagram such as that of fig. 8. The total proton ($Z = 79$) and neutron ($N = 108$) spin for the optimal configurations is also indicated on the abscissa. At $\omega = 0$ the orbitals are labelled with the main oscillator quantum number, N_{rot} , and as a subscript the position of the orbital within the N_{rot} shell. Signature $\alpha = +\frac{1}{2}$ is marked with "+", $\alpha = -\frac{1}{2}$ with "-". Some orbitals can approximately be assigned to specific j -shells as indicated. The orbitals which are occupied in the "collective" configurations $c1$, $c2$, $c2'$ and $c3$ are also indicated, cf. table 2.

We are now prepared to identify which orbitals are filled in the different bands illustrated in figs. 6a, 8. The $\pi = +$, $\alpha = +\frac{1}{2}$ band (conf. c1) which is strongly favoured for $I = 20$ has two protons in $h_{9/2}$ and one in $i_{13/2}$ while it has 10 neutrons in $i_{13/2}$. The band crossings observed at $I \approx 27$ and $I \approx 40$, respectively, arise when the first $g_{9/2}$ ($\alpha = +\frac{1}{2}$) and the first $i_{11/2}$ ($\alpha = -\frac{1}{2}$) neutron orbitals cross the Fermi surface. For small values of γ , these two $N_{\text{rot}} = 6$ orbitals could also be characterized by their asymptotic quantum numbers for $\hbar\omega = 0$, $[651\frac{1}{2}]$ and $[640\frac{1}{2}]$, respectively.

The configurations c2 and c2' with $\pi = +$ and $\alpha = +\frac{1}{2}$ and $-\frac{1}{2}$, respectively, have two protons in $i_{13/2}$ and one in $h_{9/2}$. Then, to get positive parity they have 9 neutrons in $i_{13/2}$, where for the ninth neutron $\alpha = -\frac{1}{2}$ in c2 and $\alpha = +\frac{1}{2}$ in c2', see table 2. The band crossing observed at $\hbar\omega \approx 0.4$ MeV in conf. c2' is caused by the filling of the first $g_{9/2}$ neutron orbital. As there are only four $N_{\text{rot}} = 6$, $\alpha = +\frac{1}{2}$ neutrons in conf. c2, the corresponding $g_{9/2}$ occupation comes first at $\hbar\omega \approx 0.5$ MeV in this case. The second backbend seen in the c2' configuration ($I \approx 45$, $\Delta E \approx 1.2$ MeV) results when a $h_{11/2}$ proton orbital is emptied and the second $h_{9/2}$ orbital is being occupied, see fig. 9.

In configuration c3, one neutron has been put into the lowest $N_{\text{rot}} = 7$ orbital. This should be favourable for $I \geq 40$ because the $N_{\text{rot}} = 7$ orbital crosses the Fermi surface at a somewhat smaller frequency than does the lowest $i_{11/2}$ orbital. There are then 9 neutrons in the $i_{13/2}$ subshell while the proton orbitals are filled as in configuration c2. The filling of the $N_{\text{rot}} = 7$ orbital leads to a somewhat increased deformation which affects the different band crossings. Below the backbend at $I \approx 40$ (which is rather calculated as an upbend due to interpolation errors), there are five nucleons in orbitals carrying "aligned spin", namely two protons in $i_{13/2}$, two protons in $h_{9/2}$ and one neutron in $j_{15/2}$. The backbend is then caused by the filling of the $g_{9/2}$ neutron orbital while the more distinct backbend at $I \approx 50$ at $\Delta E = 1.1$ MeV occurs when the first $i_{11/2}$ neutron orbital becomes occupied. The frequencies of the backbends are rather different for different mesh points. Especially, the crossing frequencies between the lowest $h_{9/2}$ and the highest $h_{11/2}$ proton orbitals depend strongly on deformation. This might lead to rather large interpolation errors when the equilibrium deformation is not close to any mesh point. It turns out that this is the case for configuration c3 at spins $I = 30-50$.

Let us now also identify which orbitals are filled in the different bands of the $\pi = -, \alpha = +\frac{1}{2}$ yrast states (figs. 6 and 8). At very low spins, the odd proton is in the lowest $h_{9/2}$ orbital. The second $h_{9/2}$ and the first $i_{13/2}$ proton orbitals become occupied at $I = 10$ and $I = 18$, respectively. The filling of the lowest $g_{9/2}$ neutron orbital is seen for $\Delta E \approx 0.8$ MeV and $I \approx 30$. This alignment is accompanied by the excitation of one proton from the second $h_{9/2}$ to the second $i_{13/2}$ proton orbital. Then, for $I \approx 40$ and $\Delta E \approx 0.95$ MeV, the first $N_{\text{rot}} = 7$ neutron orbital becomes occupied. At more or less the same rotational frequency, one proton is lifted from $h_{11/2}$ to $h_{9/2}$ and the neutron in the lowest $i_{11/2}$ orbital becomes occupied. The transition energies for $\pi = -$ and $\alpha = -\frac{1}{2}$ show very much the same pattern as those for $\pi = -$ and $\alpha = +\frac{1}{2}$. This is seen in fig. 8. No similar plot is given for the

positive-parity yrast states but they also show backbends at more or less the same frequencies and spin.

For spin $I \approx 60$, states built on a strongly deformed minimum at $\varepsilon \approx 0.47$ and $\gamma = 0^\circ$ become yrast. The corresponding band for the $\pi = +$ and $\alpha = +\frac{1}{2}$, configuration c4, is drawn in figure 6a. There is probably no hope of observing spins as high as $I = 60$ in a heavy nucleus like ^{187}Au . Note, however, that for $I = 40$, for example, the strongly-deformed configuration is predicted to be only ~ 1.5 MeV above yrast. The potential energy barrier between the two minima at $\varepsilon \approx 0.30$, $\gamma \approx 25^\circ$ and $\varepsilon \approx 0.47$, $\gamma = 0^\circ$ is not very high. Even so, the corresponding configurations are very different which suggests that any decay between the two nuclear shapes should be strongly hindered.

It is also interesting to study the general structure of E versus I as drawn in fig. 6a. One observes that the energy of the collective states increases rather smoothly up to $I = 40$. Around this spin, there is a sudden discontinuity and the energy begins to increase less rapidly with spin. The discussion above shows that this is connected with a more or less simultaneous alignment of 3 particles, two neutrons ($j_{15/2}$ and $i_{11/2}$) and one proton ($h_{9/2}$). One might have expected that these alignments should be accompanied by a drastic shape change but as seen in the insert of fig. 6a, this is not the case. When more and more particles "get aligned" one notices small increases in both γ and ε but all shape changes up to $I = 60$ are quite small. With three protons in aligned orbitals ($I \approx 15-20$) the calculations predict $\gamma \approx 10-15^\circ$ while for $I \approx 60$, when four protons and three neutrons are "aligned" we calculate $\gamma \approx 25$.

With the simultaneous increase of ε and γ for spins $I = 20-50$, one might expect that the collectivity stays more or less constant. One way to quantify such a statement is to calculate the moment of inertia $J_{\text{band}}^{(2)}$ which was defined in sect. 3. In a plot of I versus ΔE (fig. 8), $J_{\text{band}}^{(2)}$ which is defined for each band individually, is simply proportional to the slope of the curve for that band, $J_{\text{band}}^{(2)} = \Delta I / \Delta \omega$. If E is plotted versus I , $J_{\text{band}}^{(2)}$ is proportional to the curvature, see fig. 6a. For the fixed configurations, with exception of the superdeformed c4, it turns out that the slopes of fig. 8 are very much the same in all cases, $J_{\text{band}}^{(2)} \approx 40 \hbar^2 / \text{MeV}$. This means that the down-sloping orbitals which cross the Fermi surface hardly affect $J_{\text{band}}^{(2)}$, i.e. they contribute with a substantial angular momentum but leave the core essentially unchanged. If we follow the yrast states with only parity and signature fixed (upper curves in fig. 8), each band is only calculated in a small spin interval. It becomes therefore very difficult to extract $J_{\text{band}}^{(2)}$ with any numerical significance. This illustrates the usefulness of our calculational feature to keep N_{rot} as a preserved quantum number which makes it possible to specify a configuration in a much more precise way.

The contribution to $J_{\text{band}}^{(2)}$ from one filled orbital i can be expressed as

$$J_{\text{orb}(i)}^{(2)} = \frac{d(\langle j_x \rangle_i)}{d\omega}, \quad (29)$$

which is the curvature in a diagram like those of fig. 9. From these figures, it becomes evident that the strongly-aligned orbitals of $h_{9/2}$ and $i_{13/2}$ for the protons and $g_{9/2}$, $i_{11/2}$ and $j_{15/2}$ for the neutrons, show almost no curvature. The remaining spin is mainly supplied from other neutron orbitals which should thus be the orbitals which build up $J_{\text{band}}^{(2)}$. The spin from these orbitals is naturally referred to as the collective component while the strongly-downsloping orbitals build up an aligned spin component. It is these orbitals which supply the driving force towards positive γ -values [cf. refs.^{46,47)}]. One could argue that the orbitals which are emptied when the downsloping ones become occupied show a “negative” curvature which should contribute to $J_{\text{band}}^{(2)}$. However, this contribution is rather small and might also be counteracted by the small deformation changes.

The moment of inertia $J_{\text{band}}^{(2)}$ can be compared to $J^{(1)} = I/\omega$ which is typically $80 \hbar^2/\text{MeV}$ for $I = 20-40$ and even larger for $I = 40-50$. The fact that $J_{\text{band}}^{(2)}$ is only half as large as $J^{(1)}$ indicates once more that the collectivity in these bands is comparatively small. It is then interesting to compare with the strongly-deformed configuration c4 which has $J^{(1)} \approx J^{(2)} \approx 115 \hbar^2/\text{MeV}$, a value which is also close to the rigid-body moment of inertia for the deformation in question, $\varepsilon = 0.47$, $\gamma = 0^\circ$. The situation with the kinematical and dynamical moments of inertia equal is typical for such a large deformation. In a single-particle diagram, it corresponds to a structure where no orbitals cut through the Fermi surface as straight lines, i.e. no aligned angular momentum is brought into the system.

4.2. ALIGNED OR NEAR-ALIGNED STATES

Some of the most low-lying bands corresponding to the potential energy minima for ^{187}Au in the $-60^\circ - 120^\circ$ sector are shown in fig. 6b and the single-particle orbitals are given at a typical deformation in fig. 10. From the latter diagrams, one finds that even if the frequency is varied over large intervals ($\Delta\hbar\omega \sim 0.5 \text{ MeV}$), the total spin for one fixed band is only changed by a few units. This explains why the bands in fig. 6b have a rather peculiar behaviour, with a very large curvature. This curvature corresponds to a very small $J_{\text{band}}^{(2)}$, i.e. very small collectivity.

Some minima are also found at $\gamma = -120^\circ$ corresponding to ph excitations for prolate shape. The structure of these states are easily identified from the e_i versus m_i plots in fig. 11. The proton configurations of interest are $(s_{1/2}d_{3/2})^{-2}(h_{11/2})^{-1}$ with a spin of $\frac{15}{2}^-$ and $(d_{3/2})^{-1}(h_{11/2})^{-2}$ with $I^\pi = \frac{23}{2}^+$. The most important neutron configurations are $(f_{7/2}h_{9/2})^{-3}(i_{13/2})^9(p_{3/2})_0^2$ with $I^\pi = 34^-$ and $(f_{7/2}h_{9/2})^{-2}(i_{13/2})^8(p_{3/2})_0^2$ with $I^\pi = 24^+$ (if the spin value, given as a subscript, is omitted, the maximal spin is implied). If these proton and neutron configurations are combined it becomes possible to create the terminating states with $I^\pi = 31.5^-$, 41.5^+ and 45.5^- which are shown in fig. 6b.

The lowest state in the strongly curved bands in fig. 6b can often be identified with a ph configuration. For example, the configuration labelled ph2 comes

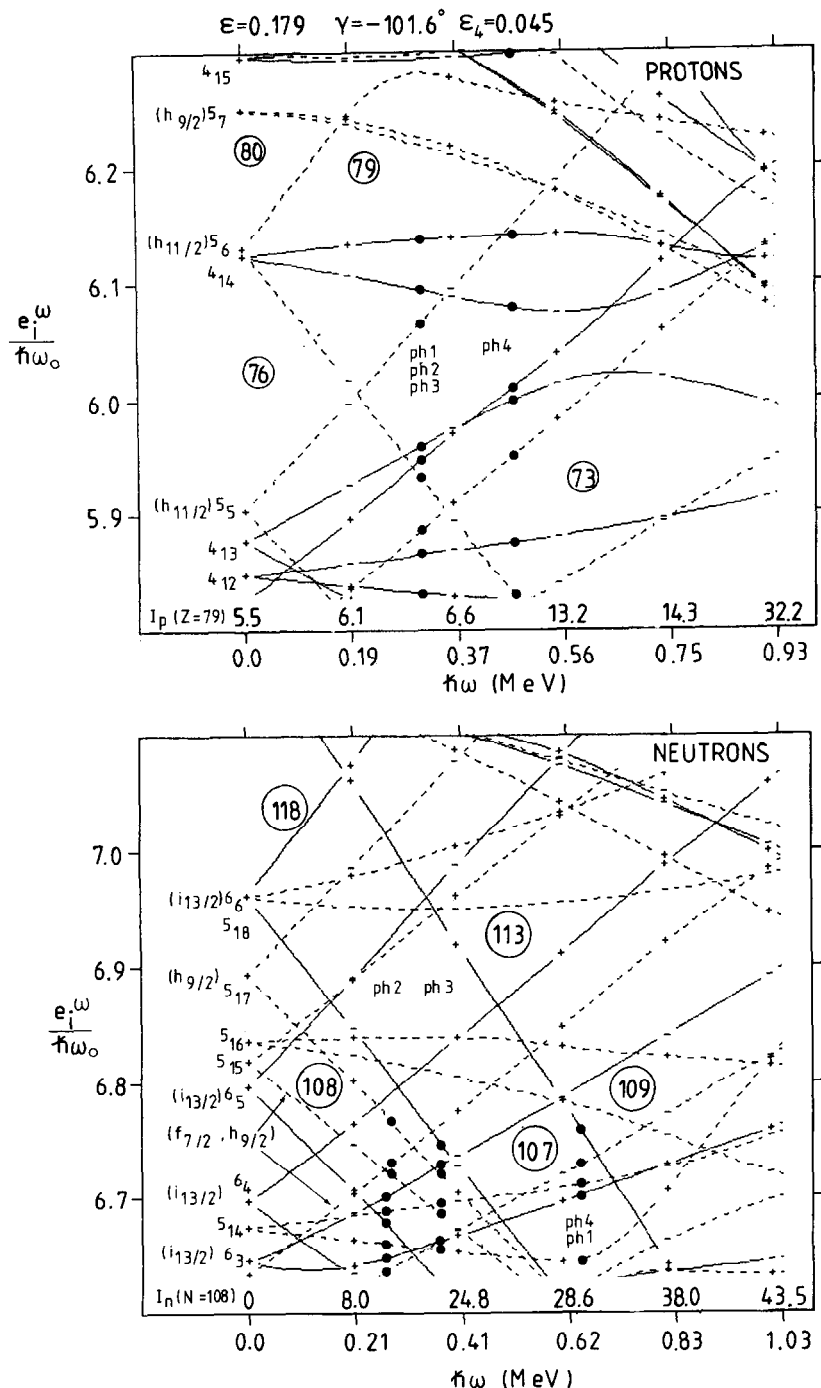


Fig. 10. Same as fig. 9, but for the deformation $\epsilon = 0.179$, $\gamma = -101.6^\circ$ and $\epsilon_4 = 0.045$. The orbitals which are occupied in the "particle-hole" configurations are indicated.

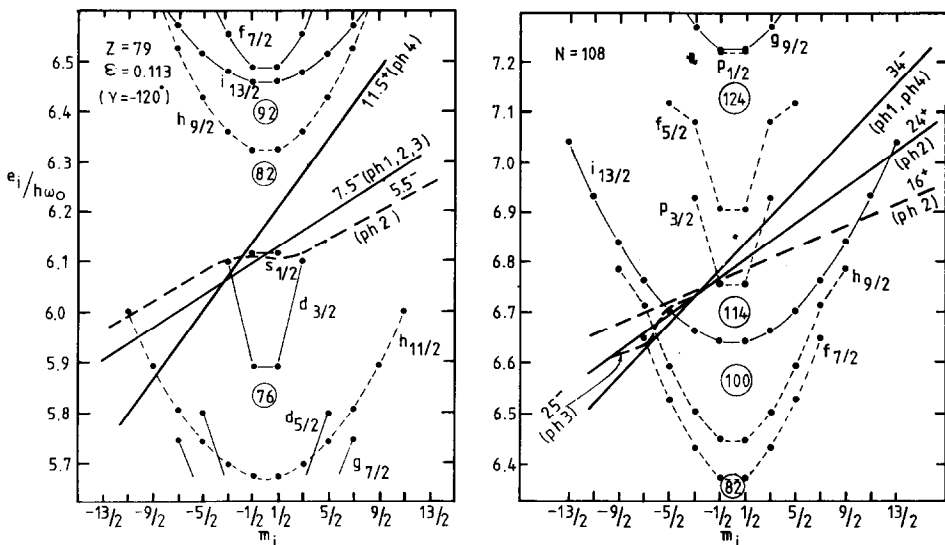


Fig. 11. Single-particle energies e_i plotted versus the spin component on the symmetry axis m_i for the deformation $\epsilon = 0.113$, $\gamma = -120^\circ$. Some configurations (see table 2) in the nucleus ^{187}Au are indicated by sloping Fermi surfaces. Full lines are used for states which are calculated to be of pure ph character, while dashed lines indicate the filling of j -shells for low-lying states which are slightly collective, cf. fig. 6b and fig. 10.

very low for $I^\pi = 21.5^-$ which is more or less formed as $\pi[(h_{11/2})^{-1}(s_{1/2})_0^{-2}]_{5.5} \times \nu[(h_{9/2}f_{7/2})_8^{-2}(i_{13/2})_8(p_{3/2})_0^2]_{16}$. Similarly, the 32.5^+ state in configuration ph3 could be identified with $\pi[(h_{11/2})^{-1}(s_{1/2}d_{3/2})^{-2}]_{7.5} \nu[(h_{9/2}f_{7/2})_{11.5}^{-3}(i_{13/2})_{13.5}^9(p_{3/2})_0^2]_{25}$. These configurations come from straight, or almost straight, line Fermi surfaces as shown by dashed lines in fig. 11. They are also indicated in fig. 10 while the occupation of the rotating N -shells is specified in table 2.

It is interesting to note that starting from such low-lying states of spin I which are not fully aligned it is possible to form both $I-2$ and $I+2$ states within the same band. This could be compared to the $I-2$ and $I+2$ γ -vibrational states which can be generated from aligned states with spin I [ref. ⁴⁸]. In the present approach which is purely based on cranking, it is only possible to find a related $I-2$ state for such a fully-aligned state (for example, the 41.5^- and the related 39.5^- states in conf. ph1 of fig. 6b).

The aligned prolate states for ^{187}Au can be understood as a manifestation of the coupling scheme discussed in ref. ⁴⁹). In this coupling scheme, the effect of the quadrupole deformation to destroy the spherical shell degeneracy is compensated by the rotational motion. This compensation is more or less independent of quadrupole deformation ϵ (or rotational frequency ω) if the ratio ϵ/ω is kept constant. For prolate shape, particle numbers corresponding to some holes in the spherical

shells or maybe rather in the high- j subshells get favoured. The nucleus $^{187}\text{Au}_{108}$ can be characterised by having three holes in the $Z = 82$ core (one or two holes in $h_{11/2}$) and six to eight holes in an “ $N = 114$ core” where the core is formed by the $i_{13/2}$, $h_{9/2}$ and $f_{7/2}$ subshells in addition to the subshells below $N = 82$. In fig. 3 of ref.⁴⁹⁾, the quasishell energy⁵⁰⁾, $\sum e_i^\omega - \langle \sum e_i^\omega \rangle$, is plotted for the ratio $\omega/\omega_0 = 0.75\epsilon$. One then observes that the valley of minimal “shell energy” passes through particle number 79 as well as 108 at the appropriate deformation $\epsilon = 0.11$. As the corresponding proton diagram is very similar, the two “shell-energy minima” being 2–3 MeV deep can be combined leading to a shell energy gain of 4–6 MeV for the prolate ph states of ^{187}Au at spins $I = 40$ –50. Indeed it seems that in the present case, a somewhat smaller ω/ϵ ratio would be even more favourable. Thus, the sloping Fermi surfaces in fig. 11 for $I_n^\pi = 34^-$ and $I_p^\pi = 11.5^+$, respectively, rather correspond to $\omega/\omega_0 = 0.6\epsilon$.

4.3. REMARKS ABOUT THE TWO COUPLING SCHEMES OF ^{187}Au

The difference in collectivity between the states of the two calculated coupling schemes of ^{187}Au might be possible to check experimentally. This difference should influence the total decay times in the two cascades which were identified experimentally in ref.⁴⁵⁾. In that reference, the “oblate” cascade was not observed for spins higher than $I = 30$ –35 while the prolate cascade was seen for spins up to 50–55. This is in qualitative agreement with the present calculations where the “collective” minimum survives to much higher spins than the “non-collective” one. As concerns the exact spin where the non-collective cascade is interrupted, the present calculations would suggest $I = 40$ –45, i.e. some minor difference compared to experiment. One could also note that for the neighbouring nucleus ^{186}Hg two coexisting bands have very recently been observed up to $I = 20$ [ref.⁵¹⁾]. This is in qualitative agreement with our results while the neglection of pairing in the present calculations exclude any quantitative comparison. One feature which is different in the two coupling schemes is the division of the total spin between protons and neutrons. In the more collective states, the proton spin reaches 15–20 units for very low rotational frequencies and then stays more or less constant up to $I = 40$ –50. For the less collective states, the proton spin is built only from the three holes in the $Z = 82$ core. This spin is then 5–7 units for $I < 30$ and it only reaches 10–12 units for $I = 30$ –50. The division of the total spin influences the magnetic moment (the g -factor) which should thus be different for the states of the two cascades.

5. Terminating bands

It is well known that it is only nuclei with a considerable number of nucleons outside the closed shells which show collective rotational bands at low spin. If

pairing is neglected and the corresponding deformation is not too large, the different nucleons can naturally be classified as belonging to specific j -shells. There is then a fixed number of nucleons in partly filled j -shells which mean that, if the distribution of particles over the j -shells is not changed, the total nuclear spin is limited. The classical example is ^{20}Ne [refs. ^{33,12}] with two protons and two neutrons in the $d_{5/2}$ subshell outside the ^{16}O core with the maximum spin of $2(\frac{5}{2} + \frac{3}{2}) = 8$. Furthermore, it has recently been predicted ¹⁵) that similar bands should be present in heavier nuclei, e.g. the nuclei with a few particles outside the $^{146}\text{Gd}_{82}$ core.

In the terminating state the spin vectors of all the valence nucleons are quantised along the same axis, the "rotation axis". This must mean that the whole nucleus is axially symmetric where the valence nucleons create an oblate shape. The same concepts can also be used for configurations with a few holes in valence shells in which case the nucleus is prolate in the terminating state (cf. subsect. 4.2 above).

Aligned nuclear configurations are most easily illustrated in e_i versus m_i diagrams [see e.g. ref. ¹⁵] where a diagram appropriate for the $A = 150-160$ region is given] but can also be identified with the help of standard single-particle diagrams such as those of figs. 2 and 3. In fig. 12 we illustrate how the ^{158}Yb $\alpha = 1$ branch of the $\pi[(d_{5/2})^{-1}(h_{11/2})^6(d_{3/2})^1]\nu[(f_{7/2}h_{9/2})^4(i_{13/2})^2]$ configuration becomes less and less collective with increasing spin and finally terminates at a fully-aligned state for $I'' = 47^+$. The corresponding trajectory in the (ϵ, γ) plane for this band and for a similar band in ^{158}Er [ref. ¹⁵] is depicted in fig. 13. The energies in the ^{158}Yb band can be read out from fig. 14. An important feature of this and other calculated terminating bands is that the energy cost per spin unit decreases when the terminating state is approached. In other words, in plots like that of fig. 14 the curvature often becomes negative corresponding to values of $J_{\text{band}}^{(2)}$ which are about as large or even larger than $J^{(1)}$. The terminating bands seem to be especially favoured in ^{158}Yb compared to other nuclei we have studied. For example, as seen in fig. 14, some terminating states in the $I = 40-50$ region are lowered by 1-1.5 MeV relative to the smooth trend for $I = 0-30$.

The first terminating states are calculated just above $I = 30$. It is then very interesting to note that an yrast cascade with essentially constant transition energy between 700 and 800 keV has very recently been observed in ^{158}Yb [ref. ⁵²]). Such a cascade is in close agreement with the calculated features of terminating bands ¹⁵). A possible candidate ⁵³) is the configuration shown in fig. 14 which terminates ~ 100 keV above yrast for $I = 36$.

One special kind of terminating bands are those where both the signatures are present with more or less no signature splitting. This seems to happen if there is one (or maybe a few) holes in specific j -shells. For example, for proton configurations with one hole in $d_{5/2}$ which terminate for $I = 40-50$ and $\epsilon = 0.10-0.15$ ($\gamma = 60^\circ$) the state with one hole in $d_{5/2,-5/2}$ is roughly as favoured as the state with one hole in $d_{5/2,-3/2}$. Examples of such bands are those which terminate for $I'' = 47^+$ and 48^+ in fig. 14. These kinds of bands were discussed for ^{158}Er in ref. ¹⁵) where it was

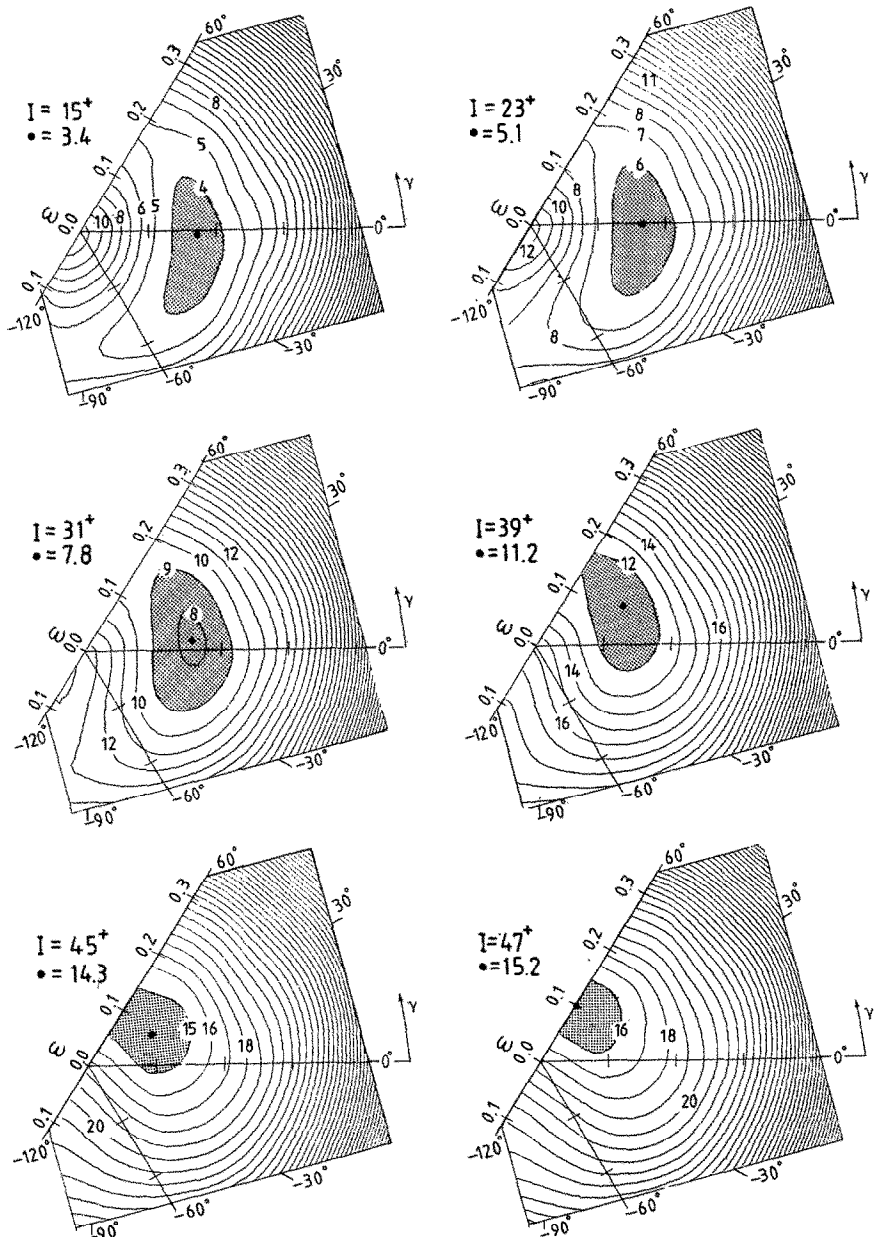
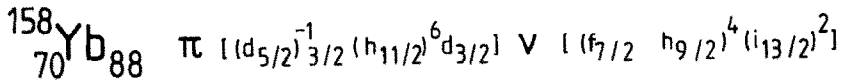


Fig. 12. Deformation energy surfaces as in fig. 5, but for the configuration terminating in the $\pi[(\text{d}_{5/2})^{-1}_{3/2}(\text{h}_{11/2})^6 \text{d}_{3/2}] \nu[(\text{f}_{7/2}\text{h}_{9/2})^4(\text{i}_{13/2})^2]$ state of the nucleus ^{158}Yb when it approaches termination at $I'' = 47^+$. For signature $\alpha = -1$, this is the maximal spin which can be extracted from the configuration. For signature $\alpha = 0$, a 48^+ state can be formed if the proton hole in $\text{d}_{5/2}$ is put in the orbital with spin projection $m_i = -\frac{5}{2}$ instead of $m_i = -\frac{3}{2}$.

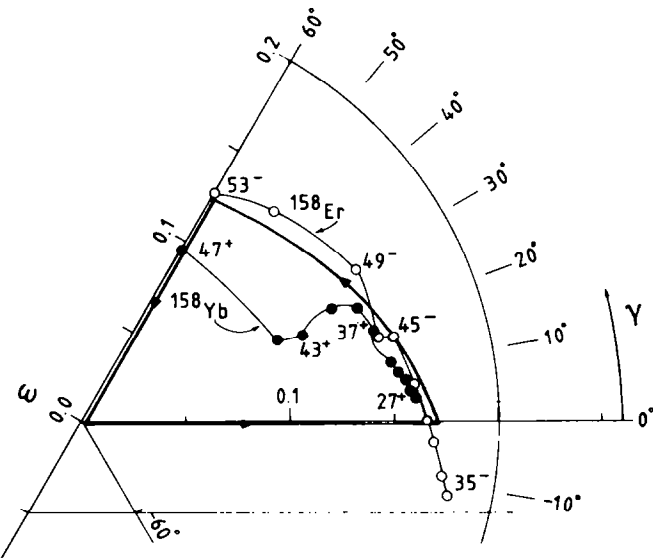


Fig. 13. Shape trajectories in the (ϵ, γ) plane for the configurations terminating in the states $\pi[(d_{5/2})^{-3/2}(h_{11/2})^6d_{3/2}] \nu[(f_{7/2}h_{9/2})^4(i_{13/2})^2]$ of ^{158}Yb and $\pi[(d_{5/2})^{-1}(h_{11/2})^5] \nu[(f_{7/2}h_{9/2})^3(i_{13/2})^3]$ of ^{158}Er . The configurations which are also illustrated in fig. 14 terminate for $I = 47$ ($I_p = 21$) and $I = 53$ ($I_p = 20$), respectively. The path followed in the single-particle diagram of fig. 15 is also illustrated.

speculated that they might be responsible for bumps of M1 transitions tentatively observed⁵⁴) in Yb nuclei.

For two bands with one hole in the $\alpha = \frac{1}{2}$ or $\alpha = -\frac{1}{2}$ branch of the highest $d_{5/2}$ orbital, it turns out that the signature splitting is very small for all spins. This is illustrated in fig. 15 where single-particle orbitals in the rotating system are illustrated. The deformation, ϵ , γ and ϵ_4 , and the rotational frequency ω is varied in such a way that the shape changes of the two configurations of fig. 13 in $^{158}_{68}\text{Er}_{90}$ and $^{158}_{70}\text{Yb}_{88}$ are roughly followed as a function of spin. The figure can, however, also be used as a general illustration of terminating bands in the $A = 150-160$ region of nuclei. An important feature in the figure is that for all values of γ , the signature splitting of the highest $d_{5/2}$ orbital is negligible. This then suggests that for bands with one hole in $d_{5/2}$, one should see both signatures with more or less no splitting all the way to their termination.

The signature splitting for the terminating states is strongly correlated to the (oblate) deformation. It is then interesting to note that the deformation where the two signatures become degenerate corresponds to an ω/ϵ ratio which was found in ref.⁴⁹) to give very strong shell effects. This is most easily seen from fig. 15 where for oblate deformation (far right), the ω/ϵ ratio is such that the upsloping levels in especially the $h_{11/2}$ subshell but also the $d_{5/2}$ and $g_{7/2}$ subshells are more or less degenerate for all values of ϵ (or ω). For a fixed value of ϵ ($\gamma = 60^\circ$), the same feature is seen in e_i versus m_i diagrams [fig. 4 of ref.¹⁵] from the fact that the

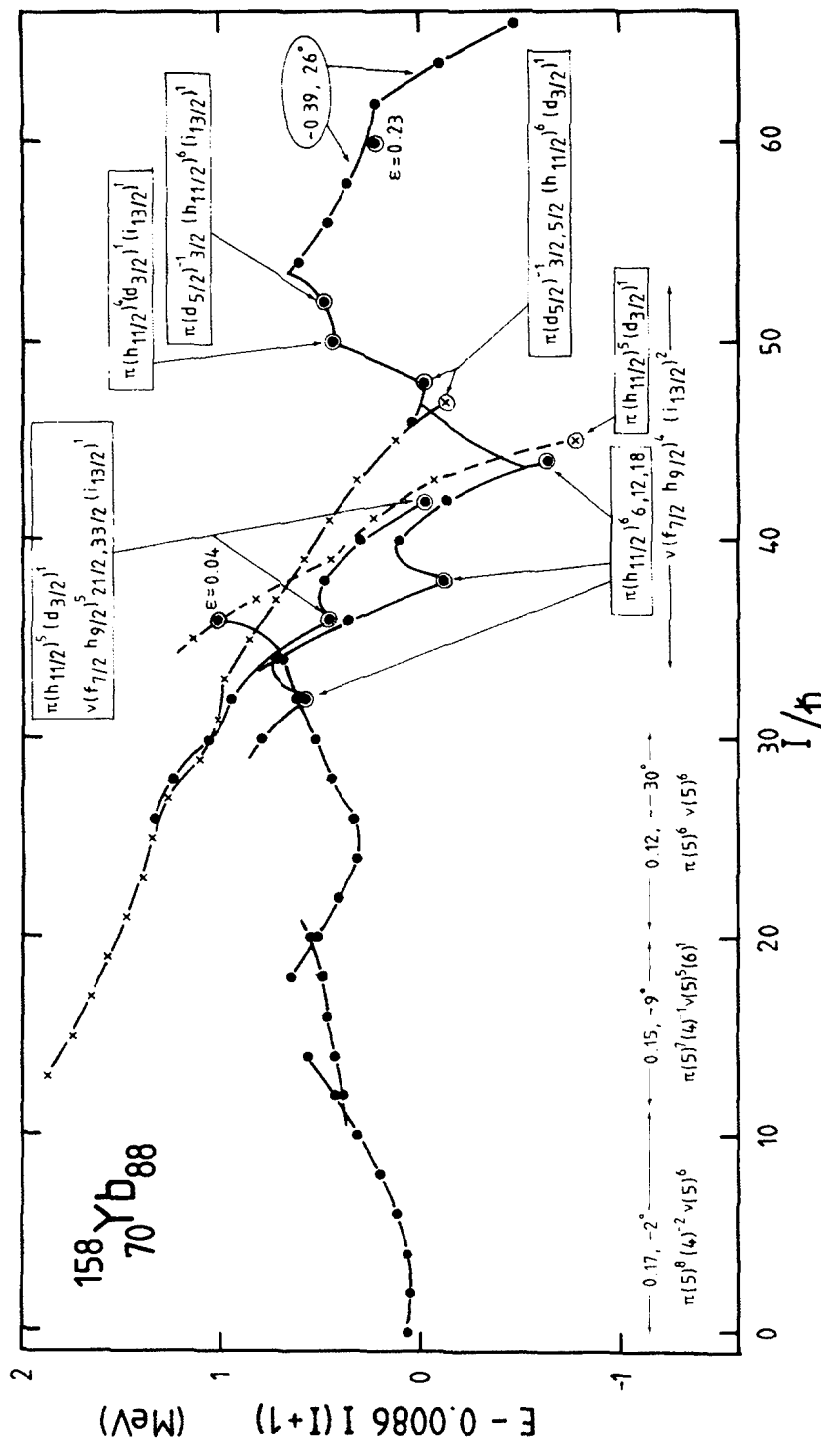


Fig. 14. Total energy as in fig. 6, but for the nucleus ^{158}Yb . The positive-parity $\alpha = 0$ yrast states are given and in addition two bands terminating for $I'' = 45^-$ and 47^+ . Also one very near yrast band which terminates for 36^+ (and 42^+) is shown. This band might be assigned to the $26^+ - 36^+$ yrast band of ^{158}Yb which is observed in discrete spectroscopy [22, 53]. Configurations are given relative to a ^{146}Gd core, either as occupation of N_{rot} shells, or for the terminating bands as occupation of j -shells. The deformation for the yrast bands at $I \leq 32$, ϵ and γ as given in the figure, is rather different for different bands which indicates a softness of the total energy surfaces. For $I = 40-50$, we calculate some strongly favoured band terminations at $\epsilon \approx 0.11$ (cf. figs. 12, 13). Most of these belong to the very favoured neutron configuration $\nu[(f_{7/2}h_{9/2})^4(i_{13/2})^2]$ which terminates for $I_n = 30$. Note especially the two bands which terminate at $I'' = 47^-$ and 48^+ . These bands, which are more or less equally favoured have the same configuration except for the signature of the $d_{5/2}$ hole. see fig. 15. For $I = 60$ there is a competition between superdeformed states ($\epsilon = 0.39$, $\gamma = 26^\circ$) and states of more or less pure particle-hole character.

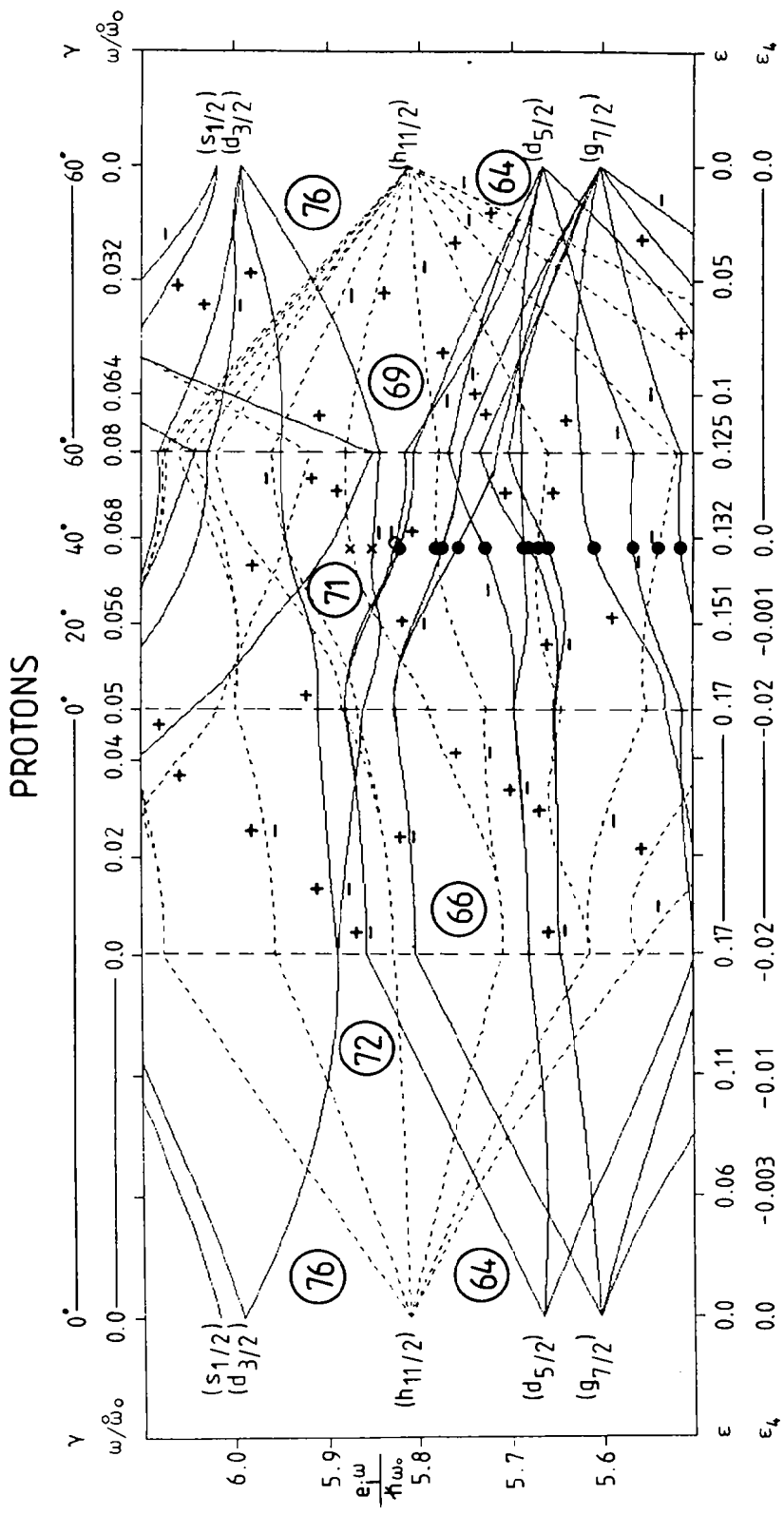


Fig. 15. Single-particle energies along the trajectory in the (ϵ, γ) plane shown in fig. 13 and for the ω and ϵ_4 values given on the abscissa. Starting from spherical shape, the static orbitals are first drawn for prolate shape up to $\epsilon = 0.17$. Then for constant deformation, the rotational frequency ω is increased up to $0.05\omega_0$ corresponding to total spin $I = 30-40$ for $A = 150$ nuclei. A trajectory in the (ϵ, γ) plane is then followed over to oblate shape ($\gamma = 60^\circ$) where, furthermore, ω increases slowly more or less as in the terminating bands illustrated in fig. 13. Finally, with a linear relation between ϵ and ω , $\omega/\omega_0 = 0.64\epsilon$, the static spherical orbitals are regained. In this part of the figure, one observes large degeneracies which are more or less independent of deformation. The occupied proton orbitals in the bands of ^{158}Yb and ^{158}Er illustrated in fig. 13 are also indicated. Note especially that with one hole (open circle) in $d_{5/2}$ the two signatures are approximately degenerate for more or less all spins up to the termination.

negative m_i orbitals in high- j subshells are all about as far away from the sloping Fermi surface. Similarly, the orbitals with negative m_i in the neutron $i_{13/2}$, $h_{9/2}$ and $f_{7/2}$ subshells show the same kind of degeneracy. In the present case, because the $N = 82$ gap is much larger than the $Z = 64$ gap, the neutron shell effects are much stronger than those for the protons. Thus, as found in fig. 3 of ref. ⁴⁹), there is a very deep shell-energy minimum at $\epsilon = 0.12$ ($\omega/\omega_0 = 0.09$) for $N = 90$ and for $\epsilon \approx 0.10$ ($\omega/\omega_0 = 0.075$) for $N = 88$. As seen in fig. 13, these ϵ -values are consistent with the calculated deformations in the 53^- and 47^+ terminating states of $^{158}\text{Er}_{90}$ and $^{158}\text{Yb}_{88}$.

6. One-dimensional continuum spectra

In this section, we will discuss a few cases where the methods described in sect. 2 facilitate the understanding of results from continuum γ -ray spectra.

6.1. THE NUCLEUS ^{118}Te : A CHANGE TO COLLECTIVE ROTATION AT VERY HIGH SPINS

The experimental information on ^{118}Te from ref. ⁵⁵) is taken as an example of a "bump" or pulse-height spectrum which in principle is related to the $J_{\text{eff}}^{(1)}$ moment of inertia. The experimental results can roughly be summarised as follows. When the input angular momenta is increased from $I \sim 30$ to $I \sim 55$, a bump appears in the unfolded γ -ray spectrum above 1.2 MeV, with an upper edge around 2.3 MeV. This bump is found to consist mainly of E2 transitions, which indicates a collective character of the nuclear states in this spin region, in contrast to the lower spin region, where the spin is mostly generated from particle-hole excitations.

The calculations which were first described in refs. ^{50,55-57}) are in general agreement with these data. It is found that the yrast states have an oblate deformation (spin built from ph excitations) for $I \leq 30$. Around this spin value, the yrast configurations become collective corresponding to prolate or, at somewhat higher spins, triaxial deformations. The collective states in this spin region would then be responsible for the bump observed in experiment.

In the present calculations, hexadecapole deformation ϵ_4 is fully accounted for while only the liquid-drop effects of ϵ_4 were considered in ref. ⁵⁷). Furthermore, the single-particle parameters κ and μ are somewhat different in the two cases. Even so, we find very much the same average behaviour of the yrast states, which means that for a general survey we can use the energy surfaces presented in ref. ⁵⁷). Then, with the methods described in the present paper, we are able to make a closer study of the different yrast or near-yrast bands.

In fig. 16, we plot the total energies for the calculated yrast states in the spin region $I = 20-60$. Furthermore, we give all rotational bands which can be identified in the four yrast cascades of different parity and signature. In the spin region $I = 30-45$, all yrast states are collective. For lower spin, most yrast states are of ph

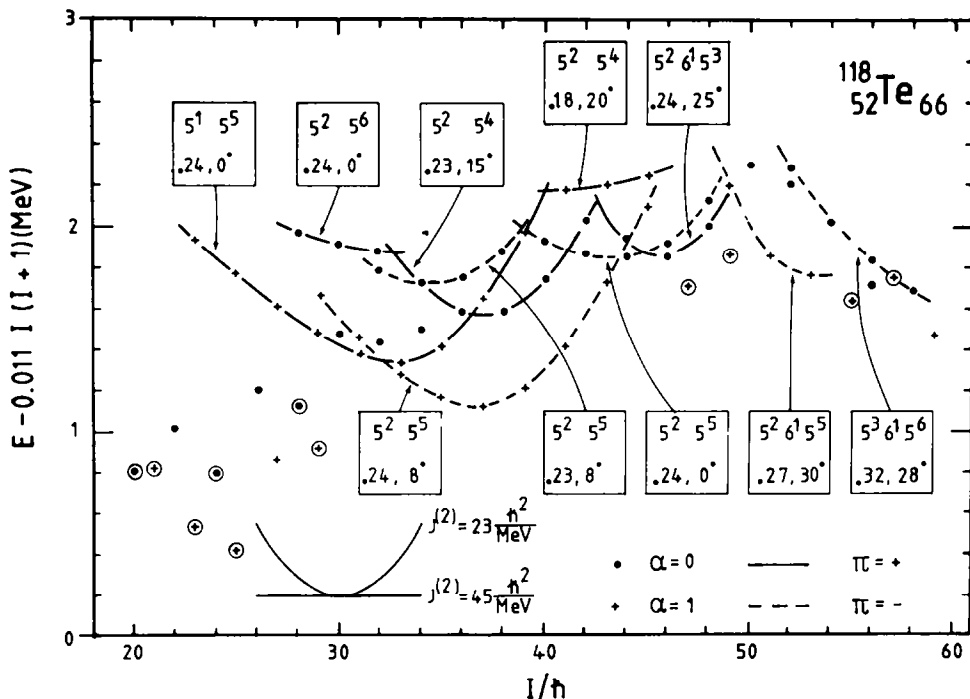


Fig. 16. Total energy $E(I)$ versus spin as in figs. 6 but for the yrast states of different parity and signature in the nucleus ^{118}Te . States marked with points have signature $\alpha = 0$, while those marked with plus signs have $\alpha = 1$. Full and broken lines connect bands of positive and negative parity, respectively. An average "liquid-drop" energy $0.011I(I+1)$ MeV has been subtracted. The lowest state for each spin and all bands of different parity and signature which become yrast for any spin are plotted. Aligned states at $\gamma = 60^\circ$ are encircled. The bands are labeled by the number of protons in the $N_{\text{rot}} = 5$ shell and the number of neutrons in $N_{\text{rot}} = 5$ and 6 (when occupied). Also approximate values of deformation, ϵ and γ , are given.

character while the collective bands go away from yrast and lose their identity. For $I \geq 45$, the yrast region is a mixture of collective bands and states of more or less pure ph character.

For $I = 40$, a $\pi = -, \alpha = +1$ band is about 0.5 MeV below all other bands. The deformation of the nucleus in this low-lying band is found to be $\epsilon \approx 0.24$, $\gamma \approx 8^\circ$ and $\epsilon_4 \approx 0.03$. In fig. 17 we show single-particle energies for a nearby deformation. One finds from this figure that a gap in the single-particle energies for 52 protons opens at high cranking frequencies, due to the occupation of the first two $h_{11/2}$ orbitals [cf. fig. 62 of ref. ⁵⁰]. Also for 66 neutrons a gap appears at high frequencies. The corresponding configuration has one neutron deexcited from an $N_{\text{rot}} = 5$ to an $N_{\text{rot}} = 4$ orbital. This deexcitation determines the parity and signature, $\pi = -$ and $\alpha = 1$, of the favoured band for $I = 40$.

"Transition energies" within the yrast $(-, 1)$ states are plotted in fig. 18, where also the continuation of the $\pi(h_{11/2})^2\nu(h_{11/2})^5$ band is shown. The yrast part of the

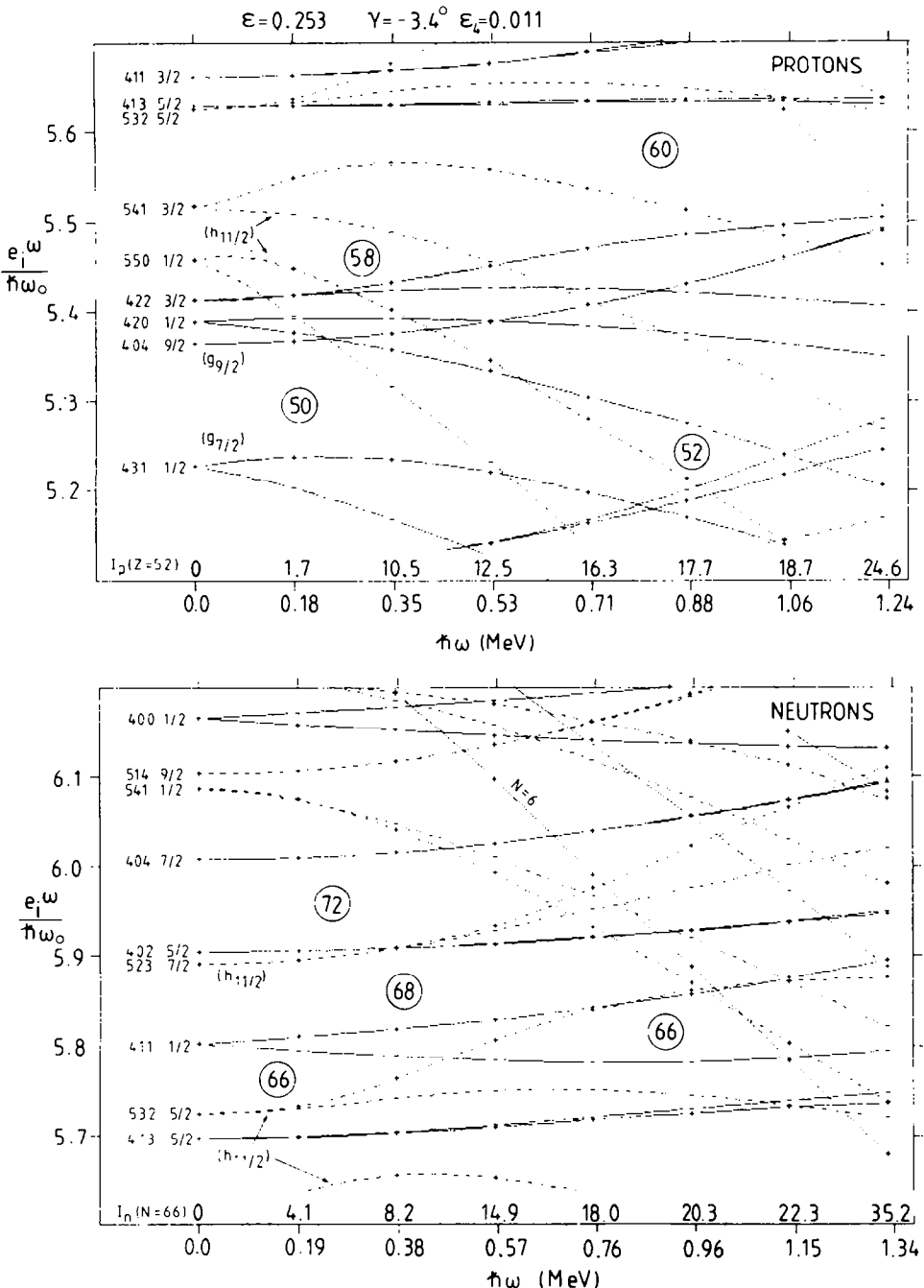


Fig. 17. Single-particle energies $e_i \omega$ as in fig. 9, but at the deformation $\varepsilon = 0.253$, $\gamma = -3.4^\circ$ and $\varepsilon_4 = 0.011$. At $\omega = 0$ the orbitals are labeled with the asymptotic quantum numbers $[Nn,\Lambda\Omega]$.

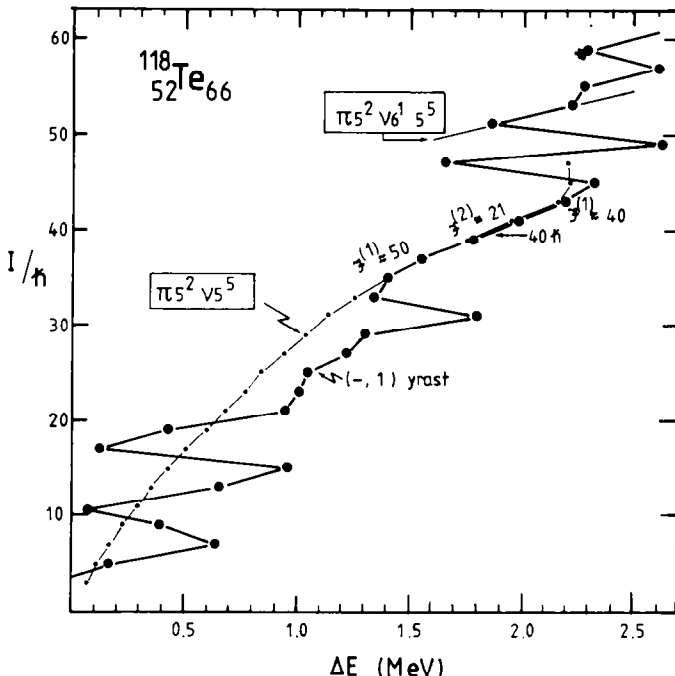


Fig. 18. Transition energies versus spin for the $(\pi, \alpha) = (-, 1)$ yrast cascade in ^{118}Te (filled circles). Note the regular behaviour between spins 33 and 45 in contrast to other spin regions, an effect of collective rotation. The corresponding collective configuration $\pi(h_{11/2})^2\nu(h_{11/2})^5$ is shown with small points over a wider region of spin. The difference between the two lines in the $I = 33-45$ region is caused by the different interpolations and gives some idea about the uncertainties in our calculations. Around $I = 50$, another collective configuration, $\pi(h_{11/2})^2\nu[(i_{13/2})^1(h_{11/2})^5]$, gives two yrast transitions.

latter cascade is found to be associated with transition energies between 1.4 and 2.2 MeV. In this figure, one also notes two transitions within the $\pi(h_{11/2})^2\nu(i_{13/2})^1(h_{11/2})^5$ band, $51^+ \rightarrow 49^+$ at 1.85 MeV and $53^+ \rightarrow 51^+$ at 2.2 MeV. Also for other calculated yrast bands at $I \geq 45$, the transition energies do not increase in general with spin but stay more or less constant below 2.2–2.3 MeV. This is due to the shape changes and backbends which occur, mainly when the first $i_{13/2}$ neutron orbital becomes occupied.

All the collective bands for $I \sim 40$ show rather similar features with deformations $\epsilon = 0.23-0.24$ and $\gamma = 0-10^\circ$. They all have 2 protons in $h_{11/2}$ and 4–6 neutrons in $h_{11/2}$. The proton state has a rather definite shell-model configuration $(g_{9/2})^{-2}(g_{7/2})^2(h_{11/2})^2$ corresponding to a maximum total proton spin of $I_p^\pi = 24^+$. The neutron configuration is less pure but the main components can be described as $(h_{11/2})^4(g_{7/2})^{-2}$ and $(h_{11/2})^6(g_{7/2})^{-4}$ (cf. fig. 3) with maximum total spin $I_n = 22$ and $I_n = 26$, respectively. This means that these bands can at most carry 45–50 units of angular momentum. Fig. 16 then shows that it is energetically rather expensive to get spin values close to this limit, i.e. the yrast bands have a relatively high energy

for $I = 45-50$. The shape changes within these bands are rather modest but not negligible. As a typical example, the $(-, 1)$ band which is yrast for $I = 33-43$ has a deformation of $\gamma \approx 0^\circ$ ($\epsilon \approx 0.26$) for $I = 27$ and $\gamma \approx 9^\circ$ ($\epsilon \approx 0.22$) for $I = 43$. However, neither this nor any other band in this spin region shows any real tendency to terminate in a ph state, i.e. to move all the way to $\gamma = 60^\circ$.

Around $I = 50$, states with one neutron in the $i_{13/2}$ subshell come down in the yrast region. The yrast bands then change their deformation towards $\epsilon \approx 0.30$ and $\gamma \approx 30^\circ$. One also notices that it becomes energetically less expensive to increase the spin in the bands, i.e. the lowest $i_{13/2}$ orbital gives rise to rather strong backbends. In the $I = 50-60$ region, there is also a strong competition from non-collective states of pure ph nature in the yrast region.

Our results explain in a very natural way the observed E2 bump for energies $\Delta E \approx 1.2-2.3$ MeV and spins $I \approx 30-55$. In the calculations, it is first for $I = 30$ corresponding to $\Delta E \approx 1.2$ MeV that the yrast states become collective. Then for $I = 45-50$ when the transition energies in the low-lying bands come close to $\Delta E = 2.3$ MeV, the backbend caused by the first $i_{13/2}$ neutron leads to transition energies which are lower than ~ 2.3 MeV also in the $I = 50-55$ region. If even higher spins could be populated, it seems that new backbends would keep the transition energies at more or less the same or even lower values than for $I = 45-55$. For the bands in the $I = 35-45$ region, the calculated $J^{(1)}$ moment of inertia varies in the $50-40 \hbar^2/\text{MeV}$ range while the $J_{\text{band}}^{(2)}$ moment of inertia comes out at around half this value. One also notes that within these bands, the $J_{\text{band}}^{(2)}$ moment of inertia shows a small decrease with increasing spin (cf. fig. 18). Discrete-spin spectroscopy for $I \geq 30$ would of course be very interesting and a severe test on our calculations. Also $\gamma\gamma$ -correlation experiments could give a lot of useful information about the nature of the rotational bands in the very-high-spin region $I \approx 30-55$. In subsect. 7.2 below, we will discuss a $\gamma\gamma$ -correlation experiment centered around the neighbouring nucleus ^{122}Xe .

6.2. EFFECTIVE MOMENT OF INERTIA

One can define the effective moment of inertia $J_{\text{eff}}^{(1)}$ for a nucleus, as the number $N(E_\gamma)$ of stretched E2 transitions (carrying away 2 units of angular momenta from the nucleus) below a certain transition energy E_γ , divided by this transition energy:

$$J_{\text{eff}}^{(1)}(E_\gamma) = 4 \frac{N(E_\gamma)}{E_\gamma}. \quad (30)$$

The corresponding $J_{\text{eff}}^{(2)}$ will then become

$$J_{\text{eff}}^{(2)}(E_\gamma) = 4 \frac{N(E_\gamma + \frac{1}{2}\Delta E) - N(E_\gamma - \frac{1}{2}\Delta E)}{\Delta E}, \quad (31)$$

and will thus be a measure of how much spin is carried away by E2 γ -rays in a certain energy interval ΔE around E_γ .

In ref.⁴⁰), a method to obtain $J_{\text{eff}}^{(2)}$ from experimental data was described, with applications to a few nuclei in the rare-earth region. To test the information obtainable from this experimental method, we derived in ref.¹⁶) a theoretical $J_{\text{eff}}^{(2)}$ from the calculated high-spin states as an average of the contributions from the four cascades with different parity and signature. A “smearing” procedure was introduced to approximately account for the experimental resolution [cf. eq. (4) of ref.¹⁶)]. A comparison between the experimental and calculated $J_{\text{eff}}^{(2)}$ values indicates that the rise of $J_{\text{eff}}^{(2)}$ found experimentally was correlated to a calculated rise due to a change to a very deformed shape (superbackbending).

The effective moment of inertia can thus provide insight into nuclear properties at spins where few other experimental quantities are available. When compared to $J_{\text{band}}^{(2)}$, it can also give important additional information about the nuclear structure. A large difference between the two quantities imply that the band structure is rapidly changing, since some transitions in different bands will have similar transition energies and thus contribute to make $J_{\text{eff}}^{(2)}$ larger than $J_{\text{band}}^{(2)}$.

7. Coincidence experiments and $J_{\text{band}}^{(2)}$

Plots of calculated transition energies versus spin, like figs. 8 and 18 above, are very useful when comparing calculations with experimental results obtained from $E_{\gamma} - E_{\gamma}$ coincidence experiments. Firstly, one can easily see whether there are any collective correlations at all, which is the case if the transition energies increase approximately linearly with spin. In such a case, the value of $J_{\text{band}}^{(2)}$ can be obtained from the slope of the I versus ΔE line. Secondly, changes of single-particle configuration or deformation are often manifested by backbends or possibly upbends in this type of plot.

7.1. VARIATION OF $J_{\text{band}}^{(2)}$ IN ^{106}Pd

Let us first study $J_{\text{band}}^{(2)}$ obtained from ref.⁵⁸), in which experiment the resultant nuclei are ^{106}Pd and a few of its neighbours. The valley is here visible up to $(\hbar\omega)^2 = 0.8 \text{ MeV}^2$ ($\Delta E = 1.8 \text{ MeV}$) and the $J_{\text{band}}^{(2)}$ value deduced from the width of the valley shows some variations. Between 0.1 and 0.3 MeV^2 it increases from ~ 20 to $35 \hbar^2/\text{MeV}$, while at 0.4 MeV^2 it has dropped to $\sim 23 \hbar^2/\text{MeV}$, just to start a rise to a maximum of $35 \hbar^2/\text{MeV}$ at 0.6 MeV^2 . Above this frequency, $J_{\text{band}}^{(2)}$ assumes a rather constant value of $26 \hbar^2/\text{MeV}$. The first rise is correlated with the change in moment of inertia below the first backbend in the observed discrete lines.

In our calculations for ^{106}Pd some different yrast configurations terminate for spherical or near-spherical shape in the $I = 30-40$ region. Then, by the help of fig. 2, it is possible to conclude that a very favourable and stable proton configuration must be the one with 4 holes in $g_{9/2}$ corresponding to a maximal spin $I_p'' = 12^+$. For the neutron configurations, it is natural to classify them according to

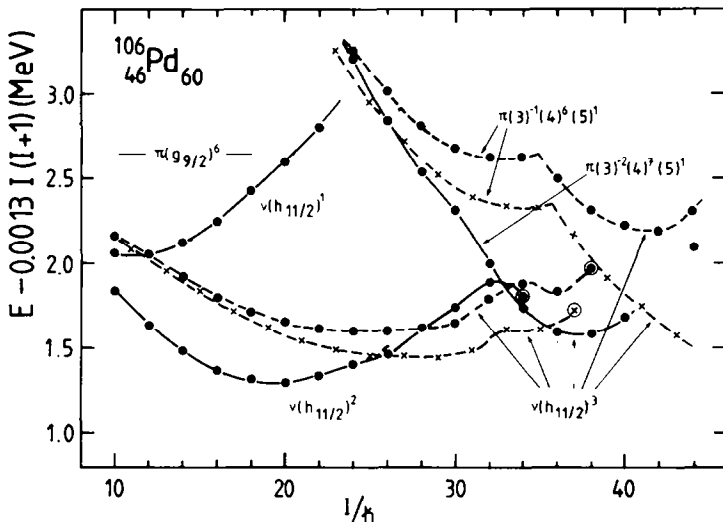


Fig. 19. Energies of the yrast bands of ^{106}Pd in the $I = 10\text{--}40$ region relative to an $I(I+1)$ reference. Positive- and negative-parity bands are drawn with full and dashed lines, respectively. Dots are used for states with $\alpha = 0$ and crosses for $\alpha = 1$. Aligned states are encircled. No $(\pi, \alpha) = (+, 1)$ bands are shown because all such bands are relatively high in energy. For the proton configurations, the number of particles in subshells or principal shells are given relative to a $Z = 40$ core. Only the number of particles in the $h_{11/2}$ subshell is indicated for the neutrons. The irregular behaviour close to the band termination of the $\pi(g_{9/2})^6$ bands is not numerically significant. The band crossings at $I = 30\text{--}36$ in the configurations with one proton in $h_{11/2}$ (i.e. one proton in $N = 5, (5)^1$) occur when one proton is lifted from $g_{9/2}$ to $g_{7/2}$.

the number of particles in $h_{11/2}$. With one, two and three particles in this subshell, the favoured aligned states are $[(d_{5/2})^5(g_{7/2})^4(h_{11/2})^1]_{16^-}$, $[(d_{5/2})^4(g_{7/2})^4(h_{11/2})^2]_{22^+}$ and $[(d_{5/2}g_{7/2})^7_{23/2,25/2}(h_{11/2})^3]_{25^-, 26^-}$, respectively (fig. 3). As illustrated in fig. 19, the full calculations give that the bands with two and three neutrons in $h_{11/2}$ are yrast for their respective parity and signature in a large spin interval, and that the terminating states with $I^\pi = 34^+$ and $37^-/38^-$, respectively, are very close to yrast. The shape changes within the bands are illustrated in fig. 20.

Higher spins in ^{106}Pd are formed if protons are lifted above the $Z = 50$ gap, from either the $f_{5/2}$ or $g_{9/2}$ subshells to the $g_{7/2}$ or $h_{11/2}$ subshells, see fig. 2. Some typical bands of this type which are yrast or near-yrast in the $I \approx 40$ region are also shown in fig. 19 while their deformation trajectories are given in fig. 20. The excitation across the $Z = 50$ gap will generally give rise to strong driving forces towards positive γ leading to triaxial deformations in these configurations. The band crossings observed for $I \geq 30$ in these three configurations occurs when one proton is lifted from a $g_{9/2}$ orbital to the most low-lying $g_{7/2}$ orbital.

In the experimental study of ref.⁵⁸), it was found that the moment of inertia $J_{\text{band}}^{(2)}$ varies rather strongly with frequency and these variations were discussed within the present formalism. As the band structure along the yrast line changes rather

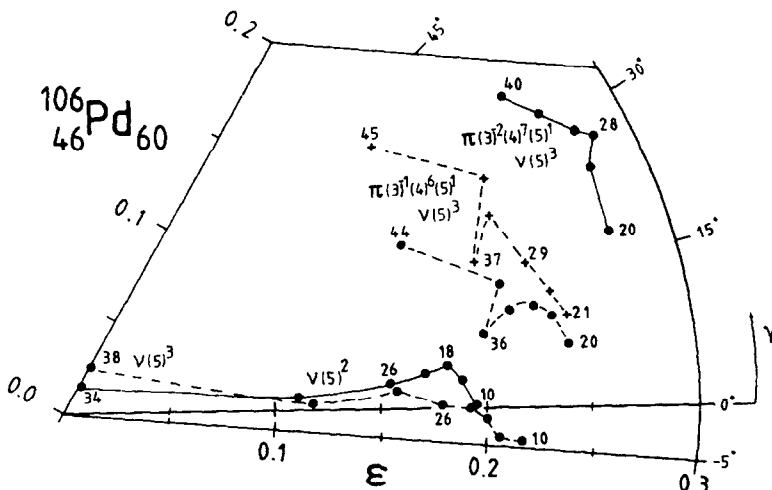


Fig. 20. Shape trajectories in the (ϵ, γ) plane for the bands of ^{106}Pd which were also depicted in fig. 19. The states are shown in steps of $4 \hbar$. As the two bands terminating for $I^\pi = 37^-, 38^-$ have very similar trajectories, the $\alpha = 1$ band is omitted.

much with spin, the variation seems natural. It also seems that the variation can be quantitatively understood. For $I = 20$ where the present calculations with no pairing might become realistic, the dominating yrast band is the one with two neutrons in $h_{11/2}$. For this spin the curvature is rather large corresponding to a small $J_{\text{band}}^{(2)}$ of approximately $27 \hbar^2/\text{MeV}$. Then with increasing spin, when this band approaches termination, the energy cost per spin unit becomes smaller, i.e. a smaller curvature in fig. 19 with $J_{\text{band}}^{(2)} \geq 30 \hbar^2/\text{MeV}$. For spins above $30 \hbar$ one expects this terminating band to loose its collectivity and the yrast cascade would then rather follow the $\nu(h_{11/2})^3$ bands for a few spin values. At even higher spins the $\pi(h_{11/2})^1$ bands should dominate the cascades (cf. fig. 19). Both types of bands ($\nu(h_{11/2})^3$ and $\pi(h_{11/2})^1$) have a smaller $J_{\text{band}}^{(2)}$, in general agreement with the experimental results⁵⁸. For the $\pi(h_{11/2})^1$ bands, the much smaller $J_{\text{band}}^{(2)}$ [$15-24 \hbar^2/\text{MeV}$, compared to $\sim 26 \hbar^2/\text{MeV}$, for the observed highest spins⁵⁸] is correlated with the large positive γ -values.

When comparing theory and experiment for ^{106}Pd , one should be aware of the large uncertainties in both cases. The experimental data are averages over a number of nuclei which, however, seem to have rather similar high-spin properties. Theoretically, the relative energies of the rotational bands are rather uncertain as they strongly depend on the exact position of the different j -shells. The properties within a band should be more stable but in this case one must remember that the $J_{\text{band}}^{(2)}$ moment of inertia is extracted as a second derivative and is as such sensitive to small variations in the rotational behaviour. We think, however, that this nucleus shows some interesting properties and it would be valuable to pursue both the $E_\gamma - E$ correlation and the discrete-spin spectroscopy to higher spins.

7.2. DIFFERENCES IN ROTATIONAL MODES

Significant differences between the behaviour of $J_{\text{band}}^{(2)}$ in ^{128}Ba and ^{122}Xe have been reported in refs.^{59,60}). In ^{128}Ba , $J_{\text{band}}^{(2)}$ is found to assume a value of about $40 \hbar^2/\text{MeV}$ above $\hbar\omega = 0.45 \text{ MeV}$, with a slight tendency to increase at the highest frequencies ($\sim 0.62 \text{ MeV}$), whereas in ^{122}Xe , $J_{\text{band}}^{(2)}$ assumes a rather low constant value ($\sim 25 \hbar^2/\text{MeV}$) between the rotational frequencies 0.45 and 0.65 MeV.

It is well known that nuclei in this mass region are relatively soft towards γ -deformation^{61,62}) and this softness is calculated to survive to quite high-spin values^{5,9}). It thus seems reasonable that the yrast deformation of these two nuclei is rather different. Indeed, with our single-particle parameters, ^{122}Xe is found to have most of its yrast states on the oblate axis (non-collective rotation). There are, however, also minima corresponding to yrast or near-yrast configurations at $\epsilon = 0.25$, $\gamma = 30\text{--}40^\circ$ and $\epsilon = 0.29$, $\gamma = 0^\circ$. In our labelling, more or less the same configurations, $\pi(h_{11/2})^{1,2} \nu(h_{11/2})^{4,5,6}$, are found at these two minima. A closer inspection reveals however, that the triaxial bands can be described as having no holes in the $g_{9/2}$ proton subshell while the prolate have two holes in this subshell (cf. fig. 2). For the $\gamma = 30\text{--}40^\circ$ bands, we calculate typical values of $J_{\text{band}}^{(2)} \leq 30 \hbar^2/\text{MeV}$ while $J_{\text{band}}^{(2)}$ is larger for the prolate bands. Thus, on the basis of the measured $J_{\text{band}}^{(2)}$ values, we would draw the conclusion that the yrast bands in the $I = 20\text{--}30$ region are built from triaxial configurations with no holes in the proton $g_{9/2}$ subshell. Above $\hbar\omega \sim 0.7 \text{ MeV}$ the prolate bands begin to show a decreasing $J_{\text{band}}^{(2)}$ because of the alignment processes in the valence orbitals are almost completed at this high spin, cf. the discussion below and figs. 17, 21. In subsect. 6.1, we discussed similar prolate bands in the neighbouring nucleus ^{118}Te , with small value of $J_{\text{band}}^{(2)}$ for spins above 35. This small value for ^{118}Te is thus consistent with the behaviour of prolate bands in ^{122}Xe in the same spin region.

Collective bands with $\epsilon \leq 0.27$ in $^{128}\text{Ba}_{72}$ are calculated to have $J_{\text{band}}^{(2)} \leq 35 \hbar^2/\text{MeV}$, which means that they cannot account for the high observed values. There are, however, bands with a larger prolate deformation, $\epsilon = 0.34$, which are calculated to become yrast above spin 40, but are only 0.4 MeV above yrast at spin 24. In fig. 21 the single-particle energies at this deformation are shown. Both $Z = 56$ and $N = 70$, 72 are seen to be in a region of rather low level-density at this deformation. The high-spin bands in ^{128}Ba will have two or three protons in $N_{\text{rot}} = 5(h_{11/2})$ orbitals and none, one or two neutrons in $N_{\text{rot}} = 6(i_{13/2})$ orbitals. The last occupied $N_{\text{rot}} = 5$ orbitals, [541 1_2], for neutrons have an admixture of $h_{9/2}$ and $f_{7/2}$ components while those orbitals ([523 7_2], cf. fig. 3) that are emptied by excitations to $i_{13/2}$ are mainly of $h_{11/2}$ nature. The mentioned orbitals behave differently as a function of cranking frequency. The energy of the $i_{13/2}$, [660 1_2], orbitals decreases essentially linearly with spin while when drawn as in fig. 21, the other orbitals show a curvature. This curvature is a result of a varying $\langle j_x \rangle$, and one might express this variation as an orbital moment of inertia, $J_{\text{orb}(i)}^{(2)}$, for orbital i as in eq. (29) above. The change of

$$\varepsilon = 0.33 \quad \gamma = 1^\circ \quad \varepsilon_4 = 0.058$$

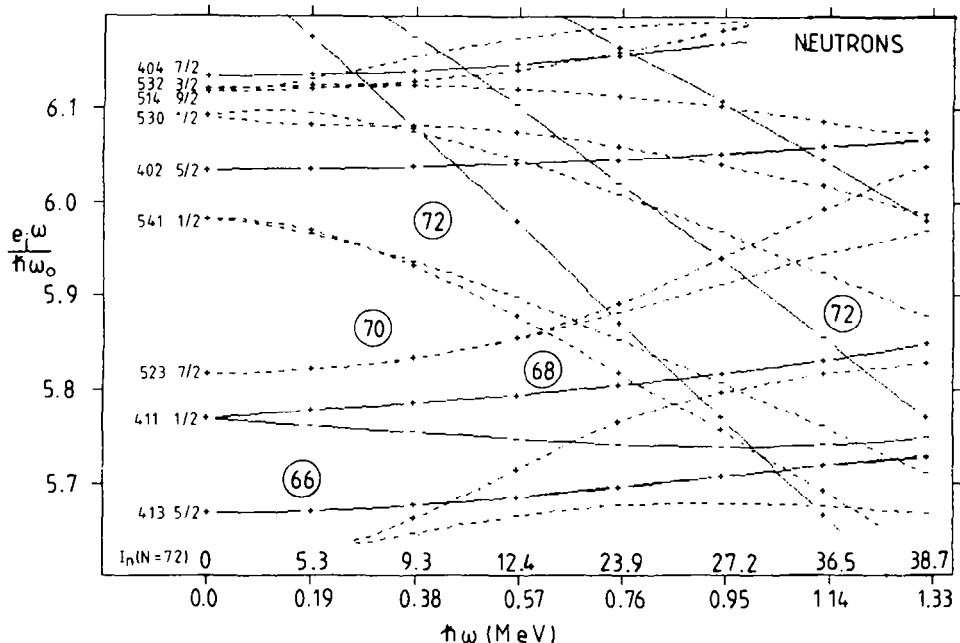
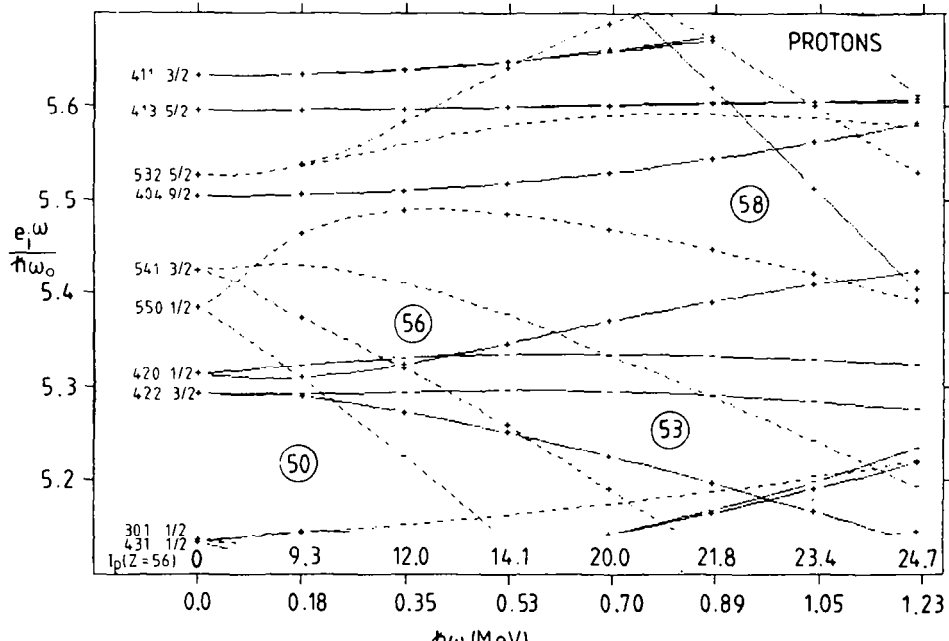


Fig. 21. Single-particle energies as in fig. 9, but at the deformation $\varepsilon = 0.33$, $\gamma = 1.0^\circ$ and $\varepsilon_4 = 0.058$.

TABLE 3

$J_{\text{orb}}^{(2)}$ contribution at $\hbar\omega = 0.6$ MeV for some neutron single-particle orbitals in fig. 21

Orbital	$J_{\text{orb}}^{(2)} [\hbar^2/\text{MeV}]$	
$[541\frac{1}{2}]$	$\left\{ \begin{array}{l} \alpha = +\frac{1}{2} \\ \alpha = -\frac{1}{2} \end{array} \right.$	2.0 1.5
	$\left\{ \begin{array}{l} \alpha = +\frac{1}{2} \\ \alpha = -\frac{1}{2} \end{array} \right.$	-4.5 -2.0
$[660\frac{1}{2}]$	$\alpha = +\frac{1}{2}$	0.5

$J_{\text{band}}^{(2)}$ caused by a particle-hole excitation from orbital i to orbital k can then be expressed as

$$\Delta J_{\text{band}}^{(2)} = J_{\text{orb}(k)}^{(2)} - J_{\text{orb}(i)}^{(2)}. \quad (32)$$

Thus we find that the $[541\frac{1}{2}]$ orbitals have a large positive $J_{\text{orb}}^{(2)}$ as their $\langle j_x \rangle$ is increasing, whereas the $[523\frac{7}{2}]$ orbitals have a negative $J_{\text{orb}}^{(2)}$ and that for $i_{13/2}$ orbitals is essentially zero. At $\hbar\omega \approx 0.6$ MeV we calculate the approximate values in table 3. The deformation of the nucleus in the single-particle configurations mentioned above, is calculated to be relatively stable around the deformation of fig. 21. Thus we expect that the excitation of one neutron from the $[523\frac{7}{2}]$, $\alpha = +\frac{1}{2}$ to the $[660\frac{1}{2}]$, $\alpha = +\frac{1}{2}$ orbital should be associated with an increase of $J_{\text{band}}^{(2)}$ by about five units. A similar situation occurs when a proton is excited to the third $h_{11/2}$ orbital as, also in this case, the orbital from which the proton is excited, $[420\frac{1}{2}]$ $\alpha = \frac{1}{2}$, shows a negative $J_{\text{orb}}^{(2)}$. These estimates are roughly borne out in the more detailed calculations, which give $J_{\text{band}}^{(2)} \approx 35, 38$ and $40 \hbar^2/\text{MeV}$ for the configurations $\pi(h_{11/2})^2\nu(h_{9/2})^2$, $\pi(h_{11/2})^3\nu(h_{9/2})^2$ and $\pi(h_{11/2})^3\nu[(h_{9/2})^2i_{13/2}]$, respectively.

These values are in reasonable agreement with the experimental ones. From fig. 21, it is apparent that this large deformation should be even more favoured in ^{130}Ce , where the discrete spectrum is discussed in subsect. 8.4 below. Thus the increase of $J_{\text{band}}^{(2)}$ associated with the occupation of high- j orbitals should occur in a similar way. Indeed, large values of $J_{\text{band}}^{(2)}$ have been observed in ^{130}Ce , as reported in ref.⁶³⁾.

7.3. OTHER FEATURES IN COINCIDENCE EXPERIMENTS

Not only the width of the valley that eventually appears in $E_\gamma - E_\gamma$ correlation experiments, but also fillings and disappearances of the valley can yield important information about the nuclear structure in the very-high-spin region.

A filling of the valley is caused by a number of transitions that have roughly the same energy. Thus, the corresponding calculated yrast lines should show upbends

or backbends if plotted as spin versus transition energy. Few such cases have hitherto been studied with the present theoretical method, mainly due to the lack of experimental observations at high enough energy. In refs.^{14,17)} however, we discuss the observation of "stripes"⁶⁴⁾, i.e. fillings that are also in coincidence with many transitions at lower energy. The difference between stripes and fillings of the valley is mostly due to different methods of subtracting the uncorrelated background. The stripes appeared in ¹⁶⁶Yb and some other rare-earth nuclei around the transition energy 1.2 MeV. In our calculations for nuclei in this mass region, we often find that $h_{9/2}$ and $i_{13/2}$ proton orbitals become occupied around spin 35–45, resulting in many transitions with almost the same energy somewhere in the interval 1.0–1.25 MeV (cf. the transition energy plots in subsect. 8.1). Furthermore, recent data from the TESSA II instrument at Daresbury⁶⁵⁾, show fillings of the valley between 1.2 and 1.38 MeV. The valley can be followed up to 1.42 MeV in this experiment where ¹⁶⁸Yb is the main residual nuclei. As seen in fig. 23 below, we calculate backbends from the occupation of $h_{9/2}$ and $i_{13/2}$ orbitals to occur in this region of transition energy for ¹⁶⁸Yb.

Thus the observation of stripes and fillings in $E_y - E_y$ correlation plots can possibly be connected to the occupation of proton $h_{9/2}$ and/or $i_{13/2}$ orbitals. As will be discussed in sect. 8, discrete-line spectroscopy has now reached such a stage of refinement, that discrete lines are observed up to the spins where we predict that this change of configuration will take place.

Another interesting, although difficult, perspective in correlation experiments is that it should in principle be possible to get a measure of how much of the deexciting cascade that goes through collective rotational states in different regions of spin. The main difficulty is probably that this would require careful normalization of the entire correlation matrix. A decrease in the collective correlations would then indicate that a substantial part of the cascade goes through particle-hole excited states, which would give valuable insight in the oblate-prolate energy difference. It would thus be an independent test of the theoretical predictions [sect. 5 and refs.^{15,16,9)}] and experimental indications^{66,54)} of changes from collective rotation to particle-hole excitations in neutron-deficient rare-earth nuclei as the spin increases.

8. Discrete states

In this section we will present comparisons between experimentally obtained and calculated high-spin states for a few nuclei. Here we are mainly interested in how well we can reproduce the experimental spectra. Failure or success in this respect should help to draw conclusions about how important residual interactions, i.e. pairing, might be. Furthermore, some information about the position of single-particle orbitals can be obtained from such a comparison.

8.1. THE NUCLEI ^{168}Yb , ^{168}Hf AND ^{165}Yb : PURE ROTATIONAL BANDS AND STABLE DEFORMATIONS

These nuclei are calculated to keep their deformation almost fixed around $\epsilon = 0.23\text{--}0.27$ and $\gamma \approx 0^\circ$ up to spins $I \approx 60$ (see insert of fig. 23 below). The single-particle orbitals for a typical deformation, $\epsilon = 0.253$ and $\gamma = -3.4$, are shown in fig. 22. In this figure, ϵ_4 is chosen equal 0.03 while the same plot with $\epsilon_4 = 0.011$ was published in ref.¹⁴). The present value of ϵ_4 is chosen to be optimal for ^{168}Yb , while in e.g. ^{168}Hf ϵ_4 varies in the range 0.01–0.02. The rather large $Z = 70$ gap in fig. 22 suggests a quite stable proton configuration with 8 protons in $h_{11/2}$. For the neutrons, positive-parity configurations can be formed from 6 or 4 particles in $i_{13/2}$. However, the $N = 98$ gap for $\hbar\omega$ values larger than ~ 0.2 MeV leads to calculated yrast configurations of negative parity (5 neutrons in $i_{13/2}$) for a large spin interval.

Some bands of ^{168}Yb have been observed up to quite high spin⁶⁷), the ground band to 38^+ and two negative-parity bands to 39^- and 30^- , respectively. Additionally, one band with spin and parity unidentified is also seen above $I = 30$. For a general comparison between theory and experiment, we give in fig. 23 transition energies for the three combinations of spin and parity which are most low-lying both theoretically and experimentally. For spins larger than $I = 20\text{--}25$, the agreement between theory and experiment is certainly very satisfying. Not only the transition energies, i.e. the moment of inertia $J^{(1)}$, but also the slopes, i.e. $J_{\text{band}}^{(2)}$, are roughly reproduced by our calculations. One could also observe that the $(+, 0)$ and $(-, 1)$ bands have been observed up to spin where we predict a strong backbend when the first $h_{9/2}$ proton becomes occupied. Such a backbend could make it considerably more difficult to extend the experimental studies to higher spins. Thus, it may explain why no higher spin states have been observed.

As we have pointed out before^{14,16}), a second backbend due to the occupation of the first $N_{\text{rot}} = 6$ $i_{13/2}$ proton orbital is predicted at more or less the same frequency as the $h_{9/2}$ backbend. One should note that these calculated backbending frequencies are rather uncertain as they depend strongly on the position of the $h_{9/2}$ and $i_{13/2}$ proton subshells in the single-particle spectra. However, as was pointed out in subsect. 7.3, experimental observations suggest that one or several backbends occur around these frequencies. The first really drastic shape change in ^{168}Yb occurs for $I \geq 60$. The calculated deformation in the resulting superdeformed state is $\epsilon = 0.40\text{--}0.42$ and $\gamma = 20\text{--}25^\circ$.

The comparison between theory and experiment in fig. 23 is done on an absolute scale with no parameter fitting whatsoever. We now also want to discuss the relative energies of the bands and we will then use the $(+, 0)$ ground band as a reference. It turns out that for $I \geq 20$, this band is very accurately described by

$$E(I) = \text{const} + \frac{\hbar^2}{2J} I(I+1), \quad (33)$$

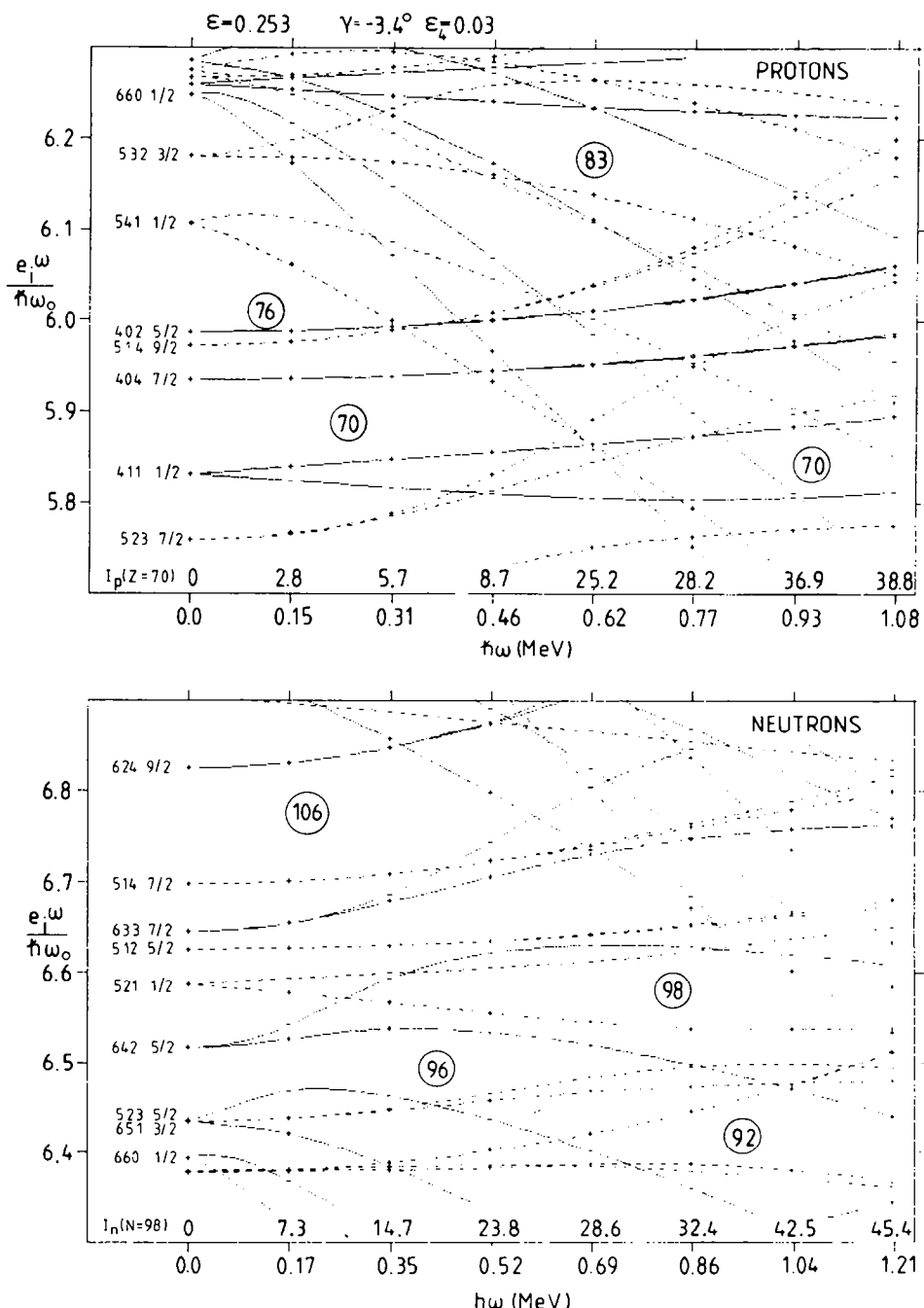


Fig. 22. Single-particle energies as in fig. 17, but with ϵ_4 slightly increased and now showing the appropriate orbitals for $Z \approx 70$, $N \approx 96$.

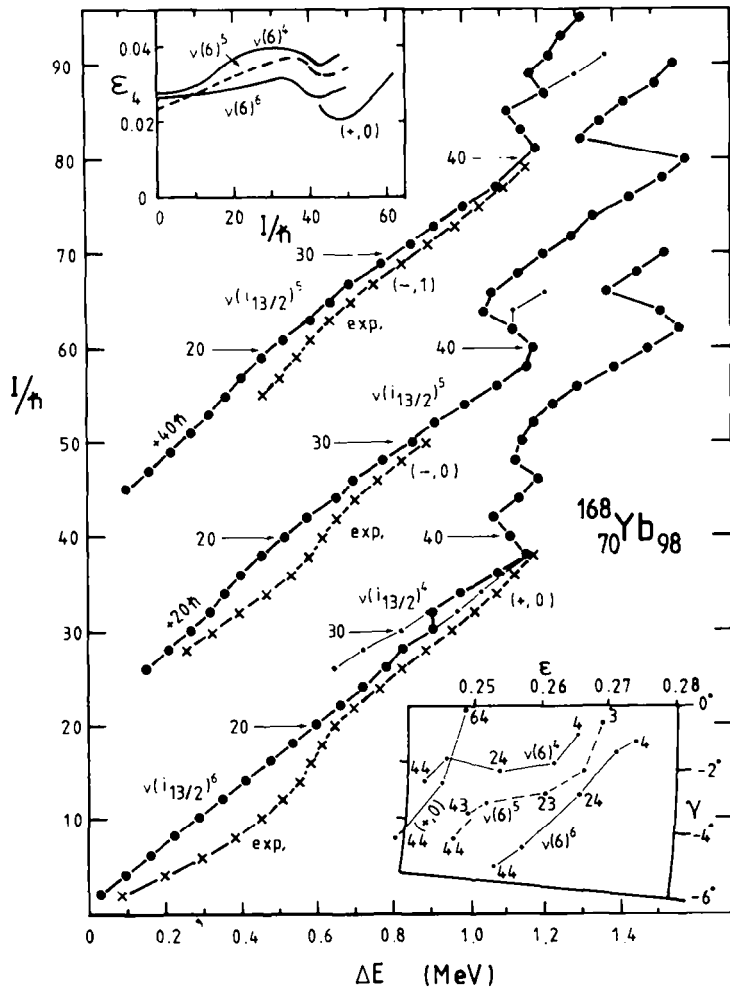


Fig. 23. Experimental⁶⁷⁾ and calculated transition energies for ^{168}Yb . The different (π, α) combinations are displaced vertically as in fig. 8. The observed bands are drawn by crosses and the calculated yrast states by large points and heavy lines. Some calculated bands, labelled by the number of neutrons in $i_{13/2}$, are followed away from yrast by thinner lines. The backbend for transition energies $\Delta E = 1.1\text{--}1.2$ MeV results when the first $h_{9/2}$ and $i_{13/2}$ proton orbitals become occupied while the more distinct backbend at $\Delta E \approx 1.4$ MeV is caused by a transition to larger deformation, $\epsilon \approx 0.40$ and $\gamma = 23^\circ$. Inserted in the upper-left corner the changes of ϵ_4 in the different calculated bands are illustrated. In the lower-left corner, we show the trajectory in (ϵ, γ) plane of these bands.

both in the experimental and theoretical case. For the measured band, one finds $\hbar^2/2J = 0.00805$ MeV and for the calculated one $\hbar^2/2J = 0.0077$ MeV. These parabolas which correspond to $J^{(1)} = 62.5$ and $65 \hbar^2/\text{MeV}$, respectively, have thus been subtracted in fig. 24. The very straight lines which are obtained for both the measured and calculated (+, 0) bands show that in both cases $J_{\text{band}}^{(2)}$ is very close to $J_{\text{band}}^{(1)}$.

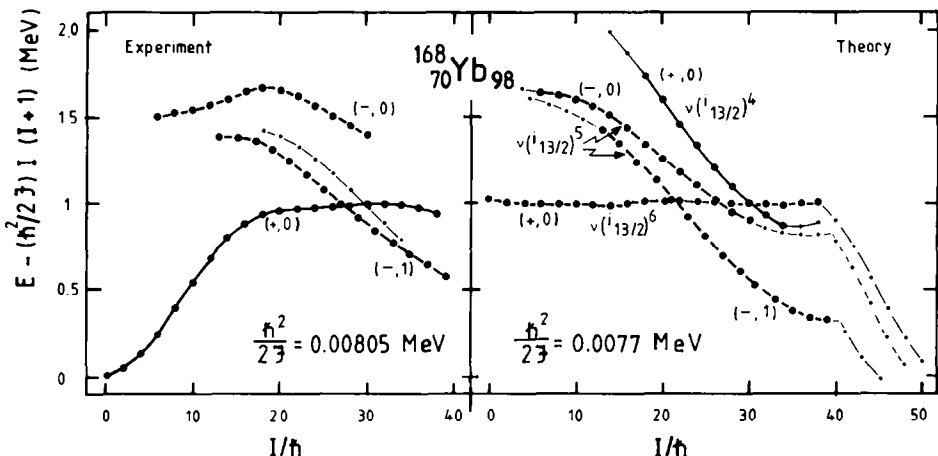


Fig. 24. Comparison between experiment⁶⁷⁾ and theory for the bands which have been observed to high spins in ^{168}Yb . The energies are given relative to a parabola $(\hbar^2/2J)I(I+1)$ with $(\hbar^2/2J)$ equal to 0.00805 and 0.0077 MeV for experimental and calculated bands, respectively. The ordinate corresponds to measured excitation energy and the theoretical energies have been "normalised" to the ground band for $I = 30$. The bands are labelled by parity and signature, (π, α) , and for the calculated bands also by the number of particles in the neutron $i_{13/2}$ shell. One observed band with uncertain spin assignment has been drawn by a thinner line. Thick lines are used for those calculated energies which are assumed to have an experimental correspondence. No pairing correlations are included in the calculations which means that theory and experiment should only be compared for higher spin. The main discrepancy seems to be a small shift between positive- and negative-parity bands, i.e. between $0p0h$ and $1p1h$ bands.

Note especially that the calculated band fits eq. (33) to within ± 20 keV in the whole spin interval $I = 0-38$. In view of the numerical uncertainties, this is certainly somewhat surprising.

The observed moment of inertia for spins $I = 20-38$ in ^{168}Yb ($J \approx 62.5 \hbar^2/\text{MeV}$) amounts to $\sim 80\%$ of the rigid-body value for the calculated deformation, $\varepsilon \approx 0.26$ ($r_0 = 1.2 \text{ fm}$). It is then very interesting to note that the calculations reproduce this value to within 5%. Then the calculated $J^{(1)}$ moment of inertia increases considerably in the backbending region, $I = 40-50$, reaching $\sim 110\%$ of the rigid-body value for $I = 50$. These calculated fluctuations around the rigid-body value, to which the average trends are normalized, are caused by shell effects. Our results thus indicate that neither any proton nor any neutron pairing is needed to account for the moment of inertia observed in ^{168}Yb .

Also the relative energies between the different bands in ^{168}Yb are described in our calculations in a satisfying way. Both theoretically and experimentally, the $\alpha = 1$ negative-parity band becomes yrast at high spins, at $I = 21$ and $I = 27$, respectively. Furthermore, at the higher spin values, the signature splitting between the two odd-parity bands which seems to be built with one neutron in $[521\frac{1}{2}]$ (see fig. 22) is more or less reproduced. In the calculations, the ground band with 6 neutrons in $i_{13/2}$ is crossed by another $(+, 0)$ band at $I = 30$. The crossing band has only four

neutrons in $i_{13/2}$ which means that the $[521\frac{1}{2}]$ orbital is filled with two neutrons. As seen in fig. 23, the ε_4 value is larger for the band with 4 neutrons in $i_{13/2}$, a fact which can be understood if the present fig. 22 is compared with fig. 1 of ref. ¹⁴).

In the measured spectrum ⁶⁷), there is one unidentified sideband which feeds the ground band. If it is assumed that the feeding transitions are stretched E2's, this band has positive parity and signature $\alpha = 0$. Then as seen in fig. 24 it crosses the ground band at $I \approx 30$ in a very similar way to the calculated band with 4 neutrons in $i_{13/2}$. This fact suggests that the sideband can be described as having 4 neutrons in $i_{13/2}$, contrary to the ground band which should have 6 neutrons in $i_{13/2}$. Another plausible assumption about the sideband might be that it should have one proton excited to $h_{9/2}$ (or possibly $i_{13/2}$). However, this should give an alignment of at least 4–5 \hbar which is not the case. Furthermore, such a band should be strongly favoured also at higher spins and therefore, the weak experimental population of the band is inconsistent with an $h_{9/2}$ proton excitation. Also from this point of view, the $\nu(i_{13/2})^4$ band, which seems to become less favoured around $I = 35$ (see fig. 24) seems more probable.

The observed ⁶⁸) high-spin spectrum of the nucleus $^{168}\text{Hf}_{96}$ is rather similar to that of ^{168}Yb . A band of positive parity is seen up to $I = 34$ while negative-parity bands are seen to $I = 33$ and $I = 30$, respectively. As in ^{168}Yb , these bands are for $I \geq 20$ more or less perfectly described by the pure rotor formula, eq. (33), with the moment of inertia approaching the right-body value. In ref. ⁶⁸), such observations were taken as an evidence for neutron-pairing collapse around $I = 20$.

The observed and calculated transition energies of ^{168}Hf are compared in fig. 25. It is evident from fig. 22 that the calculated ground band has 4 neutrons in $i_{13/2}$ and 8 protons in $h_{11/2}$. Negative-parity bands are then formed either from the excitation of one neutron into $i_{13/2}$ or from the excitation of one proton into $h_{11/2}$. In the present calculations, the proton excitation is favoured by up to ~ 400 keV for spin $I \geq 20$ while the experimental systematics ⁶⁸) rather suggest a neutron excitation. Then, as in ^{168}Yb , the negative-parity bands are built with 5 neutrons in $i_{13/2}$. It is therefore natural that the transition energies for these bands are very similar at high spins in the two nuclei. For the negative-parity bands, the agreement between theory and experiment is also about as good in both cases, with the $J^{(2)}$ moment of inertia being more or less reproduced and $J^{(1)}$ slightly off. One furthermore finds a larger signature splitting in ^{168}Yb than in ^{168}Hf , a property which also comes out from the calculation and is caused by the larger splitting in $[521\frac{1}{2}]$ than in $[523\frac{5}{2}]$, see fig. 22.

The positive-parity band of ^{168}Hf is not as well reproduced in the present calculations. The calculated band with four neutrons in $i_{13/2}$ has $J^{(2)}$ considerably smaller than $J^{(1)}$ while these two moments of inertia are very similar in the bands observed experimentally. This leads to a gradually diminishing difference between the calculated and observed transition energies.

In a similar manner to ^{168}Yb , the backbend caused by the filling of the first $h_{9/2}$ proton orbital is predicted to occur in ^{168}Hf around the highest observed spins. Also

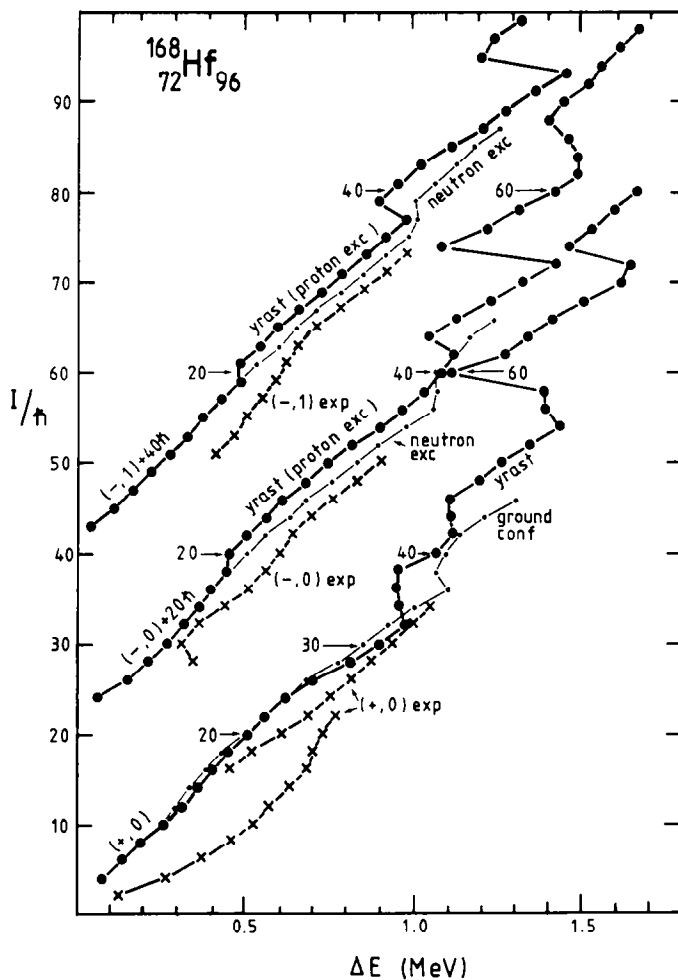


Fig. 25. Calculated and observed 68) transition energies as in figs. 18 and 23, but for ^{168}Hf . For $I \geq 20$ the calculated negative-parity side bands with one proton excited come up to a few hundred keV below those resulting from a neutron excitation.

the still higher spin properties, the crossing of the $i_{13/2}$ proton orbital and the superbackbend should be very similar in the two nuclei.

The high-spin spectrum of ^{165}Yb was observed on an early stage and in connection with the experiment, some conclusions about a considerable pairing decrease were drawn $^{69})$. The transition energies for the three observed bands are compared to experiment in fig. 26. From fig. 22, it is evident that the positive-parity band has 3 neutrons in $i_{13/2}$ and the negative-parity bands has 4 neutrons in $i_{13/2}$. This shows up in the calculated spectrum where the transition energies are higher for positive than for negative parity. In other words, it is energetically more expensive to build high spins for positive parity and this is also the case in the observed spectrum.

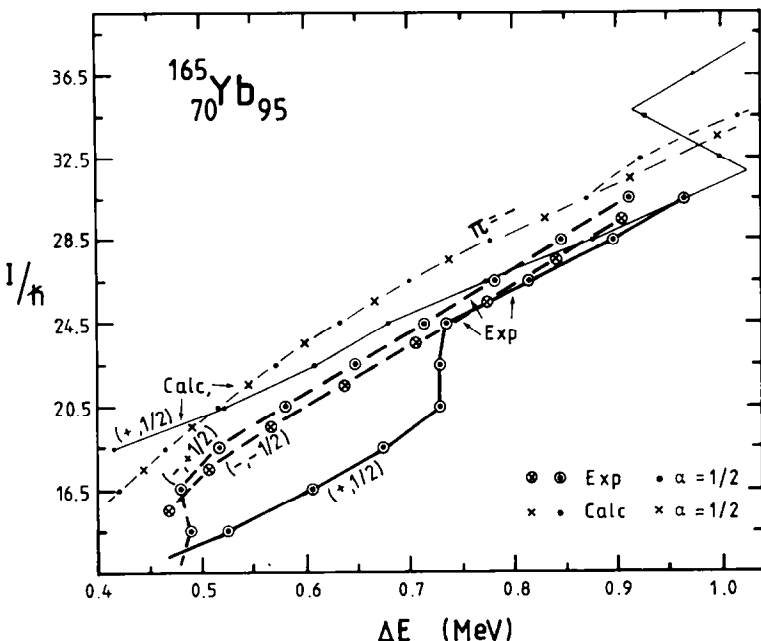


Fig. 26. Same as fig. 23, but for ^{165}Yb with experimental data from ref.⁶⁹). In this figure all bands are plotted without any vertical displacement to facilitate the comparison between different bands.

The difference for positive and negative parity has been described as "different alignments" caused by differences in the pair field⁶⁹). It is then interesting to observe that this feature is described in the present calculations with no pairing difference (because pairing is neglected) between the bands.

The fact that we calculate a more pure band ($J^{(2)} \approx J^{(1)} = \text{const}$) in ^{168}Yb than in ^{168}Hf (or ^{165}Yb) can be understood as being caused by the different neutron configurations [cf. ref.⁷⁰]. To exemplify the alignment process, we plot in fig. 27 the spin contribution as a function of cranking frequency for a few neutron numbers corresponding to 2 ($N = 90$), 3 ($N = 93$), 4 ($N = 96$) and 6 ($N = 98$) neutrons in $i_{13/2}$ orbitals. The deformation parameters are kept fixed at roughly the same values as in fig. 22 (only ϵ_4 is a little smaller). In fig. 27, the slope of the spin contribution determines the value of $J_{\text{band}}^{(2)}$, which is also plotted (broken lines). From the latter curves, we can extract $J_{\text{band}}^{(2)}$ at the frequencies $\hbar\omega = 0.25$ and 0.5 MeV and the corresponding decrease as shown in table 4. It is then evident that four particles in $i_{13/2}$ gives a large decrease in $J_{\text{band}}^{(2)}$ for rotational frequencies $\hbar\omega = 0.25-0.5$ MeV. The small value calculated at $\hbar\omega = 0.5$ MeV is understood from the fact that for this rotational frequency the spin vectors of the four neutrons in $i_{13/2}$ are more or less fully aligned and very little additional spin can be extracted from $i_{13/2}$. Therefore, it becomes comparatively more expensive to build higher-spin states and $J_{\text{band}}^{(2)}$ becomes smaller. This is contrary to ^{168}Yb with 6 neutrons in $i_{13/2}$, where both the

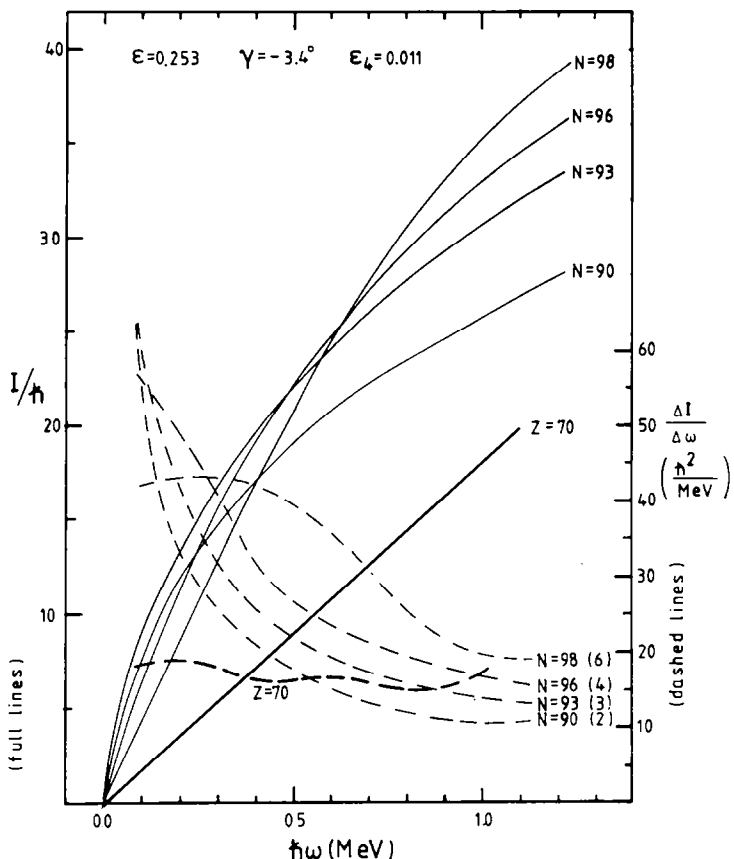


Fig. 27. Spin contribution versus cranking frequency (full lines) for a few neutron numbers, at a fixed deformation. The neutron numbers are such that they correspond to 2 ($N = 90$), 3 ($N = 93$), 4 ($N = 96$) and 6 ($N = 98$) particles in the $i_{13/2}$ subshell, cf. fig. 22. The proton spin contribution for $Z = 70$ is also shown. Broken lines show the slope of the full lines, i.e. the $J_{\text{band}}^{(2)}$ moment of inertia.

TABLE 4
 $J_{\text{band}}^{(2)}$ contributions at $\hbar\omega = 0.25$ and 0.5 MeV for the neutron configurations in fig. 27

Neutrons in $i_{13/2}$	$J_{\text{band}}^{(2)}$		$\Delta J_{\text{band}}^{(2)}$ [\hbar^2/MeV]
	$\hbar\omega = 0.25$ MeV [\hbar^2/MeV]	$\hbar\omega = 0.5$ MeV [\hbar^2/MeV]	
6 ($N = 98$)	43	39	4
4 ($N = 96$)	45	27	18
3 ($N = 93$)	36	22	14
2 ($N = 90$)	29	18	11

fifth and the sixth neutron align at a comparatively high rotational frequency, leading to a larger $J_{\text{band}}^{(2)}$ contribution at $\hbar\omega = 0.5$ MeV. In the negative-parity bands of both ^{168}Yb and ^{168}Hf there are 5 neutrons in $i_{13/2}$ leading to some intermediate value of $J_{\text{band}}^{(2)}$.

The proton spin contribution and corresponding $J_{\text{band}}^{(2)}$ for $Z = 70$ is also plotted in fig. 27. One observes a nice collective behaviour with the $J^{(2)}$ contribution more or less independent of spin. The variation of $J_{\text{band}}^{(2)}$ we calculate in ^{168}Hf is thus solely an effect from the neutrons. One could imagine that our assumption of no pairing correlation is not valid even at the highest spins and that the pairing correlations influences the alignment in $i_{13/2}$. It is, however, difficult to see how this could lead to an increased and constant value of $J_{\text{band}}^{(2)}$. Another possibility is that the alignment process is not correctly described in the Nilsson model, for example due to the presence of the I^2 term.

The present calculations could also give some idea about the position of the proton $i_{13/2}$ and $h_{9/2}$ orbitals. If they were situated at a much lower energy than they are with our set of single-particle parameters, the backbend resulting from their occupation should have been visible in the experimental states. The possibility of a substantial proton pairing would not modify this conclusion in any major way. Especially, one would expect a negative-parity band with one proton in $h_{9/2}$ to be strongly favoured in the spin range where discrete states are observed.

8.2. THE NUCLEUS ^{171}Ta : SOFTNESS IN DEFORMATION

High-spin states up to $^{69}\frac{1}{2}$ have been observed in ^{171}Ta [ref. 71)]. For this nucleus we have great difficulties in reproducing all the observed states, but we still think that a comparison between theory and experiment might help in getting a better understanding of the experimental data. Furthermore, such a comparison might yield some information on the position of the proton $h_{9/2}$ and $i_{13/2}$ orbitals. It was pointed out in ref. 71) that the experimental spectra of ^{171}Ta and ^{177}Re seem to be inconsistent with the modified oscillator position of these subshells if the parameters of ref. 25) are used.

The ground-state band of ^{171}Ta is identified as being built on the $[541\frac{1}{2}]$ orbital 71), which is the lowest orbital in the $h_{9/2}$ subshell. The lowest positive-parity $\alpha = +\frac{1}{2}$ band is built on the $[402\frac{5}{2}]$ orbital but at spin $\frac{33}{2}$; a highly-aligned decay sequence is seen to feed into it. This sequence is thought to originate from the $[660\frac{1}{2}]$ orbital 71).

Calculated and observed transition energies for the two bands which have been observed to the highest spins are compared in fig. 28. It is interesting to note the agreement between the calculated ground band and the observed high-spin positive-parity $\alpha = +\frac{1}{2}$ band. It should, however, be noted that while the calculated band has the odd proton in the $[402\frac{5}{2}]$ orbital, the observed one above the backbend around $I = \frac{33}{2}$ is believed to have one proton in the $[660\frac{1}{2}]$ orbital.

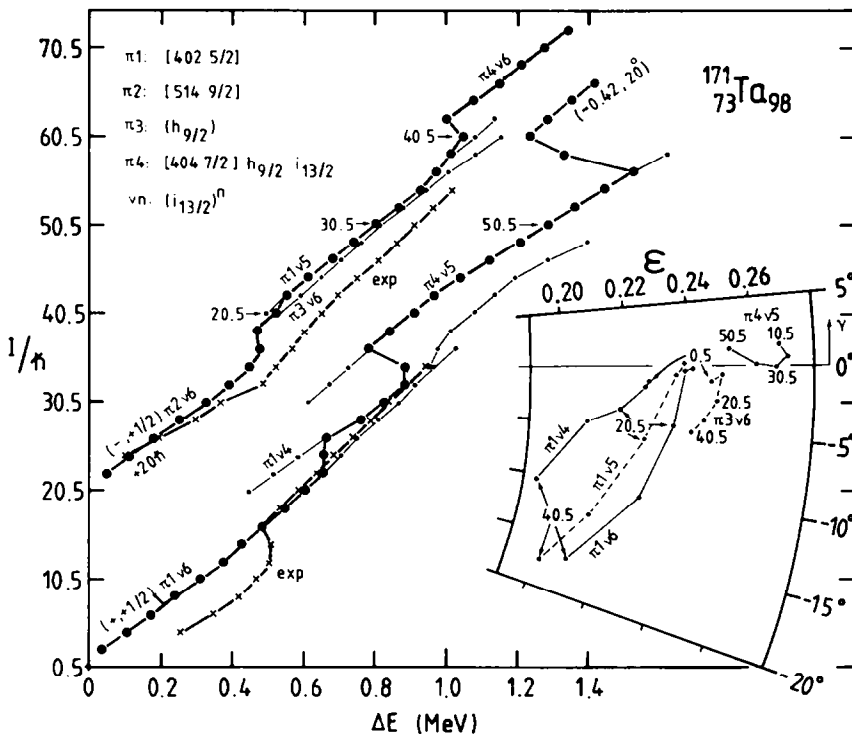


Fig. 28. Spin versus transition energy as in fig. 23 but for ^{171}Ta . The only experimental bands included are those two which have been observed up to very high spin, $I = \frac{69}{2}$ [ref. ⁷¹]. The calculated bands are labelled according to the position of the "unpaired" proton(s) and the number of neutrons in $i_{13/2}$ (cf. fig. 22). The yrast transitions are shown by larger points. For most of the bands, the shape trajectories in the (ϵ, γ) plane are also given in the insert. Configurations with 4, 5 and 6 neutrons in $i_{13/2}$ combined with different proton configurations compete along the yrast line giving rise to many more or less degenerate bands in the yrast region. The large shape changes within these bands and between the bands, i.e. the soft energy surfaces, seem to be an important factor for a more detailed understanding of the observed bands. It is interesting, though probably of no relevance, to observe the agreement over almost 20 units of spin between the observed $(+, +\frac{1}{2})$ band and the calculated $[402\frac{5}{2}]$ band.

Both the observed and the calculated positive-parity band has a $J^{(2)}$ value which is larger than $J^{(1)}$. In the calculated band this depends on rather important shape changes in ^{171}Ta , as also illustrated in fig. 28. Thus, if the shape stayed fixed we would obtain $J^{(1)} = J^{(2)}$, in a similar way to ^{168}Yb which has as many neutrons as ^{171}Ta . The shape changes in ^{171}Ta makes it comparatively "cheaper" to build higher spins, i.e. larger $J^{(2)}$ (cf. fig. 31 below).

The observed negative-parity $\alpha = +\frac{1}{2}$ band seems to have one proton in $\hbar_{9/2}$. In the calculations, this band becomes yrast first for $I = 18$. Similarly to the positive-parity band, the observed band has $J^{(2)}$ larger than $J^{(1)}$ which in this case is not borne out theoretically. It turns out that the proton in $\hbar_{9/2}$ more or less prevents the shape changes towards negative γ -values and the aligned spin then leads to $J^{(2)} < J^{(1)}$ in the calculations.

For positive parity and $\alpha = +\frac{1}{2}$, a band built on the proton [660₂¹] orbital is calculated to become yrast first for spin values greater than 30. Similarly to the h_{9/2} orbital, the shape changes are quite small and $J^{(2)}$ is considerably smaller than $J^{(1)}$.

It thus seems that both the h_{9/2} and i_{13/2} subshells are situated too high in energy with our set of single-particle parameters. One should, however, note that if the shells are lowered substantially, we would get major difficulties with the neighbouring nuclei. Thus, contrary to experimental findings, we would calculate backbends caused by these orbitals in spin regions where discrete bands are observed in ¹⁶⁸Yb and ¹⁶⁸Hf (see subsect. 8.1). Furthermore, the backbends seen as fillings of the valley in, for example, ¹⁶⁶Yb (subsect. 7.3) would come at a lower frequency than $\hbar\omega = 0.6$ MeV. One solution to this problem might be a major shift of the h_{9/2} subshell with particle number as discussed for somewhat heavier systems in refs. ^{72,73}). It seems however that these shifts are largely effects of deformation ^{74,44}). Another possibility would be an important difference in shape between ¹⁶⁸Yb and ¹⁷¹Ta. Such changes in deformation do not result from the present calculations but might be suggested from the softness of the ¹⁷¹Ta energy surfaces.

8.3. THE NUCLEUS ¹⁶⁰Yb: SHAPE CHANGE AND BAND TERMINATION?

Rare-earth nuclei with $N \approx 90$ are much more soft towards γ -deformations than the heavier nuclei discussed above. For spins below 40, they are calculated to be prolate with a deformation $\epsilon = 0.16-0.20$. At higher spins a change from collective rotation to particle-hole excitations, with γ approaching 60°, is expected (cf. sect. 5). Rotational bands in the nucleus ¹⁶⁰Yb have been found up to spin 38 [refs. ^{75,76}]), i.e. just below the region where the shape change might take place. A plot of transition energies versus spin for the (+, 0) states of this nucleus is shown in fig. 29. The calculated ground configuration has 8 protons in the h_{11/2} subshell (i.e. 2 holes in the $Z = 64$ core) and 2 neutrons in i_{13/2}. The nucleus then follows the general trend in this region as discussed in sect. 5 above and in ref. ¹⁵). Thus, the deformation decreases with increasing spin and there is a tendency to close the $Z = 64$ core. Therefore, around $I = 30$ the ground band is crossed by a band with 6 protons in h_{11/2}. The latter band begins to drift strongly out into the γ -plane in the $I = 30-40$ region and terminates on the oblate axis at $I = 48$, the corresponding configuration being $\pi(h_{11/2})^6_{18}\nu[f_{7/2}h_{9/2})^6_{18}(i_{13/2})^2_{12}]_{30}$. As discussed in subsect. 7.1, we calculate an increase of $J_{\text{band}}^{(2)}$ close to the termination.

For $I \geq 30$, the observed yrast transitions of the (+, 0) agree roughly with the calculated ones as seen in fig. 29. This holds true for both calculated bands with 8 and 6 particles in h_{11/2}, respectively. The fact that no decrease of the transition energies are observed at the highest spins might suggest that the experimental band has rather 8 protons in h_{11/2}. However, the irregularities we predict in the band with 6 protons in h_{11/2} are caused by shape changes and are therefore associated with rather large uncertainties.

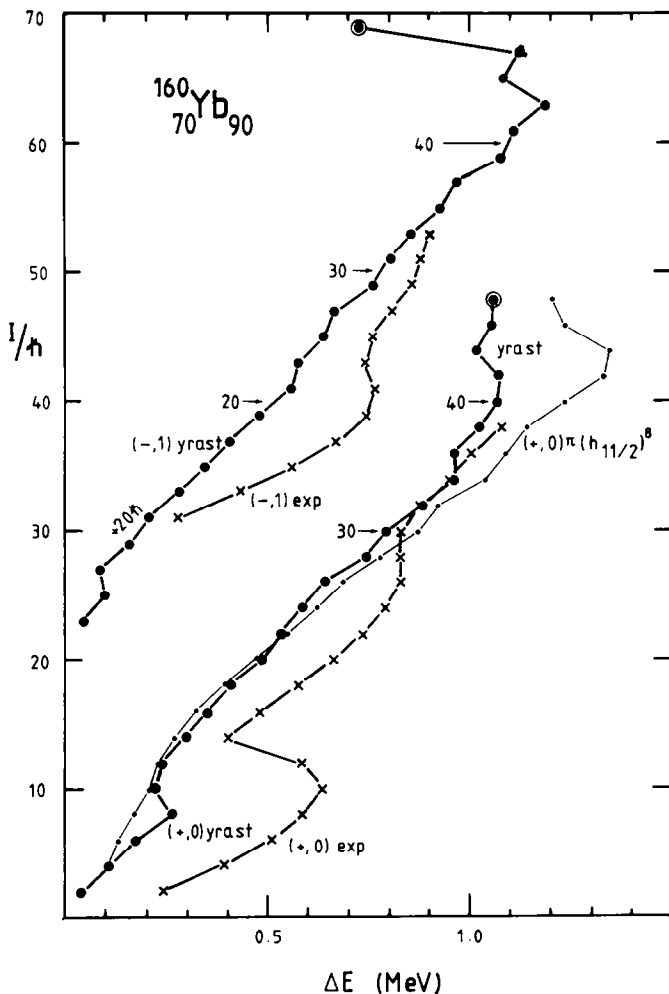


Fig. 29. Calculated and observed^{75,76)} transition energies as in figs. 18 and 23, but for ¹⁶⁰Yb. Band terminations are marked by open circles.

Also for the $(-, 1)$ band the observed and calculated transition energies come close for $I \geq 30$. The calculated band is built from a configuration with 7 particles in $h_{11/2}$; i.e. this subshell is more than half-full, and therefore we see no real termination of this band in agreement with general expectations¹⁵⁾. We predict this band to be yrast up to $I = 45$. At higher spins, the configuration with 5 protons in $h_{11/2}$, which terminates for $I = 49$, becomes somewhat lower in energy.

In summary, to be able to draw any firm conclusions about large shape changes and possible band terminations in ¹⁶⁰Yb, discrete states should be observed up to $I = 45-50$. Similar conclusions can be drawn about the nucleus ¹⁵⁸Er₉₀ which was studied in detail in ref.¹⁵⁾, while for ¹⁵⁸Yb (sect. 5) there is evidence for band termination^{52,53)}.

8.4. THE NUCLEUS ^{130}Ce : COMPETITION BETWEEN DIFFERENT DEFORMATIONS

As an example of high-spin spectra of lighter nuclei we take $^{130}\text{Ce}_{72}$, with high-spin states observed up to spin 32 $^+$ [refs. 63,77)]. The yrast states are calculated to be prolate with $\epsilon \approx 0.25$ between spins 10 and 22. At higher spins bands with a larger deformation, $\epsilon \approx 0.35$, become yrast (cf. subsect. 7.2 above). This nucleus is rather soft towards γ -deformations, like many nuclei in this mass region. Thus, below spin 10,

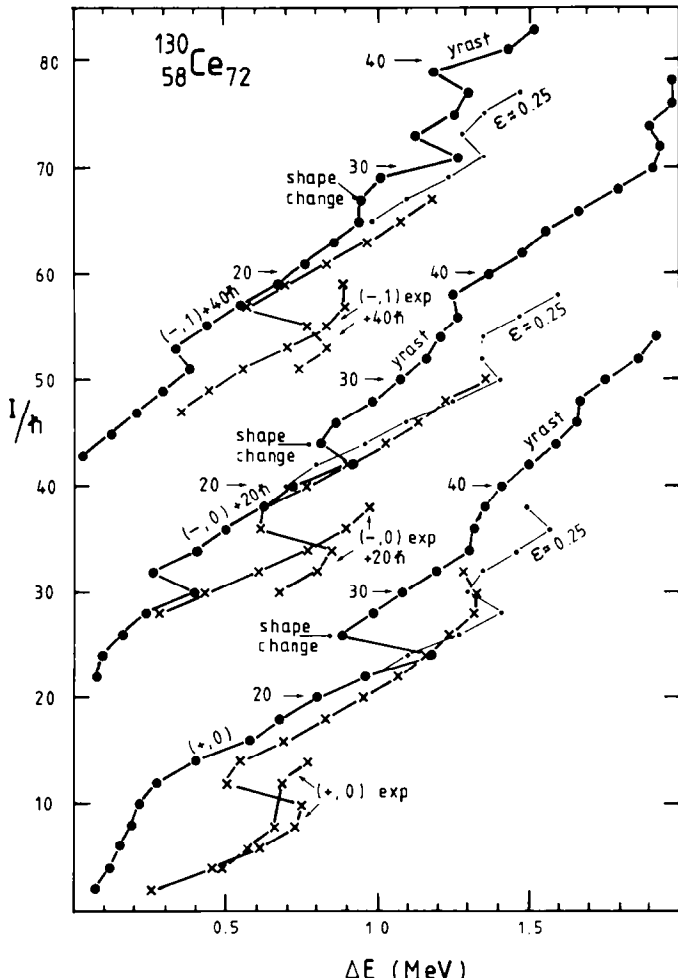


Fig. 30. Same as figs. 18 and 23, but for ^{130}Ce , with experimental data from 63,77). For low spins, we calculate a deformation $\epsilon = 0.25$ which jumps between different γ -values, giving rise to backbends in the negative-parity bands. In a large spin interval $I = 15-40$, there are essentially two coexistent minima, one γ -soft but essentially prolate at $\epsilon = 0.20-0.25$ and another at $\epsilon \approx 0.35$ and $\gamma = 0^\circ$. The latter becomes yrast for $I = 25$. If the configurations at the lower deformation, $\pi(h_{11/2})^{2,3} \nu(h_{11/2})^8$ (cf. fig. 17), are followed to higher spins, the thinner lines result. One could note that at higher spins, also small deformation configurations with 6 or 7 neutron in $h_{11/2}$ become energetically competitive. The backbends just below spin 40 are caused by the filling of the first $N_{\text{rot}} = 6$ neutron orbital, see fig. 21.

most yrast negative-parity states are calculated to have $\gamma = -40^\circ$ or $\gamma \approx +40^\circ$ (the 6^- and 8^- states). For the prolate bands around spin 20, there is a rather good agreement with the observed states above the backbends, as shown in fig. 30. This agreement is continued to the highest observed spin values by keeping the configuration of the prolate bands with $\epsilon = 0.25$, cf. fig. 17. The positive-parity band has two protons in $h_{11/2}$ orbitals while the negative-parity bands are built by promoting one proton in $N_{\text{rot}} = 4$ to the third $h_{11/2}$ orbital [$541\frac{3}{2} \alpha = -\frac{1}{2}$]. It is interesting to note that both the observed and the calculated (+, 0) bands show a backbend at spin $I \approx 28$. The calculated backbend is caused by the occupation of a neutron $h_{9/2} \times f_{7/2}$ orbital ($[541\frac{1}{2}]$). In the (-, 0) band, states are observed up to spin 30^- , while the backbend is calculated to occur at spin 32^- .

The moment of inertia $J_{\text{band}}^{(2)}$ is not so well reproduced especially in the (+, 0) band. This may be due to a different alignment process in the proton $h_{11/2}$ orbitals as compared to calculations (cf. subsect. 8.1). The proton $h_{11/2}$ orbitals are responsible for the observed backbends below spin 20 in a similar way to the neutron $i_{13/2}$ orbitals in the rare-earth nuclei.

It would be very interesting if transitions within the more deformed bands ($\epsilon = 0.35$) were observed. The observed $J_{\text{band}}^{(2)}$ [ref. 63)] in the continuum reaches a high constant value of about $52 \hbar^2/\text{MeV}$ above $\hbar\omega = 0.62 \text{ MeV}$ as compared to about $45 \hbar^2/\text{MeV}$ for the discrete (+, 0) cascade. Thus one would infer that a major part of the deexciting cascade goes through the more deformed bands, even in the region of the observed discrete transitions which extends up to $\hbar\omega = 0.66 \text{ MeV}$. The calculated transition energies within such bands can be found from fig. 30 when the calculated yrast cascade has "backbended" away from the observed transitions.

9. General features of rotation in non-paired systems

From our study of rotational bands in different nuclei, as described in detail in sects. 4–8, some general features can be extracted; we have found the schematic plot of fig. 31 very instructive. There, we try to illustrate a typical collective rotational band, $E = (\hbar^2/2J_0)I(I+1)$, and the corresponding transition energies, $\Delta E(I \rightarrow I-2) = (\hbar^2/2J_0)(4I+2)$. For such a regular band, one finds for the moment of inertia $J^{(1)} = J^{(2)} = J_0$. The band results from orbitals of the type drawn in the insert of fig. 31. The typical feature is that none of the orbitals just below the Fermi surface becomes strongly aligned at very low rotational frequencies. Bands of this type are, for example, the ground band of ^{168}Yb (figs. 23, 24) and the superdeformed band (c4) of ^{187}Au (figs. 6a, 8). We showed in fig. 27 that for typical ground-state deformations, $\epsilon = 0.20\text{--}0.30$, such pure collective bands first result, at least in the calculations, when the $i_{13/2}$ shell is approximately half-filled. On the other hand, for very large deformations away from $\gamma = 60$ or -120° , it seems as though most bands are of this type. Therefore, the number of particles that can be allowed in

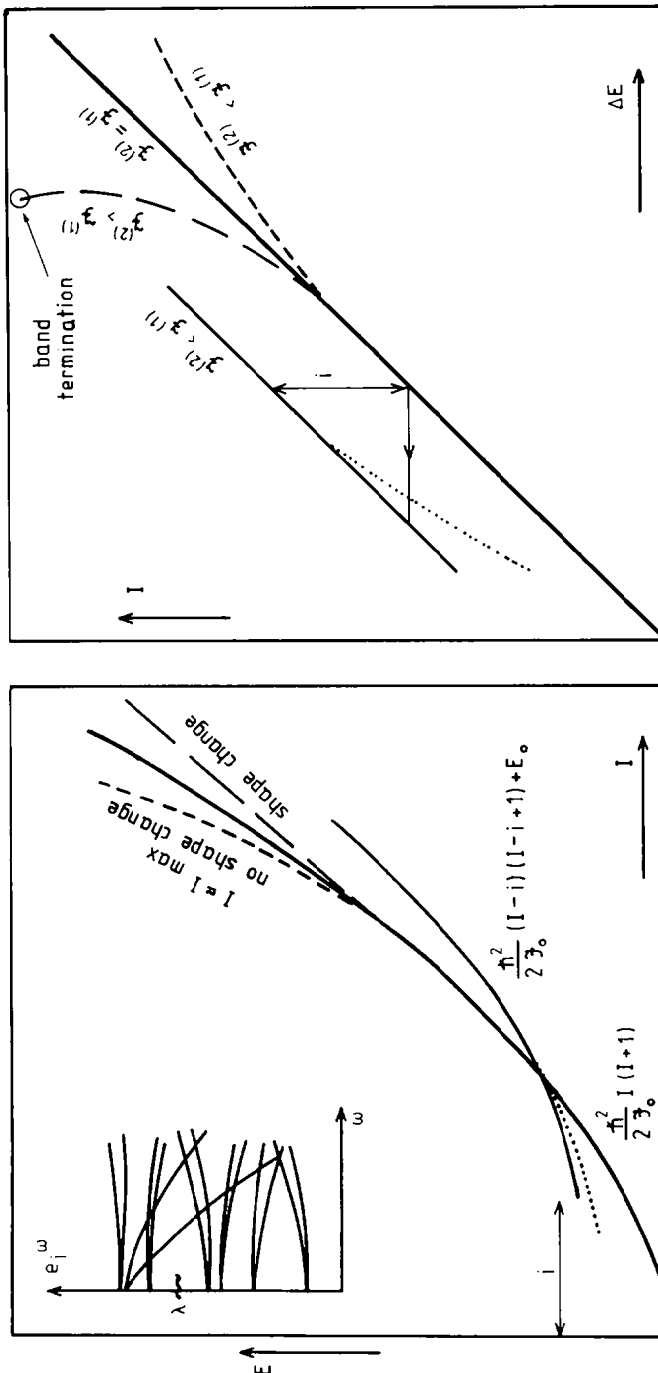


Fig. 31. Schematic illustration of typical unpaired high-spin bands shown as energy E versus spin I to the left and spin I versus transition energy ΔE to the right. The full heavy line shows a pure collective band which results if no orbital just below the Fermi surface λ gets strongly aligned at low frequencies (see insert). Then if one or several strongly aligned orbitals with total alignment i becomes occupied, the E versus I curve is shifted (thinner full line) but still keeping the $J^{(2)}$ moment of inertia as seen from the slope in the I versus ΔE diagram. The dotted line then shows the situation in non-paired calculations if one or several orbitals just below λ aligns quickly at low frequencies (a situation that generally leads to a backbend if pairing is included). At higher spin, energy might be gained from shape changes (long-dashed line) where an especially strong effect might result for a favoured band termination. On the other hand, if a configuration comes close to its maximal spin staying at a more or less constant deformation, the last spin units become energetically expensive (short-dashed line). In this case there is generally some other more favoured band (more alignment and/or different deformation) which becomes yrast.

high- j shells depends on the deformation. This is in some sense equivalent to the well known property that the high- j shells become strongly mixed at large deformations.

At some rotational frequency, a strongly aligned orbital will come down and cross the Fermi surface. With aligned spin i , the energy of the corresponding rotational band depends approximately on spin as $E = E_0 + (\hbar^2/2J_0)(I-i)(I+1-i)$. This gives for the moment of inertia, $J^{(2)} = J_0$ and $J^{(1)} = J_0(I+i/I)$, where $J^{(1)}$ is evaluated at the collective spin I , i.e. the total spin $(I+i)$ [ref. ³⁹]. Thus with an aligned spin of this type we obtain the well-known property that $J^{(2)} < J^{(1)}$. Bands of this type were calculated in ¹⁸⁷Au, specifically c1, c2, c2' and c3 (figs. 6a, 8). In our simplified discussion we have assumed that the deformation stays constant, and that the small shape changes in ¹⁸⁷Au do not affect the general picture. Indeed, such aligned orbitals which become occupied will have a tendency to increase the γ -value. Then, depending on the stiffness of the core, this increase of γ might become more or less important.

The situation where, for example, two high- j orbitals are occupied already in the ground state can also be put into this scheme. Then, in the present calculations, they align gradually but still rather fast, having obtained essentially full alignment for say $I = 20$. Corresponding energies are drawn with dotted lines in fig. 31. For higher spin, there is no difference from the situation where the aligned orbitals cross the Fermi surface and become occupied first at higher spins. It is well known that the alignment process for high- j orbitals is strongly dependent on pairing and is therefore not described in a realistic way by the present calculations. However, this should happen for comparatively low spins (say $I \leq 20$) and is therefore not important at higher spins where such orbitals have achieved more or less full alignment. A typical situation with a few high- j orbitals occupied already at low spins was studied in ¹³⁰Ce with two protons in $h_{11/2}$. Our calculations also gave a somewhat similar result for ¹⁶⁸Hf (fig. 25) while experiments rather suggest that with one-third of the $i_{13/2}$ shell filled a pure collective band should result.

With increasing spin within one fixed configuration, there is the possibility of important shape changes. Of course, such shape changes occur because it is energetically favourable. The energy gain which is illustrated with long-dashed lines in fig. 31 will primarily affect the $J^{(2)}$ moment of inertia, leading to values which are considerably larger than J_0 . One such case was calculated for the ground band [402₂⁵] in ¹⁷¹Ta. A special kind of shape change is the band termination with drastic shape change for spins close to the maximal spin within the configuration. One nucleus where the effect on $J^{(2)}$ seems to be very large is ¹⁵⁸Yb (fig. 14). In this case, also the effects on $J^{(1)}$ are far from negligible. Similar but somewhat weaker effects are predicted in ¹⁶⁰Yb (fig. 29) where the discrete spectroscopy is coming close to the spins for which the effects should be observable. Even weaker but still important effects should be present in ¹⁰⁶Pd (fig. 19). In this case, there is also experimental evidence from $\gamma\gamma$ -correlation experiments on variations in $J^{(2)}$.

A further possibility is that a configuration comes close to its maximal spin but it cannot really find any favoured deformation change (short-dashed lines in fig. 31). Then, the last spin units will become energetically quite expensive, corresponding to a small value of $J^{(2)}$. This is, for example, what happens for the calculated ^{187}Au yrast bands around $I = 40$ (fig. 6a) and for the ^{118}Te yrast bands around $I = 45$ (fig. 16).

Our calculations also give rather clear-cut suggestions about in which nuclear regions one can expect to find the different situations illustrated in fig. 31 and about the value of J_0 . In the middle of a shell, there are no band crossings at low frequencies and the maximal spin in the ground-state configurations is quite high. Thus one should expect to follow the pure collective rotation. Furthermore, as the moment of inertia $J^{(1)}$ should correspond to J_{rig} on the average, one must expect $J_0 \approx J_{\text{rig}}$ ($= J^{(1)} = J^{(2)}$). The typical example studied here (and experimentally) is $^{168}\text{Yb}_{98}$, where both the proton $h_{11/2}$ and neutron $i_{13/2}$ shell are half-filled and where furthermore the number of protons and neutrons is more or less in the middle between closed shells. A similar situation was found in ^{171}Ta , where, however, rather important shape changes seem to give $J^{(2)} > J^{(1)}$ over a large spin region.

Coming closer to the end of a shell, orbitals from the shell above will give band crossings at low rotational frequencies. Thus, the total spin is largely built from single-particle alignment which must mean that the collective J_0 , as defined in fig. 31, is much smaller than J_{rig} . The prolate or near-prolate bands in ^{187}Au are typical examples while the bands at $\gamma \approx -100^\circ$ seem to be some kind of extreme of this situation.

If the valence protons as well as the valence neutrons occupy orbitals in the beginning of a shell, one expects strong tendencies towards alignment connected with band terminations. Close to the band termination, we then calculate quite large values of $J^{(2)}$ as discussed above. This is contrary to the case when the alignment tendencies are weaker (for example, because only one kind of particles are in the beginning of a shell), which leads to a shape that stays more or less constant with spin, possibly with some increase towards positive γ . One then obtains a standard band with some alignment i (see fig. 31) and $J^{(2)} < J^{(1)}$.

Cases where band terminations have been observed experimentally are ^{20}Ne [ref. ⁷⁸] and possibly ^{22}Ne [ref. ⁷⁹] which nuclei were studied within the cranking formalism in ref. ¹²). In fig. 32, the spins are plotted versus the corresponding energy differences $\Delta E(I \rightarrow I-2)$. In both cases, one observes a decrease of ΔE for the terminating state, $I = 8$ and $I = 10$, respectively. In the language used for heavier nuclei, this would correspond to an increasing (infinite) $J^{(2)}$ at the band termination. In the very light nucleus ^8Be , on the other hand, the calculated shape ¹³) is more or less unchanged also at the highest spin in the ground band, $I = 4$. In agreement with the discussions above, this leads to a comparatively high energy for the 4^+ state (fig. 32). These observations in very light nuclei give some support for the predicted but still largely unobserved features of fig. 31.

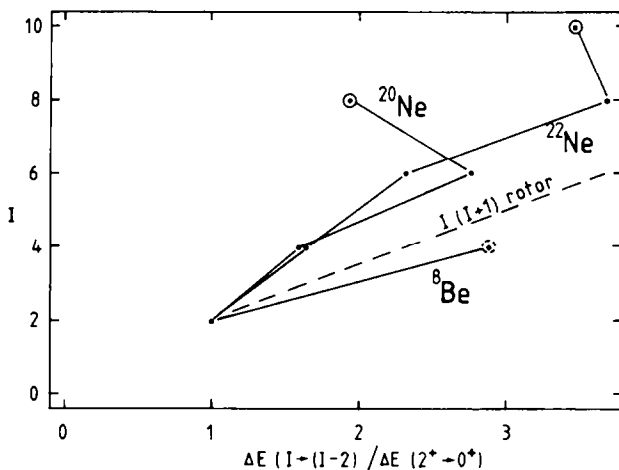


Fig. 32. Experimentally observed transition energies up to the maximal spin for the ground bands in $^{20,22}\text{Ne}$ and ^8Be compared to an ideal $I(I+1)$ rotor. The energies are normalised to the $2^+ \rightarrow 0^+$ transition. Note the very low energy of the 8^+ state in ^{20}Ne and the 10^+ state in ^{22}Ne while the 4^+ state in ^8Be is relatively high in energy. In calculations, the bands in the two heavier nuclei terminate for oblate shape (ph excitations), while in ^8Be the deformation is more or less unchanged "throughout the band".

10. Summary and conclusions

We have presented a formalism where, for different rotational bands in the yrast region, the energy is minimised with respect to deformation, ϵ , γ and ϵ_4 . The formalism relies on the cranking model but with the non-standard feature that crossings or virtual crossings between single-particle orbitals are given special attention. Apart from standard parameters determining the liquid-drop energy and the single-particle spectra, there are no free parameters in the calculations. The single-particle cranking hamiltonian is diagonalised in a rotating harmonic-oscillator basis. Then there are only small admixtures between different oscillator shells so the total number of quanta can be treated as a preserved quantum number. This means that we can put labels on a large number of configurations and construct a variety of rotational bands in the yrast and near-yrast region. Pairing is neglected in our calculations which means that it is not reasonable to make any quantitative comparison to experiment for low spin. However, for more qualitative considerations about yrast shapes and yrast configurations, it is our experience that the calculations are quite useful also for the very lowest spins.

We have applied the formalism to a number of nuclei in the $A = 100-200$ region. Such nuclei where extensive experimental studies of the very high-spin properties are available were primarily chosen. The most important results which emerge are the following:

- (a) In the nucleus ^{168}Yb where very pure rotational bands are observed, a good agreement between theory and experiment is obtained. One especially notes that

the observed moment of inertia of the ground band, being $\sim 80\%$ of the rigid-body value, is reproduced to within 5%. The properties of this nucleus and the neighbouring ones, ^{168}Hf and ^{165}Yb , were discussed in terms of the number of neutrons in the $i_{13/2}$ subshell (subsect. 8.1).

(b) In ^{118}Te , we predict a transition from ph excitations to collective rotation around $I = 30$ in agreement with continuum-type experiments. These collective bands show a rather weak collectivity with $J_{\text{band}}^{(2)} \approx \frac{1}{2}J^{(1)}$ (subsect. 6.1). In this context, it is interesting to note the small $J_{\text{band}}^{(2)}$ which is observed for nuclei centred around ^{122}Xe (subsect. 7.2).

(c) The potential energy surfaces of ^{187}Au show two distinct minima for $I \leq 50$. For one of the minima ($\gamma = 0-30^\circ$) bands which are clearly collective should result while for the other minimum ($\gamma = -60- -120^\circ$) we predict high spin states of more or less pure ph character. These results are partly supported by experiment (sect. 4).

(d) For the nuclei with some 10-12 particles outside the ^{146}Gd core, further studies on terminating bands were carried out. It was found that the terminating bands in ^{158}Yb are very strongly favoured energetically. This is in nice agreement with some recent evidence that such a band has been observed in this nucleus (sect. 5). In ^{160}Yb where the calculated terminations are less pronounced, the observed states up to $I = 38$ show no hint of this effect (subsect. 8.3).

(e) For ^{106}Pd , we suggested that the calculated band terminations just above $I = 30$ are responsible for observed variations in $J_{\text{band}}^{(2)}$ (subsect. 7.1).

(f) For the neutron-deficient Xe/Ba/Ce nuclei, the potential energy surfaces are very soft towards γ -deformation. Furthermore, for both ^{128}Ba and ^{130}Ce one secondary minimum at $\varepsilon \approx 0.35$ becomes energetically competitive for $I = 20-30$. In ^{130}Ce , we obtained a good agreement between measured discrete states ($I \leq 30$) and calculated $\varepsilon \approx 0.25$ bands (subsects. 7.2 and 8.4).

(g) The position of especially the $h_{9/2}$ but also the $i_{13/2}$ proton subshell is enlightened in several respects by the present calculations. With the present parameters (fig. 2 and table 1), strong backbends are predicted in, for example, ^{166}Yb at $\hbar\omega = 0.6$ MeV when the lowest orbitals of these subshells become occupied. These backbends seem to explain observed irregularities in continuum-type experiments (subsect. 7.3). On the other hand, in the $Z = 73$ nucleus ^{171}Ta , we calculate bands with one proton in $h_{9/2}$ or $i_{13/2}$ to become yrast first for $I = 15$ and $I \geq 30$, respectively, in disagreement with experiment. We also pointed out the large deformation changes which seem to result in unusually large values of $J_{\text{band}}^{(2)}$ in this nucleus (subsect. 8.2).

(h) Calculated and observed effective moments of inertia in $A \sim 160$ nuclei are in reasonable agreement and suggest that the superbackbends occur roughly at spins suggested by the potential energy surfaces (subsect. 6.2).

The important question about the disappearance of pairing is not directly studied here. However, the agreement we find between calculations and experiment in the $I \geq 30$ region seems to show that, at least for the transition energies in this spin

region, pairing can only play a minor role. Also for the highest spins the measured moments of inertia are generally somewhat smaller than the calculated ones. However, the discrepancies do not exceed 10% which means that only very little room is left for corrections to the total energy due to pairing. Therefore, for $I \geq 30$, the competition between different configurations in the yrast region could be influenced by pairing only in a minor way and other uncertainties (e.g. single-particle spectra) should be more important.

We are grateful to Dr. W. Nazarewicz who read the entire manuscript and made many helpful comments and suggestions. We also want to thank the experimental groups which have supplied us with as yet unpublished experimental data. This project is supported by the Swedish Natural Science Research Council.

References

- 1) S. Cohen, F. Plasil and W.J. Swiatecki, Ann. of Phys. **82** (1974) 557
- 2) A. Bohr and B.R. Mottelson, Proc. Nobel Symp. 27 on superheavy elements - Theoretical predictions and experimental generation, Ronneby 1974, Phys. Scripta **10A** (1974) 13
- 3) R. Bengtsson, S.E. Larsson, G. Leander, P. Möller, S.G. Nilsson, S. Åberg and Z. Szymanski, Phys. Lett. **57B** (1975) 301
- 4) K. Neergård and V.V. Pashkevich, Phys. Lett. **59B** (1975) 218
- 5) G. Andersson, S.E. Larsson, G. Leander, P. Möller, S.G. Nilsson, I. Ragnarsson, S. Åberg, R. Bengtsson, J. Dudek, B. Nerlo-Pomorska, K. Pomorski and Z. Szymanski, Nucl. Phys. **A268** (1976) 205
- 6) K. Neergård, V.V. Pashkevich and S. Frauendorf, Nucl. Phys. **A262** (1976) 61
- 7) K. Neergård, H. Toki, M. Ploszajczak and A. Faessler, Nucl. Phys. **A287** (1977) 48
- 8) C.G. Anderson, G. Hellström, G. Leander, I. Ragnarsson, S. Åberg, J. Krumlinde, S.G. Nilsson and Z. Szymanski, Nucl. Phys. **A309** (1978) 141
- 9) S. Åberg, Phys. Scripta **25** (1982) 23
- 10) M. Cerkaski, J. Dudek, Z. Szymanski, C.G. Andersson, G. Leander, S. Åberg, S.G. Nilsson and I. Ragnarsson, Phys. Lett. **70B** (1977) 9
- 11) T. Dössing, K. Neergård, K. Matsuyanagi and Hsi-Chen Chang, Phys. Rev. Lett. **39** (1977) 1395
- 12) I. Ragnarsson, S. Åberg and R.K. Sheline, Phys. Scripta **24** (1981) 215
- 13) I. Ragnarsson, S. Åberg, H.-B. Häkansson and R.K. Sheline, Nucl. Phys. **A361** (1981) 1
- 14) T. Bengtsson and I. Ragnarsson, Phys. Lett. **115B** (1982) 431
- 15) T. Bengtsson and I. Ragnarsson, Phys. Scripta **T5** (1983) 165
- 16) T. Bengtsson, Phys. Lett. **126B** (1983) 411
- 17) T. Bengtsson, Progress in particle and nuclear physics, vol. 9, ed. D. Wilkinson (Pergamon, 1983) p. 523
- 18) M. Brack, J. Damgaard, A.S. Jensen, H.C. Pauli, W.M. Strutinsky and C.Y. Wong, Rev. Mod. Phys. **44** (1972) 320
- 19) R.A. Sorensen, Rev. Mod. Phys. **45** (1973) 353
- 20) S.E. Larsson, Phys. Scripta **8** (1973) 17
- 21) S.G. Nilsson, Mat. Fys. Medd. Dan. Vid. Selsk. **29**, No. 16 (1955).
- 22) S.G. Rohozinski, Report of the Institute for Nuclear Research, Warsaw, INR 1520/VII/PH/B; S.G. Rohozinski and A. Sobczewski, Acta. Phys. Pol. **B12** (1981) 1001
- 23) W. Nazarewicz and P. Rozmiej, Nucl. Phys. **A369** (1981) 396
- 24) S.E. Larsson, G. Leander, I. Ragnarsson and N.G. Alenius, Nucl. Phys. **A261** (1976) 77

- 25) S.G. Nilsson, C.F. Tsang, A. Sobczewski, Z. Szymanski, S. Wycech, C. Gustafsson, I.-L. Lamm, P. Möller and B. Nilsson, Nucl. Phys. **A131** (1969) 1
- 26) I. Ragnarsson and R.K. Sheline, Phys. Scripta, **29** (1984) 385
- 27) A. Bohr and B.R. Mottelson, Proc. Int. Conf. on nuclear structure, Tokyo 1977, ed. T. Marumori (J. Phys. Soc. Japan **44** suppl.) p. 157
- 28) V.G. Zelevinskii, Sov. J. Nucl. Phys. **22** (1975) 565
- 29) D. Glas, U. Mosel and P.G. Zint, Z. Phys. **A285** (1978) 83
- 30) R. Bengtsson and S. Frauendorf, Nucl. Phys. **A314** (1979) 27
- 31) I. Hamamoto, Nucl. Phys. **A271** (1976) 15
- 32) W. Nazarewicz, J. Dudek, R. Bengtsson, T. Bengtsson and I. Ragnarsson, Nucl. Phys. **A435** (1985) 397
- 33) A. Bohr and B.R. Mottelson, Nuclear structure, vol. 2 (Benjamin, New York, 1975)
- 34) V.M. Strutinsky, Nucl. Phys. **A95** (1967) 420
- 35) W.D. Myers and W.J. Swiatecki, Ark. Phys. **36** (1967) 343
- 36) V.M. Strutinsky, Nucl. Phys. **A122** (1968) 1
- 37) P. Möller, Nucl. Phys. **A142** (1970) 1
- 38) R.M. Diamond and F.S. Stephens, Ann. Rev. Nucl. Part. Sci. **30** (1980) 85
- 39) A. Bohr and B.R. Mottelson, Phys. Scripta **24** (1981) 71
- 40) M.A. Deleplanque, H.J. Körner, H. Kluge, A.O. Macchiavelli, N. Bendjaballah, R.M. Diamond and F.S. Stephens, Phys. Rev. Lett. **50** (1983) 409
- 41) O. Andersen, J.D. Garrett, G.B. Hagemann, B. Herskind, D.L. Hillis and L.L. Riedinger, Phys. Rev. Lett. **43** (1979) 687
- 42) M.A. Deleplanque, F.S. Stephens, O. Andersen, J.D. Garrett, B. Herskind, R.M. Diamond, C. Ellegaard, D.B. Fossan, D.L. Hillis, H. Kluge, M. Neiman, C.P. Roulet, S. Shih and R.S. Simon, Phys. Rev. Lett. **45** (1980) 172
- 43) C. Bourgeois, P. Kilcher, J. Lettessier, V. Berg and M.G. Desthuilliers, Nucl. Phys. **A295** (1978) 424
- 44) C. Ekström, L. Robertsson, S. Ingelman, G. Wannberg and I. Ragnarsson, Nucl. Phys. **A348** (1980) 25
- 45) C. Gerschel, N. Perrin, B. Ader, H. Tricoire, J.P. Thibaud, Orsay preprint (1982)
- 46) S. Frauendorf and F.R. May, Phys. Lett. **125B** (1983) 245
- 47) I. Hamamoto and B. Mottelson, Phys. Lett. **127B** (1983) 281
- 48) C.G. Andersson and J. Krumlinde, Nucl. Phys. **A291** (1977) 21
- 49) I. Ragnarsson, Phys. Lett. **80B** (1978) 4
- 50) I. Ragnarsson, S.G. Nilsson and R.K. Sheline, Phys. Reports **45** (1978) 1
- 51) R.V.F. Janssens, P. Chowdhury, H. Emling, D. Frekers, T.L. Khoo, W. Kühn, Y.H. Chung, P.J. Daly, Z.W. Grabowski, M. Kortelahti, S. Frauendorf and J.Y. Zhang, Phys. Lett. **131B** (1983) 35
- 52) C. Baktash, Y. Schutz, I.Y. Lee, F.K. McGowan, N.R. Johnson, M.L. Halbert, D.C. Hensley, M.P. Fewell, L. Courtney, A.J. Larabee, L.L. Riedinger, A.W. Sunyar, E. der Mateosian, O.C. Kistner and D.G. Sarantites, Phys. Rev. Lett., submitted
- 53) I. Ragnarsson, T. Bengtsson, W. Nazarewicz, J. Dudek and G.A. Leander, in preparation
- 54) M. Jääskeläinen, D.G. Sarantites, F.A. Dilmanian, R. Woodward, H. Puchta, J.R. Beene, J. Hattula, M.L. Halbert and D.C. Hensley, Phys. Scripta **T5** (1983) 175, and references therein
- 55) R.S. Simon, R.M. Diamond, Y. El Masri, J.O. Newton, P. Sawa and F.S. Stephens, Nucl. Phys. **A313** (1979) 209
- 56) I. Ragnarsson, D.P. Soroka and F.S. Stephens, LBL Nuclear Science annual report, 1975, LBL-5075 p. 286
- 57) I. Ragnarsson, T. Bengtsson, G. Leander and S. Åberg, Nucl. Phys. **A347** (1980) 287
- 58) W. Klamra, J. Bialkowski, L. Hildingsson, D. Jerrestam, A. Johnson, J. Kownacki, Th. Lindblad, J. Nyberg, T. Vertse and T. Bengtsson, Nucl. Phys. **A431** (1984) 367
- 59) Th. Lindblad, L. Hildingsson, D. Jerrestam, A. Källberg, A. Johnson, C.J. Herrlander, W. Klamra, A. Kerek, C.G. Linden, J. Kownacki, J. Bialkowski and T. Vertse, Nucl. Phys. **A378** (1982) 364
- 60) H. El-Samman, V. Barci, A. Gizon, J. Gizon, L. Hildingsson, D. Jerrestam, W. Klamra, R. Kossakowski, Th. Lindblad, T. Bengtsson, G. Leander, Nucl. Phys. **A427** (1984) 397

- 61) I. Ragnarsson, A. Sobczewski, R.K. Sheline, S.E. Larsson and B. Nerlo-Pomorska, Nucl. Phys. **A233** (1974) 329
- 62) J. Meyer-ter-Vehn, Nucl. Phys. **A249** (1975) 141
- 63) P.J. Nolan, R. Aryaeinejad, A.H. Nelson, D.J.G. Love, D.M. Todd and P.J. Twin, Phys. Lett. **128B** (1983) 285
- 64) O. Andersen and B. Herskind, private communication
- 65) B. Herskind, Proc. of Int. Conf. on nuclear physics, Florence, 1983, to appear
- 66) A. Pakkanen, Y.H. Chung, P.J. Daly, S.R. Faber, H. Helppi, J. Wilson, P. Chowdhury, T.L. Khoo, I. Ahmad, J. Borggreen, Z.W. Grabowski and D.C. Radford, Phys. Rev. Lett. **48** (1982) 1530
- 67) J.C. Bacelar, C. Ellegard, J.D. Garrett, G.B. Hagemann, B. Herskind, A. Holm, C.-X. Yang, P.O. Tjøm and J.C. Lisle, Contribution to the 5th Nordic Conf. on nuclear physics in Jyväskylä, Finland, March 1984; and to be published
- 68) R. Chapman, J.C. Lisle, J.N. Mo, E. Paul, A. Simcock, J.C. Wilmott, J.R. Leslie, H.G. Prince, P.M. Walker, J.C. Bacelar, J.D. Garrett, G.B. Hagemann, B. Herskind, A. Holm and P.J. Nolan, Phys. Rev. Lett. **51** (1983) 2265
- 69) C. Schück, N. Bendjaballah, R.M. Diamond, Y. Ellis-Akovali, H. Lindenberger, J.O. Newton, S. Shih, F.S. Stephens, J.D. Garrett and B. Herskind, Proc. INS Int. Symp. on dynamics of nuclear collective motion, Mt. Fuji, Japan (Bando, 1982, Osaka) p. 474;
C. Schück, N. Bendjaballah, R.M. Diamond, Y. Ellis-Akovali, K.H. Lindenberger, J.O. Newton, F.S. Stephens, J.D. Garrett and B. Herskind, Phys. Lett. **142B** (1984) 253
- 70) J.-Y. Zhang and S. Åberg, Nucl. Phys. **A390** (1982) 314
- 71) C.X. Yang, J. Kownacki, J.D. Garrett, G.B. Hagemann, B. Herskind, J.C. Bacelar, J.R. Leslie, R. Chapman, J.C. Lisle, J.N. Mo, A. Simcock, J.C. Wilmott, W. Walus, L. Carlen, S. Jönsson, J. Lyttkens, H. Ryde, P.O. Tjøm and P.M. Walker, Phys. Lett. **133B** (1983) 39;
J.C. Bacelar, J.D. Garrett, G.B. Hagemann, B. Herskind, A. Holm, R. Chapman, J.C. Lisle, J.N. Mo, E. Paul, J.C. Wilmott and P.M. Walker, Contribution to the 5th Nordic Conf. on nuclear physics in Jyväskylä, Finland, March 1984; and to be published
- 72) A.L. Goodman, Nucl. Phys. **A287** (1977) 1
- 73) R.A. Sorensen, Proc. 4th Int. Conf. on nuclei far from stability, Helsingør, 1981 (CERN 81-09) p. 498
- 74) J.S. Dionisio, C. Vieu, W. De Wieclawik, R. Foucher, M. Beiner, S.E. Larsson, G. Leander and I. Ragnarsson, J. of Phys. **G2** (1976) L183
- 75) L.L. Riedinger, Phys. Scripta **T5** (1983) 36
- 76) A. Larabee and L.L. Riedinger, private communication (1983)
- 77) P.J. Nolan, R. Aryaeinejad, D.J.G. Love, A.H. Nelson, P.J. Smith, D.M. Todd, P.J. Twin, J.D. Garrett, G.B. Hagemann and B. Herskind, Phys. Scripta **T5** (1983) 153
- 78) Table of isotopes, 7th ed., ed. C.M. Lederer and V.S. Shirley (Wiley, New York, 1978)
- 79) E.M. Szanto, A. Szanto de Toledo, H.V. Klapdor, M. Diebel, J. Fleckner and U. Mosel, Phys. Rev. Lett. **42** (1980) 622